NUMERICAL INVESTIGATION ON LOW DIMENSIONAL MATERIALS FOR GAS ADSORPTION AND SEPARATION

Suchitra Waruni de Silva

Bachelor of Engineering

Submitted in fulfilment of the requirements for the degree of

Doctor of Philosophy

School of Chemistry, Physics and Mechanical Engineering

Science and Engineering Faculty

Queensland University of Technology

2017

STATEMENT OF ORIGINAL AUTHORSHIP

The work contained in this thesis has not been previously submitted to meet requirements for an award at this or any other higher education institution. To the best of my knowledge and belief, the thesis contains no material previously published or written by another person except where due reference is made.

QUT Verified Signature

Signature:

Date: 05-05-2017

Dedicated to Ammi, Chaththi and Danusha

KEYWORDS

Nano adsorbents

Nano membranes

Carbon capture

Hydrogen purification

Gas separation

Heterofullerene

Chemisorption

Selectivity

Permeability

Graphitic carbon nitride

Hexagonal boron nitride

Strain tuning

Charge controlled adsorption

Size sieving

Chemical affinity sieving

ABSTRACT

Gas separation is a key process in many industrial and scientific applications. Energy and environmental related applications such as CO_2 separation from N_2 in post-combustion carbon dioxide capture or H_2 in pre-combustion carbon capture; hydrogen production from syngas and natural gas processing, are examples of industrial applications. The separation efficiency is vital to justify the economic and environmental costs of alternative approaches. However, the overall efficacy of such solutions lies in the availability of materials with superior gas separation performance. Solid adsorbents and membrane separation are two methods that have witnessed an exponential development due to the advancement of nanotechnology. Nanotechnology makes it possible to tailor the structures of materials at the nano-scale to improve adsorption capacity, membrane selectivity and permeability. Graphene and other carbon-based materials are the most commonly studied nanomaterials for such applications. However, other graphene-like, atomically thin, layered materials and other carbon-based low dimensional materials can be suitable candidates as nano-adsorbents or membranes due to their inherent structural similarities to graphene, thus potentially sharing similar integral advantages.

The main aim of this thesis is to study the effectiveness of selective adsorption, membrane separation and adsorptive membrane separation by low dimensional nanomaterials, specifically focusing on hydrogen purification and carbon dioxide capture, which are the pre-dominant gas separation applications related to energy production. We use first-principles quantum mechanical simulations and classical molecular dynamics simulations, or a combination of both, to study the gas separation behaviour of these materials. This thesis especially focuses on the low dimensional nanomaterials: boron doped fullerenes as a carbon dioxide adsorbent, and porous hexagonal boron nitride membranes and graphitic carbon nitrides (C_3N_4 and C_2N), as H_2 purification membranes from CO_2 and CH_4 and, CO_2 separation membranes from N_2 and CH_4. Furthermore, the applicability of nanomaterials tuning techniques: structural tuning, charge

tuning and mechanical tuning for increasing the separation performance or altering the selectivity in the application is evaluated.

The first principles DFT simulations on adsorption capacity have shown that boron doping on pristine C_{60} fullerene, coupled with charge tuning, increases its CO_2 adsorption ability. The study reveals that the BC_{59} fullerene structure with an introduced electron has superior binding energy with CO_2. Most importantly, the study shows that the introduction of a charge field has negligible effects on the N_2 and CH_4 binding characteristics, indicating the applicability in carbon dioxide capture.

The membrane separation studies of porous h-BN with various pore structures show that certain pore openings are capable of purifying H_2 from gas mixtures containing CO_2, N_2 and CH_4. The membrane was subjected to external biaxial strain values of 2.5 and 5% and the gas permeation behaviour was evaluated. This study reveals that not only altering the structural characteristics of the pore opening, but also strain tuning can be used to alter or improve the separation behaviour of the membranes. Overall, this study, which evaluates both pure gas systems and binary gas mixtures, reveals that the gas selectivity and permeability characteristics are influenced by a combination of the size exclusion properties of the pore opening and the chemical affinity due to selective adsorption of certain gas molecules.

Studies of gas permeability of graphitic carbon nitride materials reveal, strained g-C_3N_4 monolayers can be effectively used in H_2 purification from CO_2 and CH_4. A combination of MD and DFT studies shows that the low H_2 permeability across a g-C_3N_4 monolayer membrane under neutral conditions can be drastically improved by subjecting the monolayer to minor biaxial strains as low as 2.5 and 5%, which is much superior to improvements that can be obtained from the conventional method of increasing feed side pressure. Most importantly, the induced strain does not compromise the CO_2 and CH_4 impermeability. A study of 2-D C_2N shows that the structure under neutral conditions is impermeable to all the gas molecules studied. However, under 5% strain this membrane can selectively separate H_2 and CO_2 from N_2 and CH_4.

Interestingly, while size exclusion properties of the membrane make it impermeable to N_2 and CH_4 with larger kinetic diameters, the CO_2 gas that is larger than H_2 has a higher permeability due to the selective adsorption of the CO_2 molecule at the pore. These observations of MD simulations are further confirmed by the DFT simulations.

Overall, this work shows that the studied low dimensional carbon based and carbon like nanomaterials can be used in effectively separating H_2 and/or CO_2 from mixtures with CH_4 and N_2. The study further demonstrates how chemical affinity and size exclusion behaviour of the adsorbents and membrane materials can be manipulated to achieve the targeted separation and match the application via charge, strain or structure tuning.

LIST OF PUBLICATIONS

- **De Silva, S. W.**, Senadeera, W., Du, A., & Gu, Y. (2014). Neutral and charged boron-doped fullerenes for CO_2 adsorption. *Beilstein J Nanotechnol*. 5: 413–418.
- **De Silva, S. W**., Du, A., Senadeera, W., & Gu, Y. (2017). Strained graphitic carbon nitride for hydrogen purification. *Journal of Membrane Science,* 528, 201-205.
- **De Silva, S. W.**, Senadeera, W., Du, A., & Gu, Y. (2017). Multi-scale simulation of strained C_2N membranes for CO_2 capture and H_2 purification (Under preparation)
- **De Silva, S. W.**, Senadeera, W., Du, A., & Gu, Y. (2017). Porous hexagonal boron nitride membranes for gas separation (Under preparation)
-

Conferences attended

- **De Silva, S. W.**, Senadeera, W., Du, A., & Gu, Y. (2014). A molecular dynamics simulation of CO_2 separation from flue gas with graphyne membranes. Presented at The 5th International Conference on Computational Methods (ICCM2014), Cambridge, England.
- **De Silva, S. W.**, Senadeera, W., Du, A., & Gu, Y. (2015). A molecular dynamics simulation study of gas separation with graphene oxide framework membranes, The 2nd Australasian Conference on Computational Mechanics (ACCM 2015), Brisbane.

TABLE OF CONTENTS

Keywords v

Abstract vi

List of publications ix

Table of Contents x

List of Figures xiii

List of Tables xvii

List of abbreviations xviii

Acknowledgment xix

CHAPTER 1 Introduction 1

1.1 Research Background 1

1.2 Research Problem 4

1.3 Research Aims and Objectives 5

1.4 Significance and Contributions 6

1.5 Thesis Outline 8

1.6 Framework of the research 10

CHAPTER 2 Literature review 11

2.1 Membrane separation 12

2.1.2 Nanoporous membranes for gas separation 15

2.1.3 Strain tuning 23

2.2 Adsorption separation 23

2.2.1 Charge controlled CO_2 adsorption 25

2.2.2 Fullerenes doped with a single B atom 25

2.3 Summary and research gaps 26

CHAPTER 3 Methodology 29

3.1 Quantum Mechanics 31

3.1.1 Semi-Empirical Methods 32

3.1.2 Ab initio Methods 32

3.1.3 The Density Functional Theory 32
3.1.4 Basis-sets 35
3.1.5 Software 38
3.2 Molecular Mechanics 39
3.2.1 Molecular Dynamics Simulations 39
3.2.2 Molecular Dynamics Simulations Theory 40
3.2.3 Algorithms 44
3.2.4 Equilibrium Ensembles 47
3.2.5 Thermostats and barostats 48
3.2.6 General simulation procedure 48

CHAPTER 4 Carbon dioxide capture by charge controlled boron doped fullerene 53
4.1 Introduction 53
4.2 Computational details 54
4.3 Results and discussion 55
4.3.1 CO_2 Adsorption on uncharged BC_{59} fullerenes 56
4.3.2 Effects of charges on the structure 57
4.3.3 CO_2 adsorption on BC59 fullerene in 1e − state 58
4.3.4 N_2 and CH_4 adsorption on neutral and charged BC_{59} 61
4.3.5 Discussion 62
4.4 Conclusion 63

CHAPTER 5 Porous hexagonal boron nitride membranes for gas separation 65
5.1 Porous Boron Nitride Structures 66
5.2 Computational Details 67
5.2.1 Density Functional Theory Calculations 67
5.2.2 Molecular Dynamics Simulations 68
5.3 Results & Discussion 70
5.3.1 Gas permeation study 71
5.3.2 Discussion 76
5.3.3 Adsorption and diffusion 77
5.3.4 Gas separation in binary systems 83
5.4 Summary 86

CHAPTER 6 Strained graphitic carbon nitride for hydrogen purification 87
6.1 Introduction 87
6.2 Computational Details 88

6.2.1 First-principles quantum mechanical simulations 88
6.2.2 Molecular dynamics simulations 90
6.3 Results & Discussion 91
6.3.1 Structural simulation results 91
6.3.2 Gas Permeation Results – MD Simulations 93
6.3.3 Gas Permeation Results – DFT Simulations 100
6.4 Conclusion 102

CHAPTER 7 Strain controlled C_2N for hydrogen purification and carbon dioxide separation 103
7.1 Computational Details 104
7.1.1 Density Functional Theory Calculations 104
7.1.2 Molecular Dynamics Simulations 106
7.2 Results 109
7.2.1 C_2N under biaxial strain 109
7.2.2 Molecular Dynamics Gas Permeability Simulation Results 112
7.2.3 Quantum mechanical simulations 124
7.3 Discussion 127
7.4 Conclusion 128

CHAPTER 8 Conclusions and suggestions 131
8.1 Research summary 131
8.2 Limitations 135
8.3 Future directions 136

CHAPTER 9 Bibliography 139

Appendix A xxi

Appendix B xxii

LIST OF FIGURES

Figure 2.1: Robeson's upper bound. 12

Figure 2.2: Porous graphene sheet with N functionalization and H terminations. Atom colour code: C, grey; N, blue; H, white. 17

Figure 2.3: Top view of selected sp1-sp2 hybridized C membranes graphyne, (b) graphdiyne.. 19

Figure 2.4: The g-C_3N_4 building blocks: (a) s-triazene and (b) tri-s-triazene units 20

Figure 2.5: The building blocks of C_2N, (a) HAB and (b) HKH. 21

Figure 2.6: Predicted g-C_3N_3 structure 21

Figure 2.7: Carbon analogues boron nitride nanostructures: (a) h-BN, (b), c-BN and (c) BNNT. Atom colour code: blue, nitrogen; pink, boron 22

Figure 3.1: The Lennard-Jones potential 43

Figure 4.1: Sites for CO_2 adsorption on BC_{59}. The B and C atoms of HH B-C and HP B-C sites are represented as 'ball and bond' type and the rest of the atoms are represented as 'wireframes'. Atom colour code: grey, carbon; pink, boron 55

Figure 4.2: CO_2 physisorbed configuration on neutral BC_{59}. (a) Front view and (b) top view. Atom colour code: grey, carbon; pink, boron; red, oxygen 56

Figure 4.3: LUMO of neutral BC_{59}. The orbitals are drawn at isosurface value 0.02. The colours of the orbitals: red, positive wave function; green, negative wave function. Atom colour code: pink, boron; grey, carbon 57

Figure 4.4: Mulliken charge distribution of (a) neutral BC_{59} and (b) 1e- BC_{59}. The atoms are shaded based on the charge distribution on each atom. The comparison suggests that the most notable charge transfer is on the boron atom 58

Figure 4.5: (a) CO_2 chemisorption and (b) Transition structure for CO_2 chemisorption on negative 1e- charge BC_{59}. Atom colour code: grey, carbon; pink, boron; red, oxygen. (c) Charge distribution after CO_2 chemisorption 59

Figure 4.6: : Intrinsic reaction pathway for CO_2 chemisorption on 1e- charged BC_{59} from its physisorbed configuration. The total energy = 0 point corresponds to the total energy of ECO2+ EBC59 − 1 60

Figure 4.7: The physisorbed configurations of (a) N_2 and(b) CH_4 on a boron doped $C_{59}B$ fullerene. The physisorbed configurations essentially remains the same irrespective of the electric field of the system. Atom colour code: white; hydrogen; pink, boron; grey, carbon; blue, nitrogen. 61

Figure 4.8: Comparison of adsorption energies of each gas type on a neutral BC_{59} fullerene and when the adsorbent is under a (-1) electric field 62

Figure 5.1: (a) Pore-10 and (b) Pore-8. These two pores have similar openings, however the difference in alignment of length of the pore opening along the zigzag edge or the armchair edge make them structurally different and therefore affects its structural stability. Atom colour code: hydrogen, white; boron, pink; carbon, grey; nitrogen, blue. 66

Figure 5.2: Pore-13-B and Pore-13-N. The predominant atom type at the edge of the pore opening distinguish these two similar looking pore openings. Atom colour code: hydrogen, white; boron, pink; carbon, grey; nitrogen, blue. 67

Figure 5.3: Simulation box setup for MD simulations. The length of the simulation box is reduced for illustrative purposes. Atom colour code: white. hydrogen; pink, boron; grey, carbon; blue, nitrogen; red, oxygen. 69

Figure 5.4: Temperature and energy variation during equilibration and production simulations. These results are sample representations from the CO_2 permeation through pore-13-B subjected to 5% biaxial strain 72

Figure 5.5: The variation of number of H_2 molecules and (b) the number of H_2 crossing events occurred during the simulation period for membrane systems under no strain. Since the pore-10 is impermeable to H_2 in the absence of strain, the plot is on the y=0 axis 74

Figure 5.6: Comparison of gas permeability of Pore-13-B under 5% strain. (a) Variation of number of crossings recorded during the entire simulation period. (b) Number of gas molecules in the permeate side during the simulation period 76

Figure 5.7: The probability distribution of the gases along the Z-direction perpendicular to the membrane. The figure shown here is the results from gas permeation study of pore-13-B under 5% biaxial strain. 77

Figure 5.8: Snapshots of membrane and adsorption zones at the end of simulation for each gas type. The contrast in adsorptive behaviour is clearly visible. Atom colour code: hydrogen, white; boron, pink; carbon, grey; nitrogen, blue, red; oxygen. 78

Figure 5.9: A typical molecular trajectory of H_2 and CH_4 respectively. The membrane is positioned at the centre where Z=0. 79

Figure 5.10: Comparison of simple crossing vs bulk crossings. Here a simple crossing is considered when a gas molecule simply crosses the membrane from one side to the opposite side, while bulk crossing represents when a gas molecule crosses from the bulk zone of one side to the bulk zone of the opposite side. The comparisons shown here are that of the CO_2 and CH_4 gas molecular permeation through a membrane with pore-13-B under 5% biaxial strain 81

Figure 5.11: The summary of gas flux through the membrane 82

Figure 5.12: Comparison of gas permeation in pure gas simulation systems of H_2 and CO_2 with permeation in an equimolar mixture of the two gases 84

Figure 5.13: (a) The normalized probability distribution of gas molecules around the membrane area for H_2 and CO_2. The figure compares the concentration in pure gas simulation system with the binary gas simulation system. (b) The summary of number of crossings in each system for each gas 85

Figure 6.1: The simulation setting for TS search calculations (a) Side view, (b) Top view. Atom colour code: white, hydrogen; grey, carbon; blue, nitrogen 89

Figure 6.2: (a) Top view of the 5x5 nm, g-C_3N_4 membrane. (b) Illustration of simulations model. Atom colour code: grey, carbon; blue, nitrogen; yellow, hydrogen 90

Figure 6.3: Depiction of structural properties and charge distribution obtained from DFT simulations 91

Figure 6.4: 2x2 supercell of g-C_3N_4. The bonds and distances are labelled. Atom colour code: grey, carbon; blue, nitrogen..... 92

Figure 6.5: (a) Temperature and (b) energy variation during the production part of the simulation. The kinetic energy in (b) is scaled in y-axis on the right side, while total energy and potential energy are represented on the y-axis on the left hand side. 93

Figure 6.6: Variation of total number of crossings at the end of 10 ns simulation time, with the reservoir pressure..... 94

Figure 6.7: (a) Variation of fraction of gas molecules on the permeate side with time, the concentration remains zero for CO_2 and CH_4 (b) The number of H_2 crossings events through the membrane in both directions vs time 95

Figure 6.8: Illustrative snapshots of the system at the end of the 10 ns MD simulations for (a) unstrained system with H_2. System under 5% strain with (b) H_2, (c) CO_2 and (d) CH_4. The results indicate how even under a 5% strain the g-C_3N_4 membrane is impermeable to CO_2 & CH_4, and the significant improvement of the H_2 permeability under strained conditions in comparison to the unstrained membrane. Atom colour code: grey, carbon; blue, nitrogen; yellow, hydrogen; red, oxygen. 96

Figure 6.9: Summary of variation of H_2 flux with alterations to the feed side pressure and membrane strain 97

Figure 6.10: Comparison of number of crossings occurred during the first 2.5 ns of simulations carried out using a 0.4 fs time step with simulations using a 0.1 fs time step..... 98

Figure 6.11: (a) Comparison of variation of gas permeability calculated based on Type I and Type II crossings. (b) Graphical illustration of Type I and II crossings..... 99

Figure 6.12: The comparison of data analysed from trajectories obtained (a) every 50 fs and (b) every 200 fs..... 100

Figure 6.13: (a) The energy variation along the gas transport pathway, (b) Snapshots of H_2 physisorbed at state I transition state (TS) and state II. Atom colour code: grey, carbon; blue, nitrogen; yellow, hydrogen 100

Figure 7.1: A 4×4 monolayer of 2D-C_2N 103

Figure 7.2: The simulation setup for energy scan of a gas molecule penetration through a pore opening. (a) The top view of a CO_2 molecule placed along the centre axis of the pore opening perpendicular to the membrane, (b) the side view of a CO_2 molecule placed. The distance between the membrane plane and the gas molecule is varied to scan the energy variation along the gas molecule pathway. 105

Figure 7.3: A typical simulation setup used in molecular dynamics simulation. The membrane is placed at the centre of the simulation box and the gas molecules were initially placed at one side of the box known as the reservoir. The simulation box is periodic in x and y directions and has a reflective boundary conditions in the z-direction. In this image, the length of the simulation box is reduced in half for illustrative purposes. The atom colour code: yellow. Hydrogen; blue, nitrogen; grey, carbon. 106

Figure 7.4: Fully relaxed structure of C_2N 110

Figure 7.5: Charge distribution on C_2N, calculated using Mulliken charge distribution analysis 110

Figure 7.6: A fully optimized C_2N structure under biaxial strain. The distance shown in the image is the point-to-point distance between two nitrogen atoms directly facing each other. 111

Figure 7.7: The variation of structural parameters with increasing biaxial strain 112

Figure 7.8: Number of crossings of H_2 and CO_2 gas molecules across the membrane in both directions under (a) 5% and (b) 7% biaxial strains respectively 114

Figure 7.9: Variation of number of H_2 and CO_2 gas molecules on the permeate side of the membrane. These figures compare the number of gas molecules for membranes under 5 and 7% biaxial strains respectively. 115

Figure 7.10: Probability distribution of gas molecules, along the Z-axis of the membrane. The membrane is placed at the centre where z=0 in the simulation box. The reservoir side is the negative side of the z-axis and while the permeate side is on the positive side. The N_2 and CH_4 gas molecules have zero probability on the permeate side. These results correspond to simulation systems under 5% biaxial strain 116

Figure 7.11: The probability distribution of gases from 1 nm (10 Å) from the membrane in both directions 117

Figure 7.12: The probability distribution of (a) H_2 and CO_2 in the x and y directions for gas molecules within the membrane and adsorption zones. The shaded dark blue and grey areas represent the nitrogen and carbon atoms of the membrane. 119

Figure 7.13: A typical trajectory of a gas molecule during the 10ns simulation period. these trajectories are representative of molecular simulation of membranes under 5% biaxial strain 120

Figure 7.14: A typical trajectory of a CO_2 molecule in the membrane system under 7% biaxial strain 121

Figure 7.15: The (a) top view and the (b) side view of the PES calculation setup. The position of the geometric centre of the gas molecule was varied from 0 to 10 w.r.t the membrane and energy calculations at each position was performed 124

Figure 7.16: Energy profile for a gas molecule along the adsorption height for C_2N membranes under (a) 5% and (b) 7% biaxial strain 124

Figure 7.17: The comparison of potential energy scan along various points of the Z-axis and TS search calculations 127

LIST OF TABLES

Table 2.1: Kinetic diameters of the gas molecules 14
Table 3.1: Comparison of basis sets for optimization and evaluation 38
Table 5.1: Summary of structural changes induced by biaxial strain 71
Table 5.2: Summary of number of crossing for each gas type through the studied pore types 73
Table 5.3: Summary of calculated gas flux 81
Table 6.1: Effect of biaxial strain on g-C_3N_4 structure 92
Table 7.1: Summary of force field data used in MD simulations 109
Table 7.2: Structural changes induced on C_2N structure by increasing strain values 111
Table 7.3: Number of crossings across the membrane 113
Table 7.4: The normalized position of the adsorption layer for each gas type 118
Table 7.5: Summary of Gas permeation and flux 123
Table 7.6: Summary of energy barriers 126

LIST OF ABBREVIATIONS

B3LYP	Becke-3 Parameter Lee-Yang-Parr Method
BSSE	Basis Set Superposition Error
CCS	Carbon Capture and Storage
CTF	Covalent Triazene Framework
DFT	Density Functional Theory
GGA	Generalized Gradient Approximation
HF	Hartree Fock
IRC	Intrinsic Reaction Coordinate
LDA	Local Density Approximation
LST	Linear Synchronous Transit
LUMO	Lowest Unoccupied Molecular Orbitals
MD	Molecular Dynamics
MEP	Minimum Energy Pathway
MOF	Metal Organic Framework
PBE	Perdew-Burke-Ernzerhof Method
PES	Potential Energy Scan
PPPM	Particle Particle Particle Mesh
QST	Quadratic Synchronous Transit
STQN	Synchronous Transit-Guided Quasi-Newton
TST	Transition State Theory
VDW	van Der Waals
WFT	Wave Function Theory

ACKNOWLEDGMENT

First and foremost, I would like to express my sincere gratitude and appreciation to my advisor, Professor YuanTong Gu for offering me invaluable guidance and support. My gratitude extends to the supervisory committee, Dr. Wijitha Senadeera and A/Prof. Aijun Du for the continuous support and guidance to achieve the successful outcomes of the study.

My heartfelt gratitude goes to the Queensland University of Technology for providing financial assistance during the study and world-class supercomputer facilities to carry out my research modelling work. I appreciate all the support offered by the administration and academics, which made me, reach my goals.

I take this opportunity to thank my beloved husband and our families for giving me endless love and courage and being there for me all the time. Finally, I thank all my colleagues and friends for all the support and corporation provided.

CHAPTER 1 INTRODUCTION

This chapter outlines the background and the hypothesis of this research, its objectives, the significance and importance of the study. Section 1.1 introduces the research background, next section 1.2 outlines the research problem, where section 1.3 presents the objectives of this research, and section 1.4 describes the significance and the contribution of this research. Finally, section 1.5 gives a brief overview of the thesis, and section 1.6 presents the developed framework of the research.

1.1 RESEARCH BACKGROUND

Nanotechnology is the manipulation of matter on an atomic and molecular level. The bottom-up approach involves assembly of atoms and molecules in to precise structures with explicit functions to meet specific requirements. The ability to manipulate matter at atomic level has opened up a completely new array of possibilities. Motivated by recent advances in many fields owing to nanotechnology, which offers precise molecular tuning to match the expected outcome, this study aims to exploit this ability to further industrial gas separation techniques, specifically targeting gas purification for cleaner energy production.

Despite growing interest in environmental sustainability, continuous dependence on fossil fuel combustion has increased atmospheric carbon dioxide concentrations beyond natural limits over the last two centuries. Among the greenhouse gases, carbon dioxide is the primary pollutant gas due to large number of annual emission where fossil fuel combustion accounts for 60% of the total carbon dioxide emissions by human activity [1]. The atmospheric CO_2 concentration has changed from 278ppm in 1750 to 390.5ppm in 2011, which is an increase of about 40%. Each year, 29 Gt of CO_2 is released to the atmosphere which is 85% of the total greenhouse gas emissions [2]. Accepted international standards state that the cumulative emission for the 2000-2050 period should not exceed 1500 billion tonnes, to limit the global temperature rise to 2°C above pre-industrial times. However, the current global CO_2 emission trends shows that cumulative emission will surpass the target within the next two decades [3].

To address the continuing increase of atmospheric CO_2 levels, the preferred approach is to replace fossil fuels with alternative cleaner energy sources or to make fossil fuel energy more efficient and cleaner. Especially, switching towards energy sources with greater efficiency can address the global climatic crisis in the long term. Hydrogen as an energy source offers a superior and more attractive alternative to conventional fossil fuel combustion, owing to its high energy density [4], higher energy conversion efficiency and its environmental friendly nature [5]. Hydrogen burned with oxygen releases energy, which can be utilized with more efficiency, emitting only water as a waste product. Hydrogen energy is commonly found in applications of fuel cells, power vehicles, internal combustion engines, and spacecraft. Current H_2 production methods include, steam-methane reforming, coal gasification, water-electrolysis etc. [6]. Irrespective of the production method, a critical step common to every method is a hydrogen purification step from a mixture of gases.

Regardless the continuous attempts to move towards sustainable energy generation, fossil fuel combustion continues to be the main source of electricity [2], releasing CO_2 to the atmosphere. Therefore carbon dioxide capture and storage (CCS) technologies have also gained the interest of many researchers [7] as a solution to limit the amounts of CO_2 released to the atmosphere. This technology offers a reasonable midterm solution to the continuous increase of atmospheric CO_2 concentrations. Capturing CO_2 from the exhaust of a power plant where the CO_2 concentration is 12 mol% is much more efficient than in direct air capture (DAC) where the CO_2 concentration is as low as 0.039 mol%. On average, 11000 tons of CO_2 is emitted by a 500MW power plant per day [8]. The existing coal fired power plants emit about 2 billion tons of CO_2 per year [9]. Considering these factors, power plants are the most efficient candidate to implement CCS technology. Therefore CO_2 capture technologies that can be retrofitted to existing power plants and designed into new plants with 90% of CO_2 captured and stored, while limiting the increase in total cost of electricity generation to no more than 35% [10] are of significant importance.

The most widely used methods for gas separation in industrial applications are cryogenic distillation, solid absorption and stripping by chemical based solvents. The main drawback of

these methods is the high energy consumption [7]. Especially in post-combustion carbon capture, amine based solvent absorption is the most commonly used method, which consumes high amounts of energy to regenerate the solvent. This has driven many researchers to look for alternative types of technologies. Nanomaterials that boast size controlled properties such as adsorption capacities, selectivity, and high surface area have gained much attention due to these inherent favourable characteristics.

Among numerous gas separation techniques, membrane separation is regarded as superior, due to its intrinsic low energy requirements, simple operation [11] and higher tunability. Membrane technology for gas separation mainly exploits the difference in molecular size between the targeted gas and other mixture gases. Among various membrane types, such as polymeric [12], inorganic [13-15], and hybrid types [16]; graphene and graphene-like two-dimensional membranes have attracted greater interest due to their atomic thickness. A membrane's performance is measured by its selectivity and permeability, which normally shows inversely proportional behaviour to each other. Atomically thin single layer 2D material, which has the ultimate thinness, is known to exceed this limitation. Therefore, porous graphene [17-25] and graphene-like materials such as graphynes [26, 27], graphitic carbon nitrides [28, 29] have been explored for gas separation applications.

Similarly, adsorption is considered as an energy efficient method in gas separation applications. The desorption and the adsorbent regeneration steps is less energy intensive compared to the absorption process. Similar in membrane separation applications, low dimensional graphene and graphene-like nanomaterials offer a superior alternative to conventional adsorbent materials due to their chemical tunability for targeted gas adsorption, larger surface area for high efficiency, and excellent chemical and mechanical stability [30, 31], which facilitates cyclic use in industrial conditions.

As with graphene, other graphene-like materials such as boron nitride; carbon nitrides; phosphorene; MoS_2 and other similar transition metal dichalcogenides; and low dimensional

carbon allotropes such as fullerene, carbon nanotubes, graphyne etc. have gained much attention. These nanomaterials potentially have tuneable size controlled properties that could precisely match intended applications. It is therefore possible to tailor adsorption capacities, selectivity, and high surface area in the case of solid adsorbents. On the other hand, tailoring the pore size, shape or chemical affinity, enable the preferential passage of specific gas species through a membrane while rejecting the rest of the species in the mixture.

1.2 RESEARCH PROBLEM

Gas separation is a vital step in many industrial processes. Hydrogen purification for hydrogen production as an energy source, or removal of CO_2 from the flue gas stream are two common instances that require a particular gas to be separated from a gaseous mixture. Adsorption separation and membrane separation are two preferred gas separation methods. Especially low dimensional carbon-based nanomaterials and other analogous materials have proven to be promising candidates for use in membrane and adsorption separation technologies. Many nano-adsorbent and nano-membrane based studies are largely concentrated on graphene-based materials, where significant work is still expected. Using other low-dimensional carbon-based materials and graphene-like nanomaterials in industrial gas separation applications for cleaner energy production offers significant prospects too. However, the studies on how tunability of nanomaterials can be exploited to advance the separation efficiencies of nano-membranes and adsorbents are limited. While the majority of the limited studies are devoted to chemical tuning, other tuning approaches, such as charge tuning and mechanical tuning for improving adsorbent performance, size exclusion and chemical affinity, are scarce. Based on these, this thesis attempts to answer the following questions:

- What low dimensional carbon-based and graphene-like materials can be effective gas separation adsorbents or membranes, especially targeting CO_2 separation and H_2 purification in applications related to cleaner energy generation?
- What novel techniques can be explored to 'tune' these materials beyond conventional means to precisely match the targeted application, i.e. to separate the exact gas molecules

from a gaseous mixture; to improve the separation efficiencies and to improve operational productivities?

1.3 RESEARCH AIMS AND OBJECTIVES

The main aim of this thesis is to explore and evaluate the gas-separation capability of low dimensional nanomaterials for selective adsorption, membrane separation, and adsorptive membrane separation using first-principles quantum mechanical simulations and classical molecular dynamics simulations or a combination of both. This research focuses on hydrogen separation from carbon dioxide and methane, which finds applications in H_2 production as an energy source, and pre-combustion carbon capture[1] for controlling carbon dioxide emission from fossil fuel combustion; and carbon dioxide separation from nitrogen, and methane significant in flue gas purification and natural gas sweetening, respectively. Furthermore, the research evaluates possible novel techniques to enhance the separation properties and efficiency of the studied low dimensional nanomaterials by focusing on tuning the materials with three approaches: chemical tuning, charge tuning and mechanical tuning. The major specific objectives of this research were:

- To study the selective CO_2 adsorptive behaviour over N_2 and CH_4 of boron-doped fullerenes, which has excellent thermal and structural stability. The study evaluated the effects of altering the charge state of the system on the selective CO_2 adsorption. First-principles DFT simulations, with a suitable solving technique were used to simulate and analyse the chemical and/or van der Waals interactions, and charge transfer between molecules
- To evaluate CO_2/ N_2, CO_2/CH_4, H_2/CO_2 and H_2/CH_4 separation capability of two-dimensional single layer boron nitride membranes with introduced sub-nanometre pores, for a number of pore structures and to establish how altering the chemical

[1] pre-combustion carbon capture- this is a two step process where (i) the fuel is partially oxidised in a synthetic gas mixture (H_2, CO and CO_2) (ii) the CO_2 is then separated from H_2 which is fed as clean fuel.

structure can be used to tune the gas separation performance of the membrane. In addition, the study aims to evaluate the possibility of enhancing the gas separation performance or altering the selective trends of the membrane using mechanical tuning. Specifically, a study of the effectiveness of strain controlled mechanical alterations of the nanopore, to change and/or improve the membranes' permeability and the targeted gas selectivity was included. A combination of *ab initio* DFT simulations and MD simulations were used for geometry optimisations and gas permeability study respectively.

- To evaluate the capability of atomically thin, graphitic carbon nitride (g-C_3N_4) monolayers for H_2 purification from gaseous mixtures of CO_2 and/or CH_4 using a combination of DFT and MD simulations. In addition, the effects of altering the operation conditions, specifically the effects of system pressure on the separation efficiency and the effects of external biaxial strain on the membrane's performance were evaluated.

- To evaluate the H_2 purification and CO_2 capture from N_2 and CH_4 by 2D-C_2N membranes. As in the previous study, the possibility of improving the membranes performance by strain tuning was explored. A combination of *ab initio* DFT simulations and classical MD simulations were used to achieve this objective and explain the research findings.

- To establish an understanding of the relationships between the different gas molecules and the separation material; and the inherent properties of the nanomaterials which contribute, or hinder superior gas separation, which can be a benchmark in predicting the gas separation capabilities of other similar materials, or a factor in design and synthesis of novel materials.

1.4 SIGNIFICANCE AND CONTRIBUTIONS

From the first-principles DFT simulations and molecular dynamics (MD) simulations, on the targeted applications, the following distinctive contributions can be identified.

- In this research, the effect of boron doping of fullerene to enhance interactions with CO_2 is studied. Our studies show that doping fullerene with a single boron atom does not lead to

a significant increase in the CO_2 adsorptivity. In the course of this study, it was found that adding an electron to the system causes CO_2, which is a Lewis acid that prefers to accept electrons to bond with the BC_{59}^{-1}. These results predict a chemically and mechanically stable, adsorbent material for CO_2 capture. They also give deeper understanding about the interaction of CO_2 with B-C systems that can be the basis for future research.

- Here, we present the gas separation behaviour of hexagonal boron nitride membranes with created pores. This study identifies which gases can be separated, the effects of various pore structures on the separation efficiencies and what characteristics of the pore structure affect the gas separation performance. The findings of this study benefit design of porous boron nitride membranes. The new knowledge garnered can be used to guide the design of similar membranes and predict the gas separation effects. It is anticipated that the research findings may foster deeper research interest in cheaper large-scale synthesis techniques to create precise pore openings with controlled size.
- In this thesis, the gas separation characteristics of two graphene-like carbon nitride materials: C_3N_4 and C_2N were studied. The study details how the physical and structural properties influence the membranes' outstanding performance. This knowledge may directly benefit in applications of H_2 and CO_2 separation, and it may also motivate further research in 2D carbon nitride materials
- Here, we study how structural tuning (boron doping on C_{60} fullerene, pore structure of the boron nitride membrane), charge tuning and strain tuning can be used to improve gas membrane's separation efficiency.
- The simulation models and techniques used in this study should be applicable in future studies of similar interests.

Overall, the reduction of greenhouse gases is becoming increasingly important. In 2004, the Australian government issued a White Paper on Energy outlining the national strategies for reducing greenhouse gas emissions. The key strategies of the paper were the capture of CO_2 from

stationary emissions and subsequent storage in geological reservoirs while gradually increasing the use of alternative energy sources including hydrogen. This research gives insights in to possible mechanisms for CO_2 removal from flue gas and H_2 purification in energy applications. The effectiveness of such approaches for reduction in greenhouse gas emissions rely on the efficiency in the processes, and this research presents separation techniques that have significantly high theoretical separation efficiencies.

1.5 THESIS OUTLINE

This section presents a brief outline of the chapters of this thesis.

- In chapter 1, an introduction to the research was presented with a discussion of the research background and research context. It also detailed the aims and objectives, significance and contribution of the research and is followed by the graphical representation of the framework of the research
- Chapter 2 presents a comprehensive literature review. This chapter is divided into two sections. The first section discusses membrane technology and current advances in this field. The second section details adsorption gas separation and a review of nano-adsorbents and research findings in this area.
- Chapter 3 introduces available simulation techniques, followed by a detailed presentation of the theoretical basics of *ab initio* DFT and classical MD simulations. A brief description of molecular sample preparation, simulation setup & settings are also introduced.
- In Chapter 4, a theoretical study of CO_2 separation from N_2 and CH_4 using boron doped C_{60} fullerene is given. The chapter investigates the effects of altering the charge state of the system on separation efficiency.
- In Chapter 5, a theoretical study of gas separation using porous boron nitride membranes is presented. The study details how different pore openings and strain affects the membrane separation efficacy to achieve H_2/ CO_2 and CH_4 separation and CO_2/N_2 and CH_4 separation.

- Chapter 6 presents a theoretical study of g-C_3N_4 for H_2 purification from CO_2 and CH_4. The chapter details the effects of strain tuning and feed pressure on membrane efficiency.
- In chapter 7, a gas permeability study of C_2N under strain is presented. It evaluates the effects of strain on gas permeability and how chemical characteristics of the membrane material affect the separation efficiency. It details the H_2 and CO_2 separation from CH_4 and/or N_2.
- Finally, in Chapter 8, the major conclusions of the research, limitations and recommendations for future work are presented.

1.6 FRAMEWORK OF THE RESEARCH

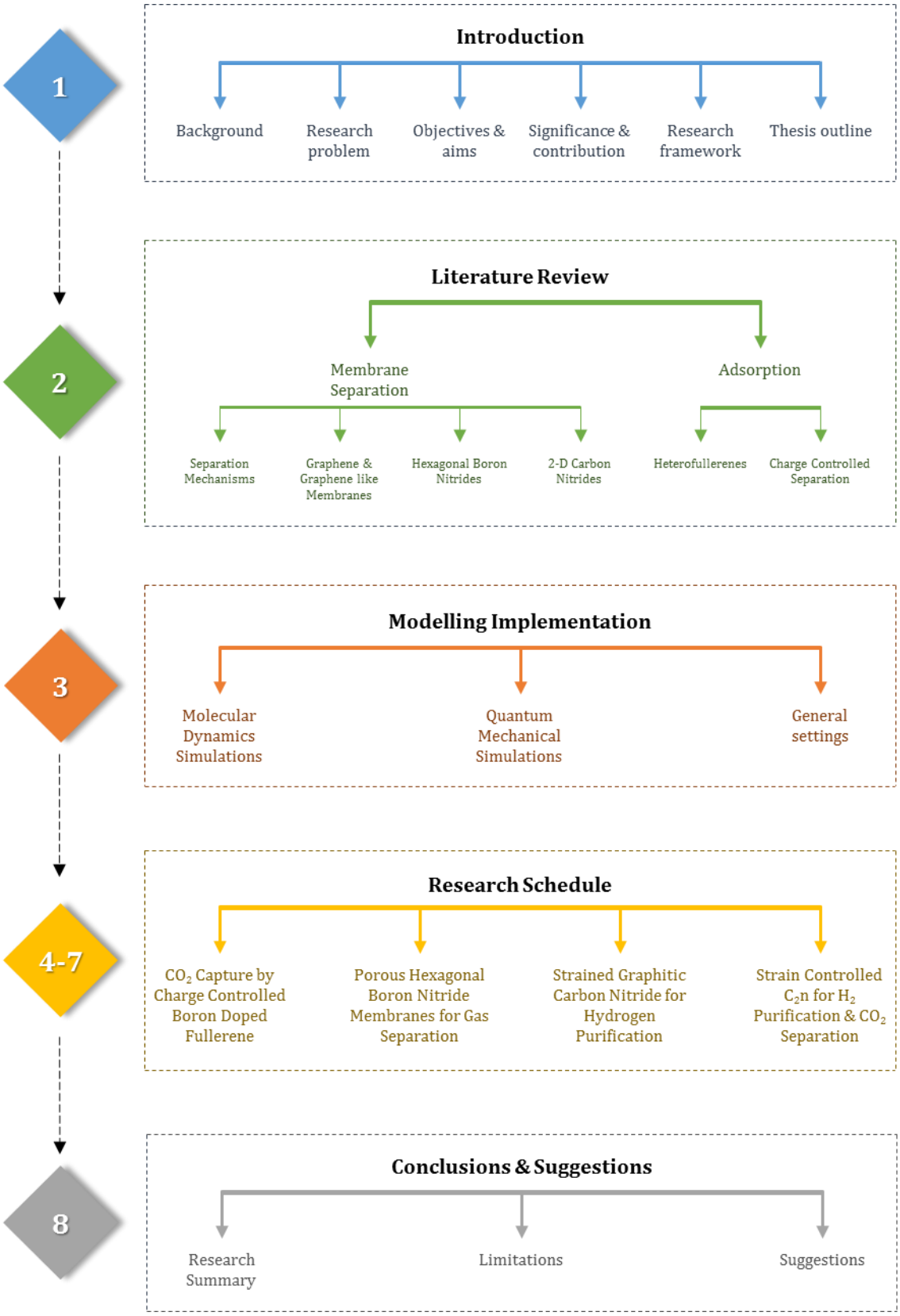

CHAPTER 2 LITERATURE REVIEW

Gas separation is a common process found in many industrial applications. Various techniques exist for gas separation such as cryogenic distillation, stripping by chemical solvents, adsorption on solid adsorbents, membrane separation, etc. The commonly used conventional methods for gas separation are cryogenic distillation and chemical stripping with solvents. However, these methods have operational limitations, for example, excessive energy consumption; operational limitations such as corrosion, foaming and chemical degradation; slow uptake rates; large equipment requirements [7]. Furthermore, in chemical stripping, an added energy intensive step to regenerate the solvent in downstream processing is required, which is caused by the strong chemical interactions between the amines (used as the chemical solvent) and CO_2 gas. Cryogenic distillation especially in H_2 production and CO_2 capture is not considered due to the high-energy requirements and the low efficiency in separating dilute gas mixtures. This type of process is suitable for gas separation only in large-scale air separation applications such as oxygen, nitrogen and argon purification.

Membrane separation offers an energy efficient alternative for gas separation compared to chemical separation by absorbents. This method does not require an energy intensive regeneration process [32] and the required pressure drop across the membrane to achieve separation, is low. The disadvantage of membrane separation for small sized gas purification is that the separation efficiency of traditional membranes is poor, where only a fraction of gas is recovered and that fraction suffers from lower purity [32]. Similarly, adsorption has a higher energy efficiency compared to other methods, since solid adsorbents do not bind gases as strong as chemical absorbents and therefore the desorption process is less energy intensive compared to the absorption process. As aforementioned, membrane separation and adsorption, processes can benefit immensely due to the advances made in nanotechnology. The ability to design materials to target the focus gas species can improve the separation efficiency tremendously. The literature review of this thesis is divided to two sections; gas separation by membrane separation

and adsorption separation. Each section includes a brief overview of the process and a review of recent developments in the field, focusing on the use of nanotechnology to precisely manipulate/control the targeted outcome.

2.1 MEMBRANE SEPARATION

A membrane is a semi permeable barrier that passes some species in a mixture while retaining the rest. Membrane technology is widely used for gas separation applications and is expected to be more efficient than other separation processes [33]. This method offers engineering and economic advantages [9] and offers easy integration in to an existing process plant. Membrane separation involves low energy consumption; simple, compact and cheaper instalment; and continuous operation [34]. The most significant advantage of gas membrane separation is that this method does not require chemical additions and therefore a regeneration step is not required. Many different types of membranes such as polymeric, metallic, zeolite and carbon-based membranes have been studied and used for H_2 and CO_2 separation [12-14, 16, 35-46].

The potential use of a membrane for a given application depends on its selectivity towards the targeted gas and the molecular diffusion rates. An efficient membrane should have both high selectivity and high permeability [47, 48]. However these two factors are counter related and the relationship is illustrated in the following diagram with the upper bound known as the Robeson's upper bound [49].

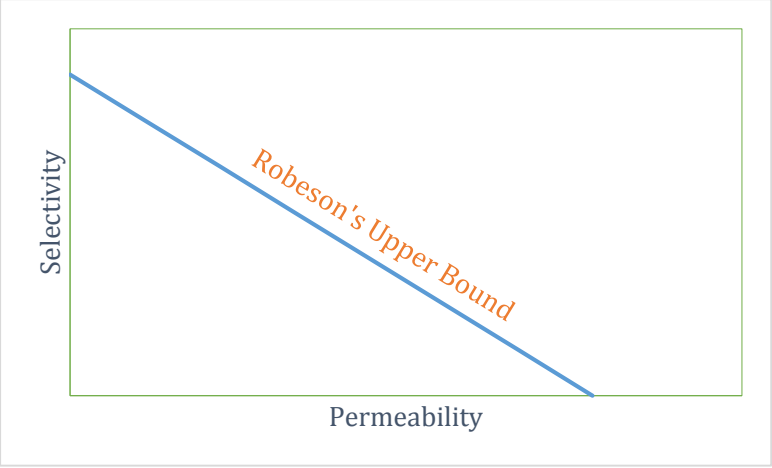

Figure 2.1: Robeson's upper bound.

The diffusion of a given species through a membrane depends on the membrane's chemical and physical properties; the nature of the permeant; and the interaction between the membrane and permeant, known as the sorptivity/solubility of the gas in the membrane. The main limiting factor to the use of membranes for gas separation is a lower pressure and concentration of the desired gas in the gas mixture stream, demanding membranes with higher selectivities. The other challenges of using membranes for gas separation are [9] :

- Low concentrations of separation gas mean excessive volumes of gasses to be handled
- The temperature sensitivity of membranes, require the gas mixture to be cooled in upstream processing. An example is in carbon capture; the flue gas has to be cooled down before it is sent through the membrane
- Membranes should be chemically resistant to the constituents of the flue gas and syngas

An ideal membrane for gas separation should possess: [9, 50]

- High separation gas permeability
- High gas selectivity
- Thermal and chemical resistance
- Plasticisation resistance
- Aging resistance
- Cost effective

There are number of mechanisms for gas separation in membranes and given the nanoscale of the membranes investigated in this thesis, three mechanisms of separation can be highlighted as size sieving, chemical affinity sieving and quantum sieving [51].

2.1.1.1 Size sieving

In size sieving, molecules smaller than pores will permeate through the membrane while the larger molecules will be excluded [51]. The challenge with small gas separation is that the kinetic

diameters of the targeted and impurity gas molecules lie within a similar range. Table 2.1 summarizes the molecular diameters of the gases studied here as reported by Breck [52] and the updated diameter [53]. As an example, in the context of CO_2 separation from N_2 post-combustion capture, the membrane geometric pore size should be between the kinetic diameters of CO_2 and N_2, which are 3.3 and 3.64 Å, respectively.

Table 2.1: Kinetic diameters of the gas molecules

Gas	Kinetic diameter (Å)	Updated diameter (Å)
H_2	2.89	2.875
CO_2	3.3	3.325
N_2	3.64	3.568
CH_4	3.8	3.817

The main challenge with this mechanism is the difficulty in controlling the pore size in membrane materials, as larger pores created would reduce the theoretical selectivity of the membrane. Size sieving is the most common mechanism used in gas separation, which is especially suited in helium separation and hydrogen purification. Details of recent research in size exclusion-based gas separation are given in sections 2.1.2.1 to 2.1.2.4.

2.1.1.2 Chemical affinity

When the pore size of the membrane is larger than both species, the difference in chemical affinity can be exploited for separation. A strong affinity between the penetrant gas and the nanopores walls often leads to surface diffusion of the penetrant, which preferentially adsorbs on the pore wall. This results in an enhanced flux through the membrane for that species, however, interactions between the penetrant and pores should not be too intense, as it will strongly adhere on the pore, blocking further molecular movement and necessitating an energy intensive desorption step. In gas separation, membranes can be chemically modified with functional groups which prefer the targeted gas to the other impurity gases.

2.1.1.3 Quantum sieving

Quantum sieving occurs when isotopes with identical size and adsorption properties, preferentially adsorb the heavier isotope due to the lower zero-point energy. This effect is more dominant at lower temperatures [51].

2.1.2 Nanoporous membranes for gas separation

Based on the aforementioned three mechanisms, numerous studies have been carried out to design/evaluate the separation efficiency of nano-membranes. The controllable size properties and chemical properties give nano-membranes the edge over conventional membranes. The two approaches to synthesise nano-sieves are to create pores on existing pristine layered nanomaterials in a top-down approach or to take a bottom-up approach of molecular assembly of unit-cells, such that the assembled material will contain inherent pores. The two approaches have their own strengths and weaknesses. The latter offers uniformly distributed regular inherent pores and hence more precise synthesis of the membrane material. Conversely, the former lends more tunability over pore size and chemical functionalization, but suffers from difficulty in controlling uniformity of the pore size and pore distribution, which can affect the selectivity of the membrane. Sections 2.1.2.1 to 2.1.2.4 present recent studies in using two-dimensional nanomaterials as membranes, designed based on these two approaches.

2.1.2.1 Porous graphene membranes for gas separation

Since its discovery in 2004, graphene [54] has garnered tremendous progress and research interest. It has been commercially synthesized in single or few layer graphene on large areas [55, 56] and 30 inch sheets transferred on a roll-to-roll basis [57] suggesting it is feasible for commercial production. The thickness of conventional membranes ranges from tens of nanometres to several micrometres. This affects the permeance of the membrane since the permeance is inversely proportional to the thickness of the membrane [21, 38]. The perfect membrane should have minimal thickness to maximize flux and high mechanical strength to avoid fracture under high pressure [22]. Therefore the atomic thickness of graphene [58] with its excellent mechanical strength [59] (intrinsic failure strength of pristine graphene is 130GP [60])

and chemical stability (can resist oxidation up to 500 °C [61]) makes it the ultimate membrane material.

However, pristine graphene is impermeable to all standard gases [22, 62, 63]. The electron density of the aromatic rings in pristine graphene is strong enough to repel even the smallest gas molecule: helium [21]. Therefore, to employ graphene in membrane separation applications, it is necessary to create openings of controlled size by removing one or more atoms from pristine graphene, which will selectively allow a certain gas to pass through, while being impermeable to the rest. Koenig et al. demonstrated a mechanism of ultra violet induced oxidative etching in micrometre graphene to create pores which can act as molecular sieves [22]. Fischbein et al. [64] successfully demonstrated the use of electron beam of a transmission electron microscope within suspended graphene sheets to punch holes, where the dangling bonds created by the punching, were passivated by nitrogen doping with ammonia.

In contrast to creating pore openings in already synthesized, pristine, graphene layers, an alternative approach of assembling molecular building blocks, to create ordered uniform layers of regularly distributed pore openings too can be used to synthesis holey graphitic structures. Kuhn et al. [65] successfully applied a method of assembling unit cells of polyphenylene to create a carbon based porous two dimensional membranes. Bieri et al. [66] demonstrated the fabrication procedure of porous graphene, by self-assembly of a hexaiodo-substituted molecular building blocks of cyclohexa- *m* -phenylenes (CHP) on a silver surface. The resulting porous graphene exhibited a regular pore size with one missing hexagon per unit and cells terminated by hydrogen atoms.

Studies have predicted that gas permeance of porous graphene is much higher than conventional membranes due to its atomic thickness, and offer excellent selectivities. They are far superior to conventional membranes such as polymer and silica membranes, where the dominant transport mechanisms are bulk solubility and diffusivity [21]. Koenig et al. [22] experimentally found that a sub-nanometre pore of 3.4 Å created through UV/ozone etching can selectively pass CO_2 while

rejecting N_2. Later Liu et al. [18] performed MD simulations to calculate an estimate of the selectivity for CO_2/N_2. They simulated CO_2/N_2 permeance through a similar pore as shown in Figure 2.2, with an opening size of 3.0 Å by 3.8 Å. Their results predicted that it had an ideal CO_2/N_2 selectivity of ~300 with a permeance of 10^5 GPU (Gas Permeation Unit). Similarly, number of other molecular dynamics and first-principles simulations studies have been conducted to study the use of various porous graphene membranes in a number of gas separation applications [17-21, 23, 24, 67-69].

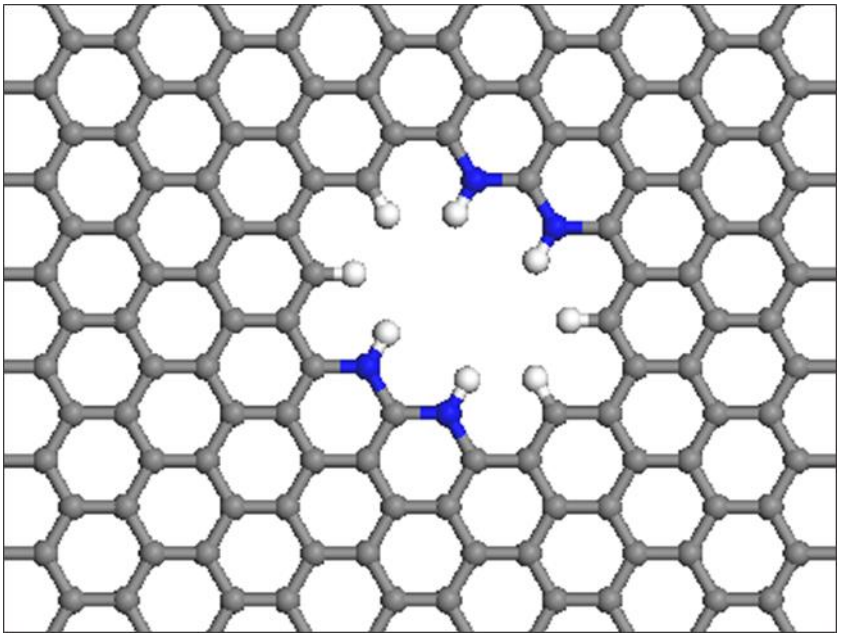

Figure 2.2: Porous graphene sheet with N functionalization and H terminations. Atom colour code: C, grey; N, blue; H, white.

2.1.2.2 Graphene oxide membranes

Unlike pure graphene, GO is not chemically inert or hydrophobic. Studies by Kim et al. [70] focusing on the gas permeability, identified that the potential energy barrier for gas entrance, the tortuosity, layer structure and residual water content, all affect the molecular transport through the GO membrane. They prepared GO membranes using two methods:

- Method I: preparation of several-layer GO membranes by contacting the support membrane surface to the air-liquid interface of a GO solution, followed by spin-coating

- Method II: preparation of thin GO membranes by spin casting of a GO solution on the membrane surface

According to their study, GO membrane prepared by method I had very low CO_2 permeance but the permeance was dramatically increased in the presence of water. The GO membrane prepared by method II had higher CO_2 selectivity in dry conditions but had less permeability. Overall, the functional groups in the graphene oxide leads to altered chemical interactions between the membrane and the gas molecule that affects the overall membrane performance.

2.1.2.3 Graphyne and graphdiyne membranes

This is a new family of carbon allotropes, which like graphene is a flat one atom thin layer. These carbon networks can be viewed as "intermediate" (sp^2 and sp^1 systems between two well-known carbon allotropes: graphene (sp^2 atoms) and carbyne (sp^1 atoms). Graphyne replaces the ($= C =$ $C =$) bond in graphene with uniformly distributed acetylenic linkages($-C \equiv C -$) and in graphdiynes with diacetylenic linkages ($-C \equiv C - C \equiv C -$). For both structures, the networks include two non-equivalent types of carbon atoms. The most interesting property of this class of materials is that the pore size can be adjusted by changing the number of acetylene bonds or diacetylenic linkages (defined as 'n') between adjacent phenyl rings as shown in Figure 2.3. For n = zero, the structure becomes graphene. The resultant membrane will have pores of constant sizes, uniformly distributed across the membrane. This is the advantage of this type of materials over graphene with drilled pores, where achieving uniformly distributed pores of consistent dimensions, could be challenging.

Li et al. [71] have demonstrated a methodology to generate large area (3.61 cm^2) graphdiyne films, on copper substrates via a cross-coupling reaction using hexaethynylbenzene. The successful fabrication of this once-hypothetical material, paved the way for use in practical applications. Some studies have been reported for use of graphynes for separation of H_2 and desalination of water [26, 27, 72-75].

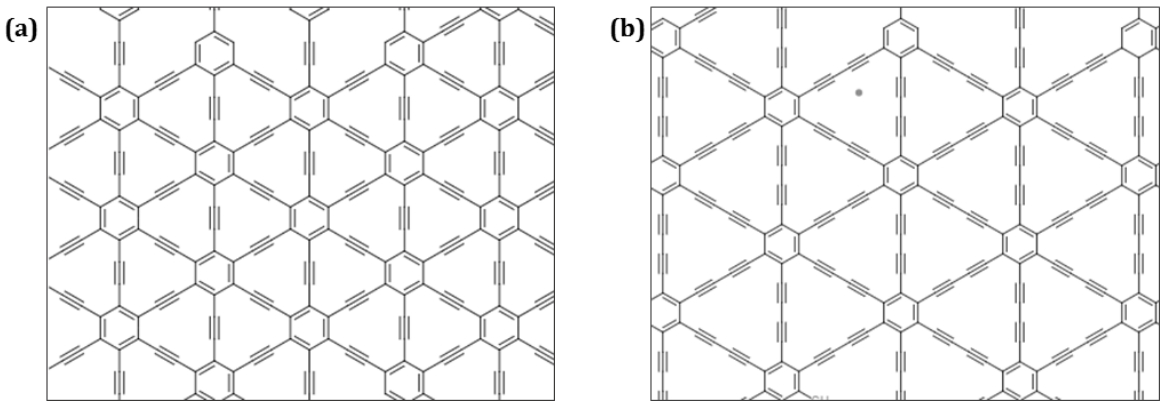

Figure 2.3: Top view of selected sp1-sp2 hybridized C membranes graphyne, (b) graphdiyne.

Altogether, graphene based nano-membranes exhibit superior separation efficiency, and the quest for higher efficiency membranes has been taken beyond graphene and other carbon allotropes based monolayers. The voluminous research on graphene and graphene applications has elicited interest in other novel ordered 2D monolayers containing non-carbon elements.

2.1.2.4 Graphitic carbon nitride materials

Two-dimensional, carbon nitride materials are graphene analogous materials with unique physical and chemical properties. The five valance electrons $2s^2\ 2p^3$ of the N atom and its atomic size give it the ability to form strong covalent network structures with C atoms [76]. These structures are generally hard materials with superior chemical and thermal stability. Among experimentally realized, stable carbon nitride allotropes are, g-C_3N_4, g-C_3N_3 and C_2N two-dimensional networks. The appeal of using such materials as membranes is, in contrast to porous graphene, these structures may naturally have intrinsic pores patterned within the 2D network. The inherent pores of these materials offer uniformly distributed regular pore openings, for gas separation membranes.

Among the known carbon nitride 2D structures, the g-C_3N_4 is the most stable allotrope [76]. Its molecular structure is built from repeating triazine or tri-s-triazine units, as shown in Figure 2.4. This structure displays two characteristic X-ray diffraction peaks, with a strong peak at 27.21° (d=3.26 Å) and at 13.02° (d=6.82 Å), representing inter-planar stacking and in-planar stacking, respectively [77]. The aromatic C_3N_3 ring in the forms a π-conjugated graphene-like planar polymer giving it higher thermal stability up to 600°C and chemical resistance [78]. The g-C_3N_4

structure synthesis can be achieved by top-down approaches such as liquid exfoliation under sonication and thermal exfoliation with intercalation compounds [76]. In bottom-up synthesis methods, C_3N_3 triazene is used as the building block for molecular assembly.

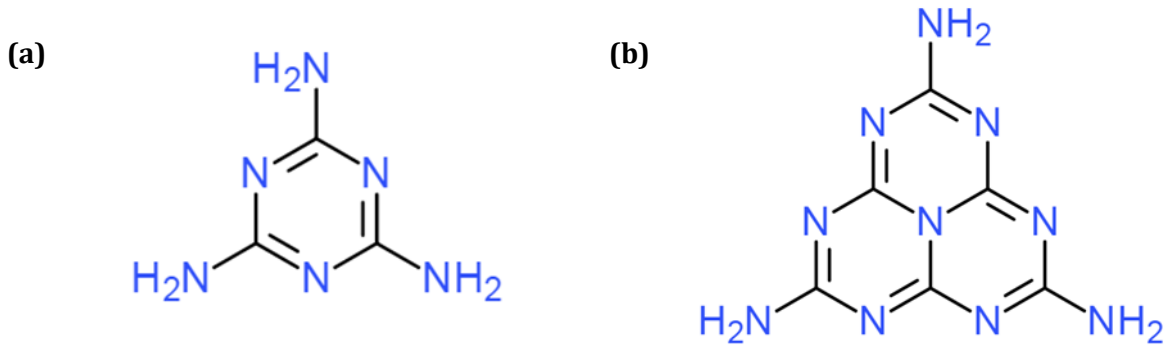

Figure 2.4: The g-C_3N_4 building blocks: (a) s-triazene and (b) tri-s-triazene units

A g-C_3N_4 monolayer, built from repeating tri-s-triazene units, will ideally form an atomically thin graphene-like structure with a geometric diameter of 3.11Å [79]. While the use as a catalysis in water splitting and photo-catalysis [76-78, 80-82] are the most commonly researched applications, several studies have reported the use of g-C_3N_4 in membrane applications [28, 79].

Despite being the most stable carbon nitride allotrope, g-C_3N_4 is not the only member of 2D-CN materials. Recently, a porous C_2N structure has been successfully synthesized by a bottom-up, wet chemical reaction [83]. This structure was synthesized by reacting hexaaminobenzene (HAB) trihydrochloride and hexaketocyclohexane (HKH) octahydrate in N-methyl-2-pyrrolidone (NMP) in the presence of sulphuric acid.

The XRD results and TEM images of C_2N show an interlayer distance of 0.328nm and 0.327 respectively, making it the thinnest layered 2D structure to date [83]. The C_2N 2D structure has a point to point distance (between the atom nuclei) in the pore opening of 5.45Å with a geometrical pore size of 3.07Å [84] implying possible application in membrane separation.

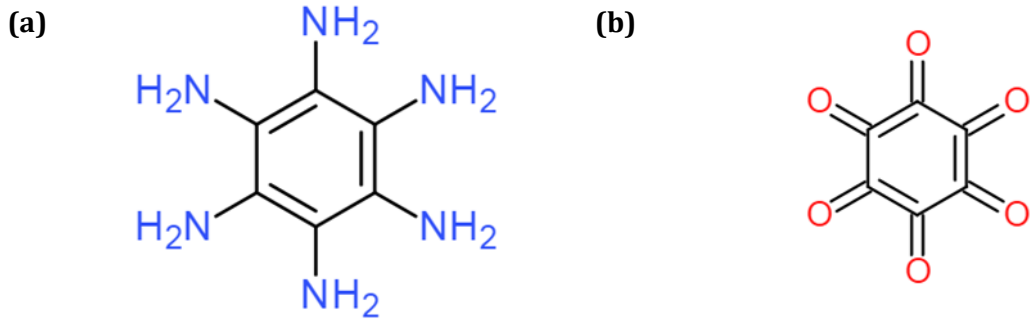

Figure 2.5: The building blocks of C_2N, (a) HAB and (b) HKH.

First-principles simulations have predicted that the C_2N-2D monolayer is capable of light isotope separation for small gas molecules: helium and hydrogen through quantum sieving [85]. This study further explores the behaviour of this structure, under strain, and predicts that the structure has remarkable stability, under strain values up to 10%. Their calculations of vibration frequencies of a supercell under 10% strain show that there are no imaginary frequency modes, confirming its remarkable stability when subjected to strain forces.

First-principles computations have explored the possibility of the existence of numerous other carbon nitride materials. Figure 2.6 shows g-C_3N_3, which is an example of a material predicted using first-principles simulations [29]. Ma et al., use first-principles simulations to predict the material's ability to act as a hydrogen purification membrane from carbon monoxide, nitrogen and methane [29]. Similarly a triazine based monolayer, CTF-0 (Covalent Triazene Framework was studied in use for helium separation and hydrogen purification [86].

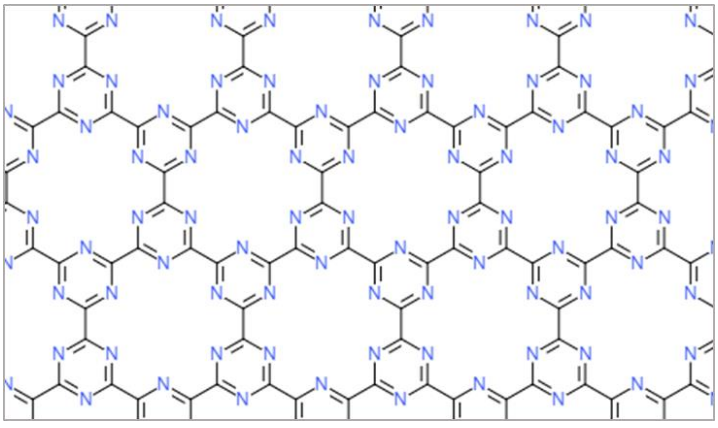

Figure 2.6: Predicted g-C_3N_3 structure

2.1.2.5 Boron Nitride Structures

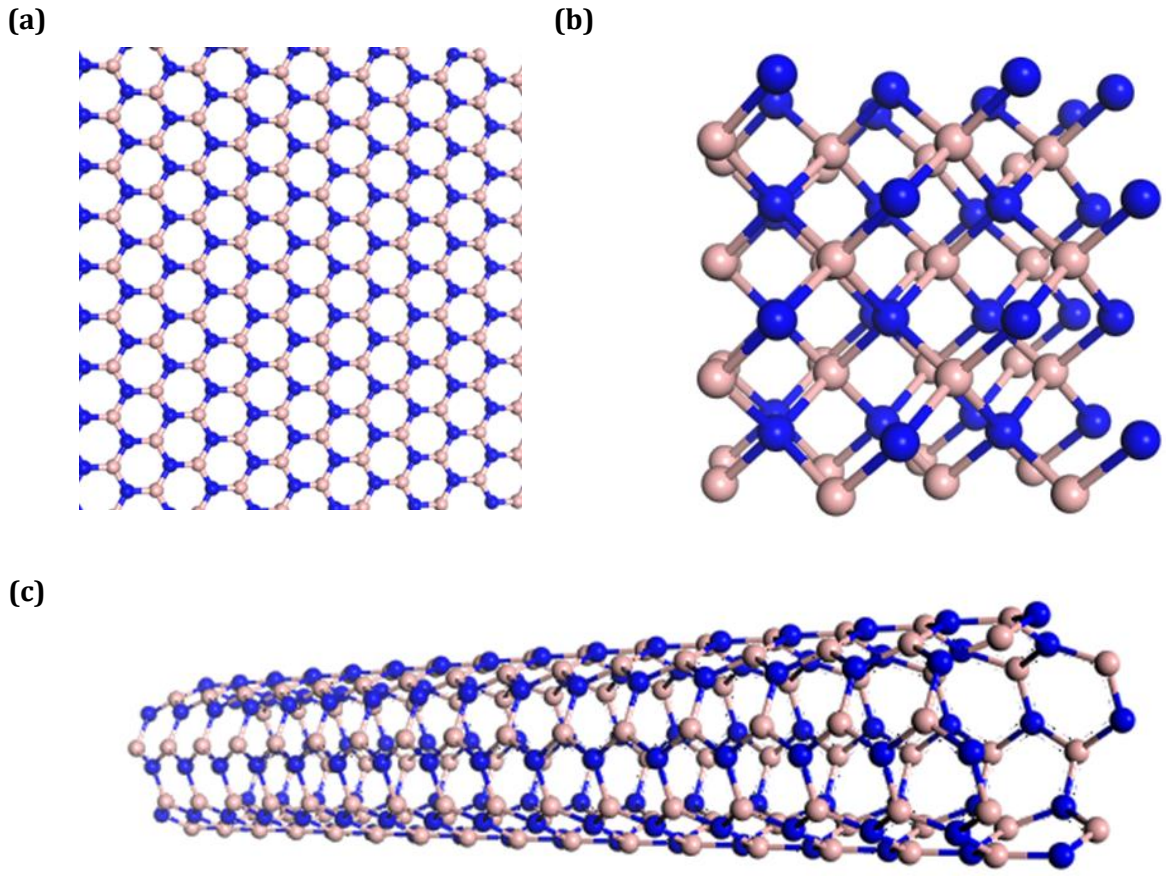

Figure 2.7: Carbon analogues boron nitride nanostructures: (a) h-BN, (b), c-BN and (c) BNNT. Atom colour code: blue, nitrogen; pink, boron.

Boron nitride nanomaterials constitute another class of allotropes with alternately linked boron and nitrogen atoms. In the periodic table, these two elements are the two immediate neighbouring elements to carbon, and have comparable atomic radii to the carbon. The combination of boron and nitrogen has an identical number of electrons in the outer-shell as carbon. Therefore, the BN crystal structures display numerous similar properties to carbon. Like carbon allotropes, they have excellent mechanical, chemical and thermal properties [87-90]. Examples of the number of boron nitride allotropes that exist are, cubic boron nitride (c-BN), which has a crystalline structure similar to diamond; hexagonal boron nitride (h-BN) in AB stacking, similar to graphite; and rhombohedral boron nitride (r-BN) in ABC stacking equivalent to r-graphite. Among these, h-BN is the most studied structure. Due to its structural similarity to graphene, especially being an atomically thin planar structure, h-BN is a suitable candidate to be

used in nano-porous molecular separation applications. The nano-pores can be created in the same manner as with in graphene.

Recently, Liu et.al. reported the synthesis of solid-state nanopores on a few-layers of a BN membrane [91]. Furthermore, Zhou et.al. successfully drilled nanopores in an atomic thin h-BN membrane with a highly focused electron beam [92]. They later reported that, by reducing the electron beam density to sub 200-pA/cm^2 and the drilling time duration to less than a second in a TEM, the pore size can be controlled to be less than 1nm [93]. Currently, most of the research on applications of porous h-BN is focussed on DNA translocation [91-94] while Zhang et.al. reported the use of designed porous BN membranes for H_2 purification from methane [95].

2.1.3 Strain tuning

Recently, applying mild strains on nanomaterials to tune their properties have gained the interest of the research world. Most of these studies are focused on using strain engineering to control electronic properties of nanomaterials [96-101]. The strain can be applied directly on the substrate to induce deformation of the substrate and accordingly, stretching of the membrane. Gerd, et.al. proposed a novel technique of manipulating the mismatch in thermal expansion between the substrate (PDMS) and the monolayer (MoS_2) to induce biaxial strain on membranes [101].

2.2 ADSORPTION SEPARATION

Nanoporous materials are a superior alternative to conventional adsorbent/absorbent materials, due to high surface areas; and the ability to create tuneable, active sites that can target a specific gas species. Among different types of nanomaterials, which exhibit good adsorption properties, metal organic frameworks (MOFs), zeolites and carbon nanotubes are popular materials used in many gas separation applications.

Among the gas separation applications focussed in this study, CO_2 separation is the most suited application for adsorption separation due to the polarity of the CO_2 gas. The polarity of CO_2 means, it may have a higher affinity to preferentially adsorb onto tuned active sites. In this thesis, gas

adsorption focusses on CO_2 separation. As mentioned earlier, post-combustion carbon capture is the most economical due to higher concentrations of CO_2, as opposed to direct air capture. This process involves removal of carbon dioxide from the exhaust gas of a power plant where the gas molecules adsorb on the surface of the adsorbent. The adsorbed CO_2 is then removed from the sorbent in a desorption step. The most common methods are TSA- Temperature Swing Adsorption (by applying thermal energy), PSA-Pressure Swing Adsorption (altering the pressure of the system) or by a hybrid method to separate physisorbed (van der Waal bonded) and/or chemisorbed (covalent bonded) gas molecules from the adsorbent [102].

This process requires materials with high adsorption capacity, high selectivity over other components of the flue gas (mainly N_2 which is ~ 70-80% of flue gas), and high diffusivity for CO_2 at pressures relevant to the partial pressure of CO_2 in the flue gas (~0.05-0.15 bar) and temperatures in the range of 40-120℃ . Moreover, the adsorbent material should possess

- Good thermal stability to withstand heat generated during the exothermic adsorption process and/or applied during the desorption process
- Good hydrothermal resistance to the water vapour in the flue gas
- High chemical and mechanical stability to withstand many cycles of operation
- High thermal conductivity to dissipate internally generated heat

Among the commonly used adsorbent materials, MOFs and the zeolites are the most popular. Out of MOFs used for CO_2 adsorption, the metal organic framework Mg-DOBDC showed the highest CO_2 uptake of 8mol/kg at ambient conditions [103]. Yet, MOFs suffer from low thermal and physiochemical stability. Zeolites are the most common material for CO_2 capture reported in the literature, but are effective only at elevated pressures, and their adsorption capacity is severely reduced by the presence of water[102, 104].

Synthetic carbon allotropes: fullerenes, Carbon nanotubes (CNTs) and graphene, despite being some of the most researched materials in the scientific community in recent years, have limited

research in CO_2 adsorption applications. However, their chemical and mechanical structures suggest that this class of materials is suitable for applications in conditions relevant to post-combustion CO_2 capture. CNTs are the most studied out of this class of materials for CO_2 capture.

2.2.1 Charge controlled CO_2 adsorption

Sun et al. [105] for the first time predicted enhanced CO_2 adsorption on $1e^-$ and $2e^-$ charged boron nitride sheets and nanotubes which show very little chemical affinity towards CO_2 in its neutral state. Also Sun et al. [31] showed that chemical interactions between boron carbon nanotubes (B_2CNT) and CO_2 can be enhanced by introducing extra electrons to the system. The charge densities associated with both studies were in order of 10^{13} cm^2, which were claimed to be easily achievable by electrochemical method, electrospray, electron beams or gate voltage control [105].

2.2.2 Fullerenes doped with a single B atom

Heterofullerenes are fullerene structures where one or more cage C atom/s is/are substituted by impurity atom/s [106]. In addition to the properties inherent to carbon based nanomaterials, heterofullerenes also offer excellent tuneable chemical and physical properties [107]. Gas adsorption on heterofullerenes is an appealing subject. Gao et al. [108] studied CO_2 adsorption on calcium decorated C_{60} fullerene and Gao, F et al. [109] studied O_2 adsorption on nitrogen doped fullerene. Since the binding energy of a decorated atom and the gas adsorption energy can lie within the same range, a substituted heterofullerene may be more suitable than decorated fullerenes.

Boron doped C_{60} fullerenes are one of the most structurally stable heterofullerenes [106]. Guo et al. synthesized B doped C_{60} fullerene for the first time, in microscopic amounts by laser vaporisation where one or more C atoms in the fullerene cage is substituted by one or more B atoms [110]. Zou et al. [111] demonstrated synthesis of B doped C_{60} fullerene by radio frequency plasma assisted vapour deposition technique. Recently Dunk et al. [112] introduced a method to produce BC_{59} directly from exposing boron vapour to C_{60} fullerene. Wang, S et al. [113] stated that substituting a single C atom of the C_{60} fullerene with a B on atom does not cause a significant

distortion to the cage structure. The net change in the dihedral angle caused by the 'puckering' induced due to doping is only 1.6%. Kurita, K et al. [114] predicted that due to the similarity between the C-B bond and C-C bonds, the changes in the bond lengths are less than 5%. Therefore, the BC_{59} fullerene has a similar structural and thermal stability as the C_{60} fullerene structure. They estimated the binding energy of a single B atom doping to be 6.03ev/atom [114].

2.3 SUMMARY AND RESEARCH GAPS

Based on the literature review, the following conclusions can be drawn:

- Porous graphene of atomic thickness shows potential to be an ideal membrane material. A number of studies have been carried out on gas separation by nanoporous graphene with different pore openings and pore sizes.
- Fuelled by the discovery and versatility of graphene, there is immense interest in other graphene-like other 2-D mono-layered materials and other low dimensional carbon materials.
- Nano membranes can be designed by two approaches. Creating pores on a pristine layer of graphene or other similar planar layers will give more control over pore size, shape and distribution. Conversely, layered materials with uniformly distributed, regular inherent pores, offer better control of the membrane's selectivity.
- Graphitic carbon nitride is a class of material, which shows strong mechanical and useful chemical properties. Various graphitic carbon nitride allotropes have been reported and C_3N_4 and C_2N have been successfully synthesized.
- Limited studies exist of the gas separation capabilities of these carbon nitride materials exist
- Hexagonal boron nitride is a graphene-like material, which shows similar promise, and porous h-BN has been synthesized with sub nanometre pores.

- Membrane separation in nano membranes can be achieved through size sieving, chemical affinity and quantum sieving (isotope separation), and depending on the type of separation mechanism/s it is interesting to observe how a membrane can be chemically and/or mechanically tuned to achieve the desired separation.
- Strain engineering of nanomaterials has been successfully used to tune electronic properties of 2D nanomaterials.
- Fullerenes can be doped with foreign atoms and B doped fullerenes are proven to have excellent structural stability.
- Modifying the charge state of nanomaterials, including BC systems have the ability to enhance the interactions between CO_2 and the material causing the CO_2 adsorbance on the material surface.
- The BC_{59}^{-1} is structurally stable.

The key points of our literature review and the identified research gaps are summarized as below.

- Despite being synthesized more than two decades ago and the inherent structural and chemical stability, studies on the use of heterofullerenes are very limited. To the best knowledge of the author, there are no studies on the use of B doped fullerenes for gas separation applications.
- Graphitic C_3N_4 that is the most stable carbon nitride nano-material has limited studies on gas separation and there is no study on the effects of mechanical tuning on gas separation capabilities or efficiency.
- To the best knowledge of the author, no studies exist for H_2 purification or carbon capture using g-C_2N despite being a structurally stable and experimentally synthesisable nano-material.
- Despite the structural similarities with graphene, limited studies exist on gas separation using porous h-BN membranes. To the best knowledge of the author, there is no available

literature for studies on the use of h-BN porous structure variants investigated in this thesis or the effects of mechanical tuning in the gas separation performance.

- Overall, charge and mechanical tuning are novel tuning methods and only limited literature exists on using such approaches to manipulate gas separation performance and efficiency.

From these observations, in this research computational chemistry will be used to investigate H_2, CO_2, N_2 and CH_4 separation capabilities of low dimensional carbon materials and other graphene-like 2 dimensional, atomic-scale materials through adsorption or membrane separation or a combination of both. Furthermore, novel approaches of tuning the nano materials to alter and/or improve their separation behaviour through charge, chemical structure and mechanical tuning will be explored.

CHAPTER 3 METHODOLOGY

In this chapter, the different simulation tools/approaches of computational chemistry are first introduced and next, *ab initio* quantum computational methods and molecular dynamics simulations methods are reviewed in detail. The latter two methods are the principal methods employed to accomplish the objectives of this work. The detailed simulation settings are presented in each chapter along with the respective work.

A number of theoretical approaches have been developed to study the diffusion of gas species through a nano-porous membrane. The two most common approaches are briefly introduced below [25].

- **Genuine kinetic separation**- this method can provide diffusion rates of various species on a short time-scale [51]. This approach employs MD simulations defined by calculation of internal forces. It is the most extensively used method in membrane gas separation applications due to the ability to handle larger systems and the ability to provide numerical estimates for gas flux [18, 20, 67, 68, 115-117]. However, it suffers from limitations in modelling isotope-separation due to the identical molecular charges, shape and chemical characteristics between isotopes, and the differences in isotopes is often not well represented at this scale.

- **Statistical kinetic separation: quantum description**- this method unlike the former method, does not simulate the gas diffusion dynamics in a time scale, but stochastically simulates the kinetic separation behaviour by focussing on bottleneck positions along the potential energy surface based on Transition State Theory (TST) [51]. The most commonly used method is the use of DFT calculations to obtain the Minimum Energy Pathway (MEP) for each species to cross through the membrane pore from one side to the opposite side. The popular methods to study the MEP involve the of use transition state algorithms such as Linear/ Quadratic Synchronous Transit (LST/QST) methods inherently implemented within DFT software to search for a local maximum point in the

pathway. While this method can more accurately capture interatomic interactions between the gas species and membrane compared to MD simulations, it can only evaluate an ideal setting of minimum energy pathway and does not take factors such as system pressure and effects of other interactions present within a system, in to account.

Similarly, to study gas adsorption, several theoretical approaches exist including quantum mechanical approaches, statistical mechanics and theoretical models based on continuum theory. Due to the ability to simulate, chemical interactions with bond breaking/formation and electron exchange, especially visible in chemisorption, quantum techniques are the most commonly used approaches to study nano-adsorbents [118-121]. The quantum techniques used are Configuration Interaction (CI) theory or total energy *ab initio* calculations [122], while statistical mechanical techniques are commonly used in collective gas adsorption studies [122]. Metropolis Monte Carlo algorithms within the grand canonical statistical ensemble are the most commonly used statistical mechanical approaches to study gas adsorption on nano-adsorbents.

While each approach has their own strengths and limitations, in our adsorption simulations we used *ab initio* quantum mechanical simulations, which can accurately describe chemical interactions and the charge state of individual atoms, to establish the selectivity of an adsorbent towards a certain gas species over the rest of the species. Despite the inability to yield macroscopic parameters such as adsorption capacity, it gives an accurate criterion for screening materials to be used as adsorbents, and gives in-depth explanation of the selective adsorption behaviour. This knowledge is more beneficial in tweaking the adsorbent to suit the specific application and the knowledge obtained in molecular level interaction can be used in future material design as well. For membrane gas separation, MD simulations are primarily used due to their ability to give a quantitative analysis along with a qualitative analysis to a certain extent. First-principles DFT calculations are used when permissible by the scale of the molecular system to deepen the qualitative assessment. A theoretical introduction to the simulation methods used in this thesis is given in the following sections.

In computational chemistry, chemical structures and reactions are simulated mathematically, with the full or partial use of fundamental laws of physics. This offers the ability to examine chemical phenomena based on simulations performed on computers rather than experiments conducted in the laboratory. The field of computational chemistry has tremendously benefited from the exponential growth of high computing power, due to the improvements in computer hardware and software. Computational chemistry can be loosely categorized into two main groups as molecular mechanics and electronic structure theory [123]. The continuum methods include tools such as finite element method, meshless methods and mesoscale methods that are used for bulk scale simulations.

3.1 QUANTUM MECHANICS

The electronic structure methods use the laws of quantum mechanics, which states that the energy state and other interrelated properties of a molecule are obtained through solving the time independent Schrödinger equation.

$$\mathbf{H}\Psi = \mathbf{E}\Psi \qquad \text{Equation 3.1}$$

The Hamiltonian *H*, is the operator associated with the energy (kinetic and potential energies) of a physical system. In quantum mechanics, the wave function theory (WFT) describes the quantum state of a system, based on the many-electron wave function $\Psi(r_n)$. The solution of the Schrödinger equation gives the wave function and the energy of the system, where the wave function producing the lowest energy describes the system in its ground state.

These quantum mechanical expressions give a mathematical description of the electrons' behaviour. However except for the hydrogen atom, which is the smallest system, an exact solution for these equations have never been solved for any chemical system [124]. Therefore, the solving of the quantum mechanical equations and consequently the entire computational chemistry is built on mathematical approximations. The two classes of electronic structure methods are the semi-empirical methods and *ab initio* methods.

3.1.1 Semi-Empirical Methods

In semi-empirical calculations, experimentally derived parameters are used to simplify the equation solving and hence are much faster than *ab initio* methods. However, the accuracy of the solution by semi-empirical methods is limited by how closely the molecules being computed are represented by the molecules in the database used in parameterization. This method includes various methods such as AM1, PM3, INDO, CNDO etc. [125-129].

3.1.2 Ab initio Methods

Ab initio methods are purely based on quantum mechanics hence giving the name *ab initio* meaning first-principles. This method solves the Schrödinger equation using a series of rigorous mathematical approximations. In contrast to semi-empirical methods, *ab initio* calculations provide highly accurate results and are not limited by the class of parameters or the accuracy of experimentally derived parameters.

3.1.3 The Density Functional Theory

The density functional method is a combination of both the qualitative and quantitative models used in semi-empirical and *ab initio* methods. While the density functional theory (DFT) is essentially a variation of the wave function theory, the main distinction is, it uses the electron density distribution instead of the electron wave function used in the WFT. DFT methods are attractive as they are able to increase the computational accuracy significantly, without demanding more computational resources. On the other hand, the WFT methods while not generally as demanding as DFT methods for simpler systems, require exponential increase to computational resources for minor accuracy improvements.

DFT theory is based on a theorem developed by Hohenberg and Kohn [130] and further generalized by Levy [131]. It states that the ground-state properties of a system are functionals of the charge density ρ.

Based on DFT the total energy can be expressed as in Equation 3.2.

$$E[\rho] = T[\rho] + U[\rho] + E_{XC}[\rho] \qquad \text{Equation 3.2}$$

Where $E[\rho]$ - total energy of the system

$T[\rho]$ - the kinetic energy of a system of non-interacting particles of density ρ

$U[\rho]$ - the classical electrostatic energy due to Coulombic interactions

$E_{XC}[\rho]$ - all the many-body contributions to the total energy from exchange and correlation energies

From the wave functions and the charge density, the kinetic energy and electrostatic energy terms can be expressed as shown in Equation 3.3 and Equation 3.4 respectively.

$$T = \langle \sum_{i}^{n} \emptyset_i \left| \frac{-\nabla^2}{2} \right| \emptyset_i \rangle \qquad \text{Equation 3.3}$$

$$U = \int V_N(\boldsymbol{r})\rho(\boldsymbol{r})dr + \frac{1}{2}\int \frac{\rho(\boldsymbol{r}_1)\rho(\boldsymbol{r}_2)}{|\boldsymbol{r}_1 - \boldsymbol{r}_2|} d\boldsymbol{r}_1 d\boldsymbol{r}_2 + V_{NN} \qquad \text{Equation 3.4}$$

Where for Equation 3.4, the first term represents the electron-nucleus attraction; the second term is a representation of the electron-electron repulsion and the final term is the nucleus-nucleus repulsion.

To derive the final term in Equation 3.2, the exchange correlation energy, certain approximations are required to make the DFT method computationally possible. There are various methods to obtain these approximations. Below is a summary of the various approaches available to obtain the approximations in order of increasing accuracy.

3.1.3.1 The Local Density Approximation (LDA)

This method only employs the local densities in the exchange-correlation energy description. In this method, the local approximation of the local exchange correlation energy is derived from the homogeneous electron gas (HEG) model. This method does well in predicting the molecular properties based on relative energy differences in a given density. However it tends to overestimate molecular properties based on absolute energy differences between densities such

as bond energies, making this method more useful in in molecular structural analysis rather than in thermochemical studies [132]. Examples for several functionals of LDA methods based on parameterization are;

- VWN (Vosko-Wilk-Nusair [133])
- PW92 (Perdew-Wang [134])

3.1.3.2 The Generalized Gradient Approximation

In this method, the local density gradients are added to the exchange correlation. Unlike in LDA, which assumes the density is uniform, and hence over-estimates the exchange correlation energy, the GGA method with gradient corrections gives more quantitatively accurate estimates of the bond energies and other quantitative molecular properties. Examples for commonly used GGA functionals are:

- PBE (Perdew - Burke – Ernzerhof) [135]
- BLYP (Becke-Lee-Yang-Parr) [136, 137] [137]

3.1.3.3 Meta-Functionals

In this third type of functionals, the kinetic energy density is added to the expression of the density functionals. This method offers increased accuracy and at the same time demands more computational resources and time.

3.1.3.4 Hybrid functionals

This is the fourth class of approximations to the exchange-correlation energy. This contains portions of exact exchange from the Hartree-Fock theory with gradient corrections for correlation and gradient corrections for exchange from other *ab initio* or empirical sources. The most commonly used hybrid functional method is the B3LYP (Becke- 3 parameter- Lee – Yang-Parr method) [137-139].

3.1.4 Basis-sets

The basis set in quantum mechanical simulations mathematically represents the molecular orbitals within the molecule. This effectively simplifies the electron representation by confining each electron to a given region within space [123]. In theory, an electron has a finite probability of existing anywhere in space. Therefore, the more a basis set restricts an electron to a confined space, the less accurate its representation is for a fixed basis set. Therefore, a larger basis set gives a more accurate approximation of the system. However, working with larger basis sets demands higher computational resources. Therefore, the choice of basis set should be a balance between accuracy and computational time. A summary of different basis sets is given below.

Minimal basis set - This basis set has the minimum number of basis functions needed for an atom. It uses one atomic orbital for each orbital that is occupied in the free atom. An example for Gaussian basis set is STO-3G and the DMol3 equivalent is 'min'.

Example: C- 1s, 2s, $2p_x$, $2p_y$, $2p_z$

Split valance basis sets - As the name implies these basis sets allow having two or more sizes for the basis function, but restricts the ability to change shape. Examples for Gaussian double split basis set is 6-31G and the DMol3 equivalent is 'DN'.

Example: C- 1s, 2s, 2s', $2p_x$, $2p_y$, $2p_z$, $2p_x$', $2p_y$', $2p_z$'

Polarized basis sets - This basis set allows orbital to change both size and shape, by adding 'f' auxiliary functions with angular momentum one higher than that of the highest occupied orbital in free atom. The polarized functions add 'd' function to carbon atoms and 'f' function to heavy metals. Examples for Gaussian basis set are 6-31G(d) and 6-311G(d,p) and the DMol3 equivalents are 'dnd' and

'tnp' respectively. The basis-sets 6-311G(d,p) and 'tnp' has triple split valance basis sets

Diffuse functions - These functions are much larger functionals of s and p functions, and thereby let orbitals to occupy a larger region in space. This is denoted by the '+' sign. Two signs as '++' denote that diffuse functions are also added to hydrogen and helium atoms. Examples are the Gaussian basis set, 6-31G (d)+ and the DMol3 equivalent, 'dnd+.

Plane-wave basis sets - In addition to the basis sets introduced above, which falls under the broad category of atomic orbital basis sets, a different class of basis sets named plane-wave basis sets exist. Unlike the atomic orbital basis sets, this type of basis sets is unbiased by the atomic positions. They are mainly used in three-dimensional periodic systems and offers smooth monotonic convergence of the wave function. This type of basis sets does not have the basis-set superposition error (BSSE) and have the ability to use Fast Fourier Transform efficiently. However, it generally requires pseudo-potentials and large number of basis functions.

In this thesis, for quantum mechanical calculations, the first-principles DFT simulations were carried out to study the intramolecular interactions and the stability of the chemical structures. DFT is a computational method that calculates the properties of the molecule under study, based on the determination of the electron density of the molecule. The most noteworthy advantage of DFT studies is the significant improvement of the results without the additional increase in the computational time. The atomic systems studied with quantum mechanical methods in this thesis are complex and their scale or size demands large computational resources. The genuinely accurate quantum chemistry *ab initio* methods such as MP2 and CCSD(T), which are

computationally quite expensive, are only efficient for small systems of few tens of atoms [140]. Another important advantage of the use of DFT simulations is, its negligible dependency [141] on the basis set superposition error (BSSE) [142], which strongly affects the binding energy results from MP2 methods [143].

For simulations with finite systems we used the B3LYP method which is commonly used to predict thermochemical data with superior accuracy [123]. Especially in adsorption studies, this method is known to give reasonably accurate results with modest demand for computational resources and time. Cazorla and Shevlin [140] studied the use of DFT calculations of carbon based materials for carbon capture. They evaluated CO_2 adsorption on several carbon-based systems using standard DFT (i.e. LDA and GGA), hybrid DFT (i.e. PBE0 and B3LYP), van der Waals DFT (vdW), and MP2 level of theories using results obtained by MP2 calculations as the benchmark and compared the results obtained by different DFT methods. They identified that the hybrid DFT results are in good agreement with MP2 results qualitatively and quantitatively, while the calculated adsorption values of DFT hybrid methods are always smaller than the results of the MP2 method.

For simulations with periodic systems, the generalized gradient approximation (GGA), treated by the Perdew-Burke-Ernzerhof (PBE) exchange correlation potential with long-range dispersion correction via Grimme's scheme, was used. This method gives simulation results with improved atomic and molecular total energies, superior cohesive energies of solids and more accurate transition state energies for chemical reactions. The choice of basis set for each simulation will depend on the systems being evaluated. The most used basis set in the completed calculations was the split valance polarized 6-31G(d) basis set. This basis set provides a good balance between computational efficiency and accuracy. It has two sizes of basis function for each valance orbital with 'd' functions added to heavy atoms. When larger basis sets are required, geometry optimization will be done using 6-31G(d) basis set and then the single point energy will be calculated with the intended larger basis set. We have identified that this does not affect the final

result significantly. A sample calculation was done to demonstrate this hypothesis for a system of B_2C_{58}. (Table 3.1)

Table 3.1: Comparison of basis sets for optimization and evaluation

	Computational method		Results (au)
	Geometry optimization	Single point energy	
(1)	B3LYP/6-31G(d)	B3LYP/6-31G(d)	-2259.62921976
(2)	B3LYP/6-31G(d)	B3LYP/6-311G(d,p)+	-2260.05912741
(3)	B3LYP/6-311G(d,p)+	B3LYP/6-311G(d,p)+	-2260.05912741

3.1.5 Software

In this section, the software used for Quantum Mechanics simulations in this study is briefly introduced. The detailed simulation procedures, settings and parameters are presented in chapters corresponding to each study.

3.1.5.1 DMol³

DMol³ [144, 145] is a software module which facilitates modelling of structure and energies of a range of molecular systems, including molecules, crystals, surfaces, solids and metallic solids. This software is used to predict structures and to optimize their geometries, calculate the energy of states, predict reaction energies and calculate thermodynamic properties. It offers high accurate computations, especially for periodic structures, without compromising the computational efficiency in this thesis, DMol³ is used to obtain optimized structures with and without lattice constraints; calculate the total energy of state; and transition state calculations and/or potential energy scan calculations to analyse the energetics of gas diffusion through membrane nanopores.

3.1.5.2 Gaussian

Gaussian [146] is a software that uses electronic structure modelling to predict structures, energies, thermodynamic properties, NMR and vibrational spectra of molecular systems. In this thesis, Gaussian and GaussView [147] (the associated GUI software) software were used for

structure building, geometry optimizations, thermodynamic analysis, IRC (Intrinsic Reaction Coordinates) calculations, and TS optimization calculations.

3.2 MOLECULAR MECHANICS

The molecular mechanics simulations are based on laws of classical physics to model the molecular structures and their properties. In molecular mechanics simulations, each method is characterized by the type of force field. For such calculations, the electrons in the system are explicitly defined. The computations are based on the nuclei interactions, and the electronic effects are implicitly added through force field parameterization.

The generalization in molecular mechanics simulations significantly reduces the demand for computational resources and time, thus making it an appropriate choice for large systems containing few thousands of atoms. On the other hand, the drawbacks of this method are the inability to model situations where electronic effects are central, because the electrons are not explicitly defined and the limitations of force field types in parameterization of different classes of molecules.

3.2.1 Molecular Dynamics Simulations

Molecular dynamics simulate the time-dependent behaviour of a molecular system using Newtonian physics. This simplification compared to quantum molecular simulations allows exploring large system and longer time durations.

This kind of simulations, are found in numerous research areas of computational chemistry and physics. MD simulations approximately can be sub divided into three categories. Namely, *ab initio* MD where first-principles calculations are used to derive atomic forces; classical MD, which uses analytical empirical interaction potentials; and coarse grain MD, where the empirical potential of a representative bead, formed from a cluster of atoms is used [148]. The choice between the different kinds of MD simulations methods to use depends on the level of detail of the model physical system. Naturally, the *ab initio* MD method is the most detailed and hence the most accurate representation of a system, where the electrons of the atoms in the model are modelled

unambiguously, making this technique more suitable for simulations of electron transport and chemical reactions. In classical MD technique, only the nuclear interactions of the particles within the system are modelled, reducing the accuracy compared to *ab initio* MD simulations. This method, where each electron is not explicitly represented, is more appropriate for analysing mechanical behaviour, transport properties and some level of chemical interaction. In coarse-grain MD simulations, a single particle is used to represent a group of atoms, and hence it has the least amount of detail and is better suited for analysis of structural and mechanical properties of large sized systems.

Unsurprisingly, with the increased level of detail within a system, the computational requirements increase limiting the *ab initio* MD simulations to small systems of hundreds of atoms to picoseconds of time scale. Conversely, the less detail of classical MD simulations, allows calculations of considerably larger sized systems (of 10^6 atoms) for time periods of microseconds and coarse-grain MD can model larger systems in micro scale up to few seconds [148].

3.2.2 Molecular Dynamics Simulations Theory

In MD simulations, the atomic trajectories, characterized by position, velocity and acceleration are governed by classical mechanics as shown in Equation 3.5. The sequential trajectories are generated by solving this equation with appropriate interatomic potentials and suitable initial and boundary conditions. Where $F_i, E(r_i)$, m_i *and* r_i denote the force, potential energy, mass and the position of the i^{th} atom of the system respectively.

$$F_i = m_i \frac{\partial^2 r_i}{\partial t^2} = -\frac{dE(r_i)}{dr_i} \qquad \text{Equation 3.5}$$

3.2.2.1 Force Fields

A force field is used to characterize molecules and their behaviour using the following components [123].

- A set of equations describing the variation of molecular potential energy with the position of its atoms
- A set of parameters that fit the above equations to synchronize the modelled atomic behaviour with experimental data, which use force constants to relate the energy components and structural data such as bond lengths and angles.
- Varied atom types defining their characteristics even within a single type of element. For example, a carbon atom in a carbonyl group is characterized differently than a carbon atom in a methane molecule. The variation of atom type within the same element depends on its hybridization, charge state and the type of the other atom/s it is bonded with.

In classical MD simulations, atomic potential function (U) is computed from force fields with predetermined parameters. The empirical force fields include bond stretch, angle bend and dihedral torsional interactions, which describe the bonded interactions, and van der Waals and Coulombic interactions that are non-bonded interactions.

$$E(r) = E_{bond} + E_{angle} + E_{dihedral} + E_{vdW} + E_{coulombic} \qquad \text{Equation 3.6}$$

3.2.2.2 Bonded Interactions

The bond stretching and angle bending are most commonly modelled by a harmonic function as shown in Equation 3.7 and Equation 3.8, but they are not limited to this function.

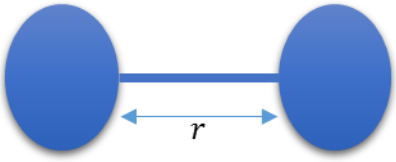

$$E_{bond} = \sum_{bonds} k_b(r - r_{eq})^2 \qquad \text{Equation 3.7}$$

Where k_b is the bond constant, which is a measure of the bond stiffness (stiffer the bond, higher the resistant for stretching) and r_{eq} is the bond length at equilibrium.

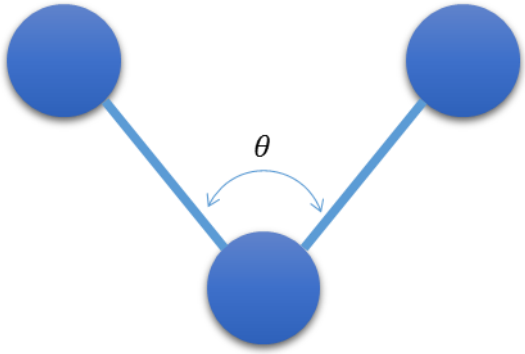

$$E_{angle} = \sum_{angles} k_\theta (\theta - \theta_{eq})^2$$ Equation 3.8

Where, k_θ is the angle constant and θ_{eq} is the bond angle at equilibrium.

The torsional interaction is the dihedral angle formed by the two planes of a system with four linearly connected atoms. One of the most commonly used functions to represent the dihedral potential is the CHARMM force field's expression for dihedral potential as shown in Equation 3.9.

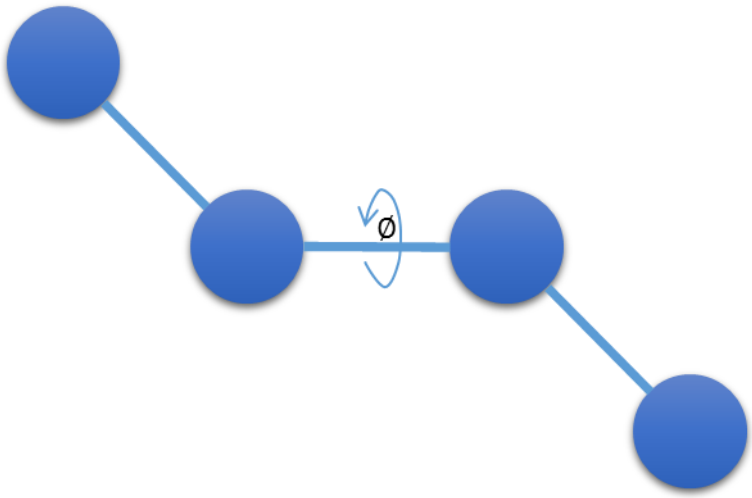

$$E_{dihedral} = \sum_{dihedral} k_\emptyset [1 + cons(n\emptyset - d)]$$ Equation 3.9

Where, $k_\emptyset$ is the dihedral force constant, n the multiplicity of the dihedral angle (a positive integer) and d the integer value of degrees.

3.2.2.3 Non-bonded interactions

In classical MD simulations, non-bonded interactions contain two parts: van der Waals interactions and electrostatic interactions. The most popular form of representing the van der Waals interactions is the Lennard-Jones 12-6 function shown in Equation 3.10 [149].

$$E_{LJ} = \sum_{i<j} 4\varepsilon_{ij}\left[\left(\frac{\sigma_{ij}}{r_{ij}}\right)^{12} - \left(\frac{\sigma_{ij}}{r_{ij}}\right)^{6}\right] \qquad \text{Equation 3.10}$$

In the Lennard-Jones equation, σ is the distance at which the inter-particle potential is zero, which is a representation of the size of the atom, and ε is the depth of the potential wall, which represents the energy of interatomic vdW attraction. The Lennard-Jones potential is truncated at a cut-off distance, which is the distance at the point beyond where the interatomic vdW interactions between two particles become negligible.

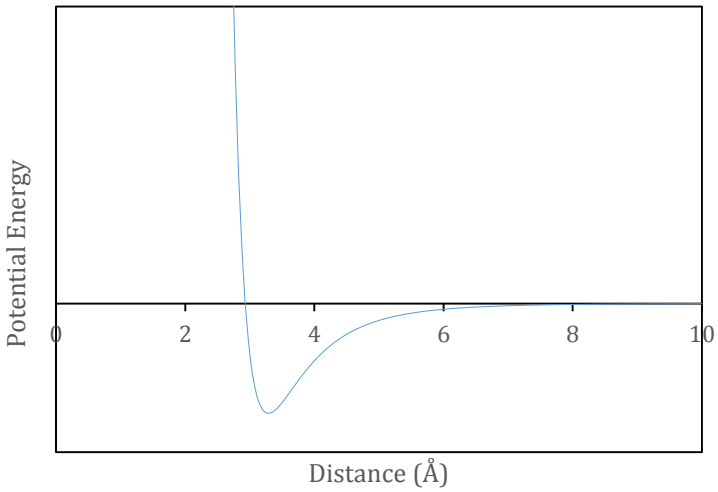

Figure 3.1: The Lennard-Jones potential

When a system contains multiple particles, and inter-particle data ε_{ij} and σ_{ij} are not available, a suitable mixing rule is used to approximate these terms, using pure body terms. The choice of mixing rule usually depends on the kind of the force field. Examples of the most commonly used mixing rules are given below.

Geometric mixing rule:

$$\sigma_{ij} = \sqrt{\sigma_{ii} \times \sigma_{jj}} \quad \text{and} \quad \varepsilon_{ij} = \sqrt{\varepsilon_{ii} \times \varepsilon_{jj}} \qquad \text{Equation 3.11}$$

Arithmetic or Lorentz-Berthelot mixing rule:

$$\sigma_{ij} = \frac{1}{2}\left(\sigma_{ii} + \sigma_{jj}\right) \quad \text{and} \quad \varepsilon_{ij} = \sqrt{\varepsilon_{ii} \times \varepsilon_{jj}} \qquad \text{Equation 3.12}$$

The Coulomb's law is used to determine the interatomic interaction caused by the electro-negativity of each atom.

$$E_{Coulombic} = \sum_{i<j} \frac{q_i q_j}{4\pi\varepsilon_0 r_{ij}} \qquad \text{Equation 3.13}$$

Where, q_i denotes the fixed partial charge on the ith atom, and ε_0 is the dielectric constant. Unlike the Lennard-Jones potential, the Coulomb potential does not decay over a short distance. Therefore, to reduce the computational cost of long-range electrostatic interactions, different approaches are used for the computation. The most popular methods are the Ewald summation method and the particle-particle-particle mesh (PPPM) method, which use fast Fourier transformation algorithms.

3.2.3 Algorithms

In classical MD simulations, the force on a single particle is affected whenever the particle or another particle with which it has interatomic interactions, changes position due to the intermolecular interactions. Since the forces on each particle rely on each other, an analytical solution becomes impossible, necessitating integration using a finite element method. Various algorithms have been developed to integrate the Newton's equation, such as the Leap Frog Algorithm [150], Gear Algorithm [151] and Verlet Algorithm [152], where the latter is probably the most commonly used method in classical MD simulations [153]. These algorithms are based on the assumption that Taylor series expansions can approximate atomic positions and dynamic properties [154].

$$\boldsymbol{r}(t+\delta t) = \boldsymbol{r}(t) + \delta t\boldsymbol{v}(t) + \frac{1}{2}\delta t^2\boldsymbol{a}(t) + \frac{1}{6}\delta t^3\boldsymbol{b}(t) + \frac{1}{24}\delta t^4\boldsymbol{c}(t) + \ldots\ldots\ldots\ldots \qquad \text{Equation 3.14}$$

$$\boldsymbol{v}(t+\delta t)=\boldsymbol{v}(t)+\delta t\boldsymbol{a}(t)+\frac{1}{2}\delta t^2\boldsymbol{b}(t)+\frac{1}{6}\delta t^3\boldsymbol{c}(t)+\ \ldots\ldots\ldots\ldots \quad \text{Equation 3.15}$$

$$\boldsymbol{a}(t+\delta t)=\boldsymbol{a}(t)+\delta t\boldsymbol{b}(t)+\frac{1}{2}\delta t^2\boldsymbol{c}(t)+\ \ldots\ldots\ldots\ldots \quad \text{Equation 3.16}$$

Where $\boldsymbol{r}$, $\boldsymbol{v}$, $\boldsymbol{a}$, $\boldsymbol{b}$ and $\boldsymbol{c}$ represent the position, velocity (the first derivative of the position vector with respect to time), acceleration (second derivative), third derivative and fourth derivatives, respectively.

3.2.3.1 Verlet Algorithm

In the Verlet algorithm, two Taylor series expansions of the position vector are combined where the positions vector $\boldsymbol{r}(t)$ and $\boldsymbol{r}(t-\delta t)$ are used to calculate the positions vector $\boldsymbol{r}(t+\delta t)$at time step $t+\delta t$.

$$\boldsymbol{r}(t+\delta t)=\boldsymbol{r}(t)+\delta t\boldsymbol{v}(t)+\frac{1}{2}\delta t^2\boldsymbol{a}(t)+\ \ldots\ldots\ldots\ldots \quad \text{Equation 3.17}$$

$$\boldsymbol{r}(t-\delta t)=\boldsymbol{r}(t)-\delta t\boldsymbol{v}(t)+\frac{1}{2}\delta t^2\boldsymbol{a}(t)-\ \ldots\ldots\ldots\ldots \quad \text{Equation 3.18}$$

Combining these two equations gives;

$$\boldsymbol{r}(t+\delta t)=2\boldsymbol{r}(t)-\boldsymbol{r}(t-\delta t)+\delta t^2\boldsymbol{a}(t) \quad \text{Equation 3.19}$$

The Verlet algorithm offers a straightforward and simple to implement approach to solve the Newton's equation of motion, with a truncation error in the order of δt^4. However, the addition of a small term $\delta t^2\boldsymbol{a}(t)$ to a much larger $2\boldsymbol{r}(t)$ and $\boldsymbol{r}(t-\delta t)$ may lead to loss of precision. Additionally, it requires the previous step's positions at $t=-\delta t$ to compute the positions for $t=\delta t$, which is usually obtained by truncating the Taylor series expansion as $\boldsymbol{r}(-\delta t)=\boldsymbol{r}(0)-\delta t\boldsymbol{v}(0)$. The other negative of this approach is that it does not explicitly include the velocity expression and therefore the velocity cannot be computed until the next time step. The velocity is especially important to calculate the kinetic energy of the system, to test the conservation of total energy, which is important to verify accurate progression of a MD simulation. In the Verlet

algorithm, the velocity can be calculated from the difference in the positions during the entire time step or during a half time step as in Equation 3.20 and Equation 3.21 respectively.

$$\boldsymbol{v}(t) = \frac{\boldsymbol{r}(t+\delta t) - \boldsymbol{r}(t-\delta t)}{2\delta t} \qquad \text{Equation 3.20}$$

$$\boldsymbol{v}\left(t+\frac{1}{2}\delta t\right) = \frac{\boldsymbol{r}(t+\delta t) - \boldsymbol{r}(t)}{\delta t} \qquad \text{Equation 3.21}$$

3.2.3.2 Leap-Frog Algorithm

To overcome the issues a half-step algorithm was developed by Hockney [155], which is known as the 'Leap-frog' algorithm. This algorithm is based on the Verlet algorithm, but explicitly includes the velocity term and avoids the $\delta t^2 \boldsymbol{a}(t)$ term reducing the precision errors. The 'leap-frog' algorithm uses Equation 3.22 and Equation 3.23 to update the positions of the simulation.

$$\boldsymbol{r}(t+\delta t) = \boldsymbol{r}(t) + \delta t \boldsymbol{v}\left(t+\frac{1}{2}\delta t\right) \qquad \text{Equation 3.22}$$

$$\boldsymbol{v}\left(t+\frac{1}{2}\delta t\right) = \boldsymbol{v}\left(t-\frac{1}{2}\delta t\right) + \delta t \boldsymbol{a}(t) \qquad \text{Equation 3.23}$$

In this algorithm, the position and the velocity cannot be solved simultaneously; instead the velocity at $\left(t+\frac{1}{2}\delta t\right)$ is calculated first, and then using this result, the position vector at $(t+\delta t)$ is deduced. This algorithm is superior to the Verlet algorithm in the sense that it explicitly includes the velocity term and does not require the calculation of the difference of large numbers. Since the positions and the velocities are not synchronised in this algorithm, the kinetic energy and the potential energy which are based on the velocity and positions respectively cannot be calculated for the same time step.

3.2.3.3 Velocity Verlet Algorithm

To overcome the shortcomings of the Verlet and 'leap-frog' algorithms, the Velocity-Verlet algorithm [156] was proposed, which also includes a half-step velocity calculation. This algorithm is implemented in three-stages as shown in Equation 3.24, Equation 3.25 and Equation 3.26.

$$\boldsymbol{r}(t+\delta t) = \boldsymbol{r}(t) + \delta t \boldsymbol{v}(t) + \frac{1}{2}\delta t^2 \boldsymbol{a}(t) \quad \text{Equation 3.24}$$

$$\boldsymbol{v}(t+\delta t) = \boldsymbol{v}\left(t + \frac{1}{2}\delta t\right) + \frac{1}{2}\delta t \boldsymbol{a}(t+\delta t) \quad \text{Equation 3.25}$$

$$\boldsymbol{v}\left(t + \frac{1}{2}\delta t\right) = \boldsymbol{v}(t) + \frac{1}{2}\delta t \boldsymbol{a}(t) \quad \text{Equation 3.26}$$

This algorithm gives the positions, velocities and the accelerations at the same time step and has improved precision, due to the absence of differences of large numbers in the formulae. However, it requires more computation compared to the Verlet algorithm.

3.2.3.4 Beeman's Algorithm

The Beeman's algorithm [157] gives a more accurate velocity and hence better energy conservation. However, this algorithm is more complex and requires more computational resources.

$$\boldsymbol{r}(t+\delta t) = \boldsymbol{r}(t) + \delta t \boldsymbol{v}(t) + \frac{2}{3}\delta t^2 \boldsymbol{a}(t) - \frac{1}{6}\delta t^2 \boldsymbol{a}(t-\delta t) \quad \text{Equation 3.27}$$

$$\boldsymbol{v}(t+\delta t) = \boldsymbol{v}(t) + \frac{1}{3}\delta t \boldsymbol{a}(t+\delta t) + \frac{5}{6}\delta t \boldsymbol{a}(t) - \frac{1}{6}\delta t \boldsymbol{a}(t-\delta t) \quad \text{Equation 3.28}$$

3.2.4 Equilibrium Ensembles

Molecular dynamics employs an ensemble, which maintains the thermodynamic state of the system, a constant. Different ensembles exist based on the conserved thermodynamic parameter, and each ensemble is briefly introduced below. In every ensemble, the number of particles in conserved and the notation gives which variables are maintained constant.

- **NVE-** also known as the micro-canonical ensemble, which is characterized by constant number of atoms (N), fixed volume (V) and fixed energy (E) corresponding to adiabatic systems where temperature and pressure are unregulated.
- **NPT-** the isobaric-isothermal ensemble that conserves the number of atoms (N), pressure (P) and temperature (T). This ensemble is only applicable to periodic systems.

- **NVT-** is also known as canonical ensemble where the number of atoms (N), volume (V) and temperature (T) are conserved. The temperature is controlled through a thermostat, which is discussed in section 3.2.5.

- **NPH-** is also referred as the isenthalpic-isobaric ensemble, and conserves the number of atoms (N), pressure (P) and enthalpy (H). This ensemble is only applicable to periodic systems.

3.2.5 Thermostats and barostats

- **Velocity rescaling-** this approach adjusts the temperature of individual particles by scaling the velocity in each step. This method offers the advantage of straightforward application, which adds or subtracts energy from the system efficiently. It is however limited in generating a realistic thermodynamic ensemble due to not allowing natural temperature fluctuations of a system. Therefore, this is more suitable for equilibrating a system rapidly to a desired temperature, but not for production phase.

- **Noosé and Noosé-Hoover dynamics-** this thermostat acts as a chain, where an additional degree of freedom is added to the system, to represent the interaction between the system and the heat bath. The added fake degree of freedom has a mass Q and a potential. The Q value should be chosen appropriately, such that it is not too small making the system not canonical or too large leading to inefficient temperature control.

- **Langevin-** this thermostat models a group or smaller particles as a single larger particle.

- **Andersen –** This thermostat includes two approaches, where one approach is to control the temperature by randomizing the velocities of all the atoms at a predefined collision period and the other version chooses collision period through Poison distribution at each time step and the temperature is adjusted according to the Boltzmann distribution.

3.2.6 General simulation procedure

In this thesis for the MD simulations, Forcite module [158] in Materials Studio software and LAMMPS software (Large-scale Atomic/Molecular Massively Parallel Simulator) [159] which is

an open source-code developed by Sandia National Laboratories, were used. The choice of software was based on the availability of potential data suitable for the system within the software, availability of computational resources and the computational time. The atomic coordinates for the membrane layer were obtained from structures optimized using DFT simulations and the simulation box with gas molecules was built with the 'Packing' task in the Amorphous Cell Module in Materials Studio. This generates randomly positioned gas molecules within a 3-D crystal of predefined dimensions with desired gas density. The molecular images are generated by Materials Studio visualizer or GaussView.

The detailed simulation settings are given under each chapter, however, a brief introduction to LAMMPS simulation procedure and the common commands used are given here, and compared with Forcite settings, whenever a significant difference can be identified. LAMMPS executes a simulation by reading commands from an input script. An input script mainly consists of four sections as given below.

I. Initialization

- **Units-** this sets the style of the units used for the quantities defined in the input script of the simulation as well as the output data. The choice of unit style is based on personal preference or the unit style of the potential style used. As an example, when the REAX potential was used, the unit style 'real' was used since the REAX potential file supplied with the LAMMPS are parameterized with these units.

- **Boundary conditions-** this specifies the types of the boundaries used in the simulation box. In the LAMMPS MD simulations, the simulation box in X and Y directions were maintained periodic while kept fixed in the Z direction which is perpendicular to the membrane plane, to avoid gas molecules crossing to the opposite direction without diffusing through the membrane. It should be noted that in the Material Studio Forcite module, the simulation setting has to be periodic in all three directions, and therefore a pristine h-BN layer was placed at

the edge on the Z-direction, which would act as a wall blocking the gas molecules' migration to the opposite direction.

- **Simulation style-** sets the dimensionality of the simulation, which was set to 3 because all the simulation boxes were 3 dimensional.

II. Atom definition

- **Create simulation box-** the 'read_data' command was used to read the initial atomic coordinates and other atomic and molecular data such as atomic mass; charge; atom number; bond, angle and dihedral information; atom type; molecule number etc. from a data file.
- **Group-** was used to group different atom types (eg. Membrane, gas molecules) to be used in assigning fix-settings in the settings

III. Simulation settings

- **Potential settings-** the 'pair_style' command was used to set the type of pairwise interactions. The pair_style was defined based on the recommended style of the force-field type with an appropriate cut-off distance. The respective parameters for pair coefficients either were defined by numerical value or were read from the force-field parameter file (for simulations that used the REAX potential). When pair coefficients between non-identical atoms were not available within the force-field data, these parameters were defined by the mixing rule recommended by the force-field type and were implemented using 'pair_modify' command
- **Bond, angle and dihedral settings-** for either of the simulations we have carried out using LAMMPS, these parameters or settings were not required. The REAX potential, can determine the bond and angle data by itself, while for other simulations the gas molecules were defined as rigid molecules, and the membrane was kept fixed, rendering bond, angle and dihedral settings redundant.

- **K- space style-** this setting defines the long-range solver compute long-range Coulombic interactions. The 'kspace_modify slab' command was used because the use of Ewald K-space style requires the system to be periodic in all three directions. The slab keyword allows the system to be non-periodic in the Z direction by inserting a vacuum between atom slabs and removing the inter-slab dipole interactions by effectively turning off the slab-slab interactions.

- **Fix settings-** various fix settings were used for thermostating (fix nvt), to keep the membrane position fixed in space (set force) and to keep molecules rigid (fix rigid/nvt). Since the Noose-Hoover thermostat was used, the Q ratio of 100 time-steps was chosen as recommended by LAMMPS. Furthermore, 'fix wall' command was used to define the behaviour of the gas molecules at the fixed boundary in the Z-plane, which is non-periodic. For simulations using REAX potential, the wall was maintained reflective, while for simulations with rigid molecules the wall was defined as a LJ particle since LAMMPS does not allow the combination of fix rigid and fix wall/reflect.

- **Neighbour settings:** this command sets parameters that affect the building of pairwise neighbour lists. The neighbour_modify command with the keyword 'exclude' was used to turn off pairwise interaction within frozen atoms (membrane atoms) and rigid gas molecules to avoid needless computation.

- **Time-step –** Appropriate time-steps were chosen balancing the computational time and the simulation accuracy. Time-steps within the range of 0.1-0.4 fs were used in this thesis.

- **Compute-** this command will compute various properties of the simulation system

- **Output options-** the 'dump' command was used to write data files containing atomic coordinates throughout the simulation at specified intervals, and the

'thermo' command was used to write the thermodynamic data of the simulation system

IV. Run a simulation

- **Minimization-** this command was used to minimize the energy of the simulation system at the initial stage.
- **Run-** this command runs the molecular dynamics simulations.

CHAPTER 4 CARBON DIOXIDE CAPTURE BY CHARGE CONTROLLED BORON DOPED FULLERENE

This chapter details the numerical studies on CO_2 and N_2 adsorption on neutral and charged boron doped fullerene (BC_{59}). As the literature review suggests, boron doped fullerene shows interesting chemical properties, in addition to the inherent properties of fullerene making it an excellent candidate for gas adsorption applications. Owing to the nature of gas adsorption with possible chemical reactions and electron-transfer, first-principles DFT simulations were used for this study. Here we report our study on CO_2 adsorption on boron doped C_{60} fullerene in its neutral state and $1e^-$ charged state. The results show that CO_2 can form weak interactions with the BC_{59} cage in its neutral state and the interactions can be enhanced significantly by introducing an extra electron to the system while the weak adsorption of the other gases remains unaffected.

4.1 INTRODUCTION

Carbon based nanomaterials such as fullerene, carbon nanotubes and graphene offer excellent thermal and chemical stability as CO_2 adsorbents [30, 31]. Heterofullerenes are fullerene structures where one or more cage C atom/s is/are substituted by impurity atom/s [106]. Boron doped C_{60} fullerenes are one of the most structurally stable heterofullerenes [106]. Details of synthesis methods and structural properties are given in section 2.2.2.

Sun et al. [105] for the first time predicted enhanced CO_2 adsorption on $1e^-$ and $2e^-$ charged boron nitride sheets and nanotubes which show very little chemical affinity towards CO_2 in its neutral state. Also Qiao et al. [31] showed that chemical interactions between boron carbon nanotubes (B_2CNT) and CO_2 can be enhanced by introducing extra electrons to the system.

Therefore, in this study we aim to study the adsorptive properties of CO_2 on BC_{59} fullerene in both neutral and $1e^-$ charged states. To achieve a gas separation, the adsorbent should mostly interact preferentially with the targeted constituent in the gas mixture. An adsorbent for carbon capture should have stronger interactions with CO_2 gas molecules, while also maintaining negligible interactions with the other gas molecules in the gas stream. In carbon capture applications, N_2

and CH_4 are the commonly found types of gases. Therefore, to evaluate the applicability of using heterofullerenes in carbon capture and the possibility of exploiting the adsorbent's preference for one gas species over the other, this study will assess the adsorption behaviour of these two gases in neutral and charged BC_{59}.

4.2 COMPUTATIONAL DETAILS

For this adsorption study, quantum mechanical simulations were used, since they give a considerably more accurate analysis of the structures, an atomic level chemical interaction and more precise calculations of the energies of structures and reactions. The system size is less than 100 atoms; therefore, the computational resources required are reasonable, justifying the use of first-principles calculations. The first-principles density functional theory (DFT) calculations were carried out to study gas adsorption on the BC_{59} cage. The BC_{59} structure was fully optimized in the given symmetry. All the calculations were carried out at B3LYP [138, 139, 160] level of theory using the split valance polarized basis set 6-31G(d). The gas adsorption on BC_{59} was studied in neutral state and with $1e^-$ charged state. The electron distribution and transfer were analysed with Mulliken population analysis method [161]. The adsorption energies were calculated using the following equation.

$$E_{ads} = E_{gas/BC_{59}} - \left(E_{BC_{59}} + E_{\text{gas}}\right) \qquad \text{Equation 4.1}$$

Where E_{ads} is the adsorption energy, $E_{gas/BC_{59}}$ is the total energy of the BC_{59} cage with a gas molecule adsorbed on it and $E_{BC_{59}}$ and E_{gas} are the energies of isolated BC_{59} cage and an individual gas molecule respectively. For favourable adsorption, the calculated adsorption energy should be a negative value. The greater the absolute value, the stronger the intermolecular interaction between the gas molecules and the adsorbent is expected to be. When the adsorption energies of two gas species on a specific adsorbent are noticeably different, we can expect the adsorbent to preferentially adsorb only the gas species with the higher adsorption energy.

The transition state was located using the synchronous transit-guided quasi-Newton (STQN) method [162, 163], which was then fully optimized using the Berny algorithm at B3LYP/6-31G(d)

level. The optimized transition structure was used for IRC calculations at the same level of theory [164, 165]. All calculations were carried out using Gaussian 09 package [146], and the GaussView 5 package [147] was used to visualize optimized molecular structures, molecular orbitals and charge distribution.

4.3 RESULTS AND DISCUSSION

First, the structural changes induced by the single carbon atom in the C_{60} fullerene by a B atom were analysed. The simulation results returned that the atom substitution causes charge transfer between C and B atoms which results in an unbalanced charge distribution in the fullerene cage. The unbalanced charge distribution forms B-C complex sites for CO_2 adsorption. Here we considered two possible sites for CO_2 adsorption: the B-C atomic site between two hexagonal rings (HH B-C site, where HH denotes hexagonal-hexagonal) and two identical B-C sites between a hexagonal ring and pentagonal ring (HP B-C site, where HP denotes hexagonal-pentagonal).

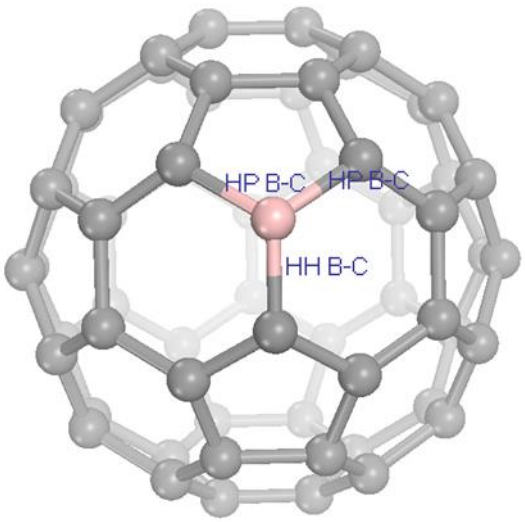

Figure 4.1: Sites for CO_2 adsorption on BC_{59}. The B and C atoms of HH B-C and HP B-C sites are represented as 'ball and bond' type and the rest of the atoms are represented as 'wireframes'. Atom colour code: grey, carbon; pink, boron.

Comparison of the two fully relaxed geometries shows that the boron atom substitution induces structural changes on the fullerene cage. The B-C bond length at HH B-C site increases to 1.5Å from 1.39Å for a typical C-C bond between two 6-member rings. The B-C bond at HP B-C site increases to 1.54 Å from the usual bond length of 1.45Å of the pristine fullerene structure. The bond angle decreases slightly to 118.5° for the C-B-C bond angle at HH B-C site, from the original angle of 120° for a bond angle between two 6-member rings of the pristine C_{60} fullerene. Similarly, the C-B-C angle at the HP B-C site decreases to 106.3° from the 109.5°.

4.3.1 CO_2 Adsorption on uncharged BC_{59} fullerenes

According to our simulation results, the CO_2 molecules can only form weak interactions with BC_{59} cage in its neutral state. The physisorption energy is a weak -2.04 kcal/mol (-4.1 kcal/mol for B97D/6-31G(d) calculations) and the weak interactions are mainly due to the van der Waals interactions between the CO_2 and the adsorbent molecule. As shown in the CO_2 physisorbed configuration in Figure 4.2, the CO_2 molecule sits parallel to the boron-carbon plane of the BC_{59} fullerene cage. The B ⋯ O and C ⋯ O bond distances are 3.25 Å and 3.71 Å respectively. The CO_2 molecule undergoes only slight structural changes upon physisorption on the uncharged BC_{59} fullerene cage. The O-C-O angle is barely changed to 179.717° from 180° and the changes to the C=O bond lengths are negligibly small. The doped fullerene cage hardly undergoes any structural change. The charge transfer between CO_2 and BC_{59} is only 0.008 e. These minimal alterations to the gas and the adsorbent molecules indicate a minimal interaction between the adsorbate and the adsorbent. Therefore, a neutral boron doped fullerene is not effective in carbon capture applications.

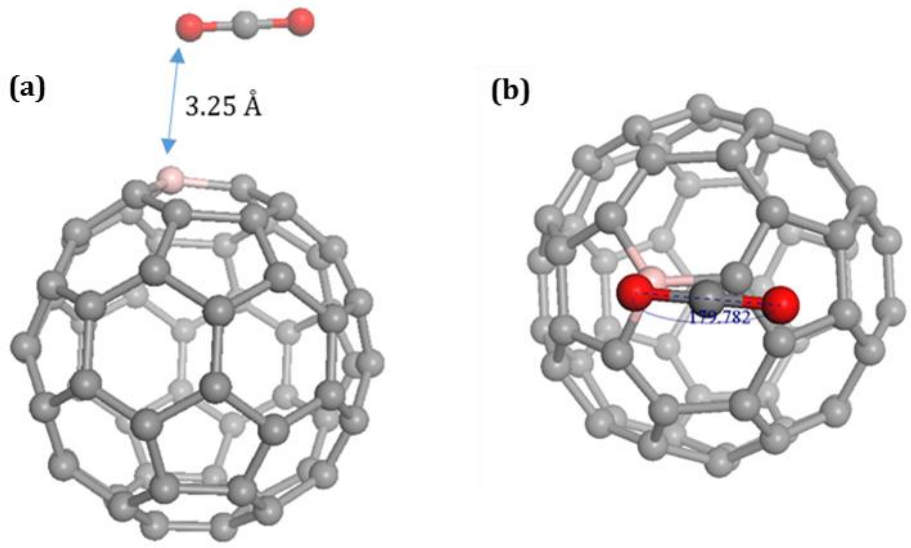

Figure 4.2: CO_2 physisorbed configuration on neutral BC_{59}. (a) Front view and (b) top view. Atom colour code: grey, carbon; pink, boron; red, oxygen

4.3.2 Effects of charges on the structure

Next, the influences of introducing an additional electron to a boron doped BC_{59} fullerene was analysed using Mulliken charge analysis and the electron density distributions of lowest unoccupied molecular orbitals (LUMO). Due to its isoelectronic analogy with C_{60}, Kim et al. [166] predicted that $C_{59}B^-$ should be a stable entity. This claim was validated by experimental observations by Dunk et al. [112]. Figure 4.3 shows that the LUMO of the neutral BC_{59} is concentrated on the B atom and the neighbouring C atoms. This observation is consistent with experimental results of Guo et al. [110] which showed that boron doping creates an electron defficient site on the B atom on the cage. This suggests that an additional electron added to the system, will be accepted by the B atom. This hypothesis is supported by theoretical predictions of Kurita et al. [13] and Xie et al. [167] who stated that the doped B atom on C_{60} fullerene exists as an electron acceptor.

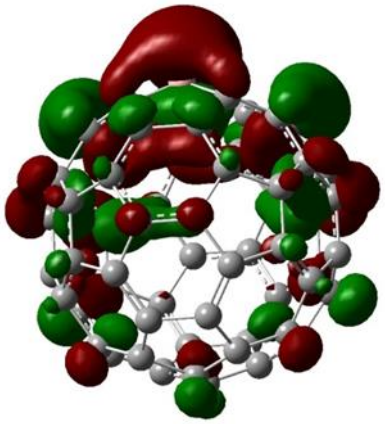

Figure 4.3: LUMO of neutral BC_{59}. The orbitals are drawn at isosurface value 0.02. The colours of the orbitals: red, positive wave function; green, negative wave function. Atom colour code: pink, boron; grey, carbon

Comparison of Mulliken population analysis of neutral and $1e^-$ charge-state of the BC_{59} structure proves that the B atom essentially accepts the negative-charge introduced to the system. The Mulliken atomic charge of the B atom in BC_{59} structure in neutral state has changed from 0.138 to 0.012 upon the introduction of the negative charge, while as shown in Figure 4.4 the negative charges on the C atoms are only slightly changed.

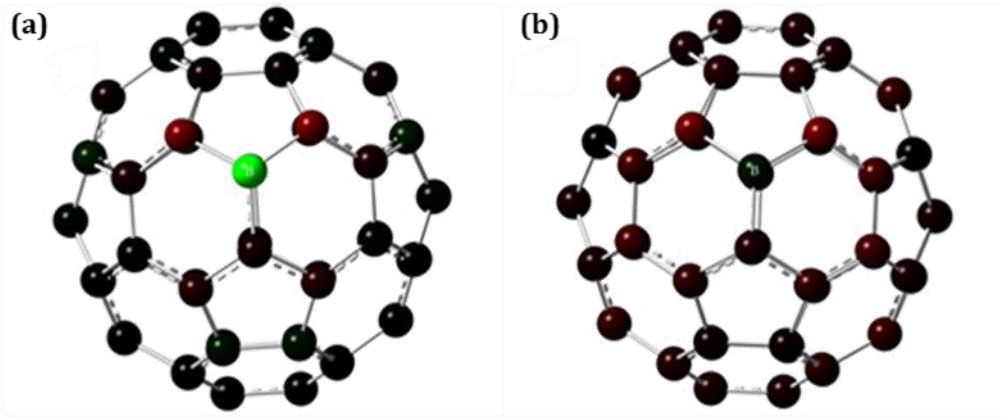

Figure 4.4: Mulliken charge distribution of (a) neutral BC_{59} and (b) 1e- BC_{59}. The atoms are shaded based on the charge distribution on each atom. The comparison suggests that the most notable charge transfer is on the boron atom

4.3.3 CO_2 adsorption on BC59 fullerene in $1e^-$ state

Next, we studied the CO_2 adsorption on a $1e^-$ charged BC_{59} cage. The results confirm that the negatively charged BC_{59} fullerene exhibits stronger interaction with CO_2. Unlike with the neutral BC_{59} where the interaction with CO_2 molecule was only physical, here the charged BC_{59} forms a substantial chemical interaction with CO_2 causing the molecule to undergo significant structural deformations. Out of the three possible sites investigated, the CO_2 adsorption on the HH B-C site was the strongest. The chemisorbed configurations of CO_2 adsorbed on the HP B-C site or on the HH C-C site have positive reaction energies, indicating the formed configuration is unstable. However, CO_2 chemisorption on the B-C site bordered by two hexagonal rings: the HH B-C site, has a negative adsorption energy.

In CO_2 adsorption on the HH B-C site, a chemisorption energy of -15.41 kcal/mol (-64.48 kJ/mol) (-13.48 kcal/mol with BSSE correction) is observed which agrees well with the ideal range of chemisorption energy (40-80 kJ/mol) for a good CO_2 adsorbent [168]. The Gibbs free energy of the reaction can be calculated using the Equation 4.2, where $\Delta G, \Delta H$ *and* ΔS are the changes in Gibbs free energy, enthalpy and entropy, respectively and T is the absolute temperature.

$$\Delta G = \Delta H - T\Delta S \qquad \text{Equation 4.2}$$

The calculated Gibbs free energy for CO_2 physisorption on the charged BC_{59} fullerene structure, using the thermochemistry data obtained from Gaussian simulations is -3.93 kcal/mol at 298.15K and 1atm. Since a negative Gibbs free energy implies a spontaneous reaction at the given temperature, the CO_2 chemisorption on the charged structure is a spontaneous process.

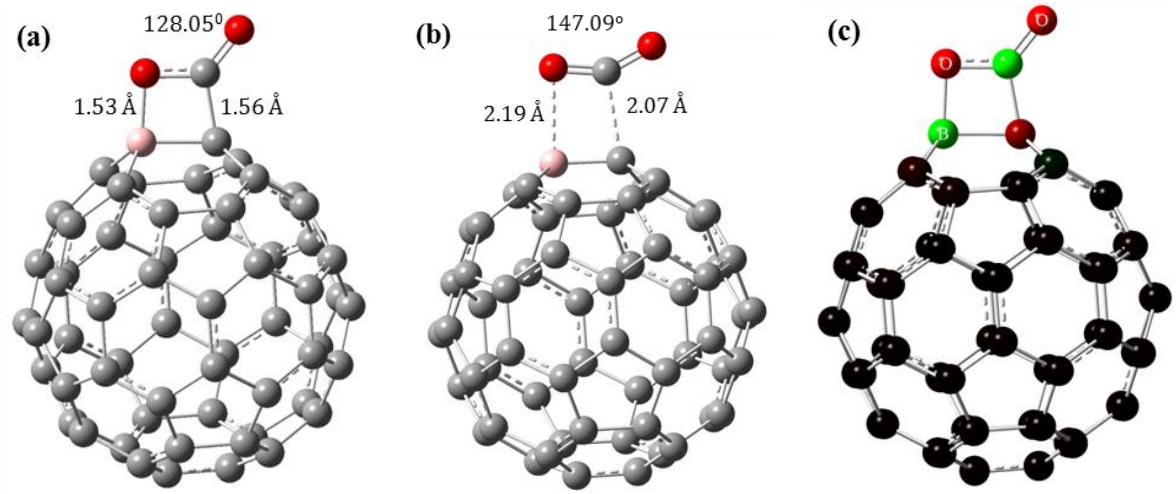

Figure 4.5: (a) CO_2 chemisorption and (b) Transition structure for CO_2 chemisorption on negative 1e- charge BC_{59}. Atom colour code: grey, carbon; pink, boron; red, oxygen. (c) Charge distribution after CO_2 chemisorption

The CO_2 molecule undergoes considerable distortion upon chemically adsorbing on the $1e^-$ charged BC_{59} fullerene. A C=O bond of the CO_2 molecule is broken while one oxygen atom forms a bond with the boron atom (which will be referred as O_a in the following discussion and the other oxygen atom as O_b). The carbon atom of the CO_2 molecule forms a bond with the carbon atom on the HH B-C site of the cage structure. The linear O-C-O bond of CO_2 is bent to 128.05° in the adsorbed form. The C=O_b bond which is originally 1.169Å (experimentally 1.162 Å [123]) is elongated to 1.208 Å, while the C-O_a bond length has expanded to 1.336 Å.The adsorption site of the BC_{59} fullerene also undergoes considerable stretching. The HH B-C site is protruded outwards by ~0.05 Å. The B-C bond of the HH B-C site has stretched to 1.672 Å from 1.496 Å. The Mulliken population analysis shows that a charge transfer of 0.42 has occurred from the BC_{59} fullerene to the CO_2 molecule. Comparison of the charge distribution on BC_{59}^- before (Figure 4.4 (b)) and after (Figure 4.5 (c)) CO_2 adsorption, confirms that the injected electron is occupied by the CO_2 molecule.

The higher adsorption energy and significant distortions in the structures confirms a stronger interaction between the CO_2 molecule and the negatively charged BC_{59} than its neutral state. These interactions can be explained due to the Lewis acidity of CO_2, which prefers to accept electrons [31]. On the other hand, the B atom of the BC_{59} becomes less positively charged upon the addition of an extra electron. Therefore, it becomes more likely to donate electrons to the CO_2 molecule leading to stronger interactions between the two molecules.

Figure 4.6 shows the minimum energy pathway for the adsorption from the physisorbed state to the chemisorbed configuration. We performed frequency calculations on the optimized transition structure which confirms it is a first order saddle point and hence an actual transition structure. From this figure, the activation barrier for the chemisorption is estimated to be 13.25 kcal/mol (55.43 kJ/mol). The low barrier to the reaction indicates that the reaction is energetically favourable.

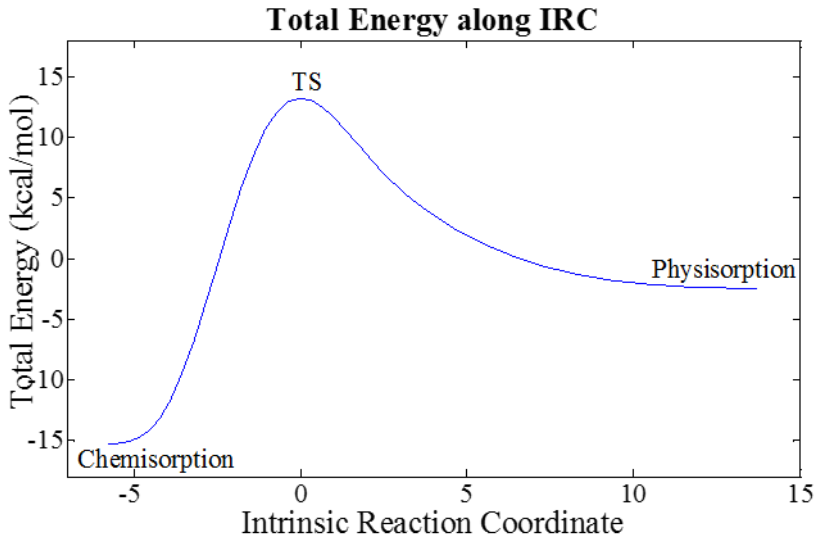

Figure 4.6: : Intrinsic reaction pathway for CO_2 chemisorption on 1e- charged BC_{59} from its physisorbed configuration. The total energy = 0 point corresponds to the total energy of $E_{CO_2} + E_{BC_{59}}{}^{-1}$

For CO_2 desorption, the removal of the added charge will decrease the stability of the bond between CO_2 and the doped fullerene. The thermodynamic analysis of the reaction shows that the CO_2 chemisorption is spontaneous only for temperatures less than 350K. Therefore, we suggest using a combination of manipulating the charge state and the temperature of the system for

adsorbent recycling. This kind of method eliminates the need for pressure swing recycling, which demands large energy requirements for adsorbent regeneration and expensive process equipment required for pressurized systems. Charging the system can be achieved by electro chemical method, electrospray, and electron beam or gate voltage control methods [105].

4.3.4 N_2 and CH_4 adsorption on neutral and charged BC_{59}

To analyse the effectiveness of employing BC_{59} for CO_2 separation, we analysed the adsorptive behaviour of N_2 and CH_4 on charged and neutral BC_{59}. The N_2 gas molecules would only weakly physisorb on the BC_{59} structure irrespective of its charged state. The N_2 physisorption energy of the charged state barely increases to -0.93kcal/mol from the weak physisorption energy of -0.43 kcal/mol of the respective physisorption on a neutral BC_{59} molecule. The N_2 molecule sits at a distance of 3.4 Å from the boron atom of the BC_{59} fullerene. In charged and neutral physisorption, any charge transfer between the gas molecule and the adsorbent is negligible. Similarly, the, adsorbent or the gas molecule hardly undergoes any structural alterations.

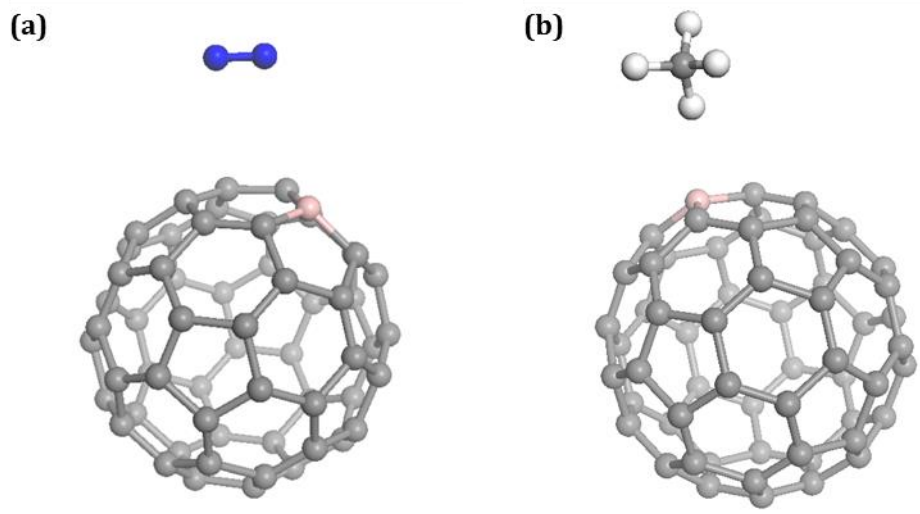

Figure 4.7: The physisorbed configurations of (a) N_2 and(b) CH_4 on a boron doped $C_{59}B$ fullerene. The physisorbed configurations essentially remains the same irrespective of the electric field of the system. Atom colour code: white; hydrogen; pink, boron; grey, carbon; blue, nitrogen.

Similarly, the CH_4 gas molecule only forms a weak vdW bond with the adsorbent. Similar to the N_2 adsorption, the methane adsorption hardly sees any difference in the adsorption behaviour with the alteration of the charged state of the adsorbent. The weak physisorption energy is slightly increased from -0.43 kcal/mol to -1.11kcal/mol when the adsorbent is introduced with

an electron. The CH_4 molecule is physisorbed at a distance of 3.6 Å from the BC_{59} fullerene. Similar to the N_2 physisorption, the adsorbent or the gas molecule barely undergoes any structural changes and minimal charge transfer occurs between the two molecules.

4.3.5 Discussion

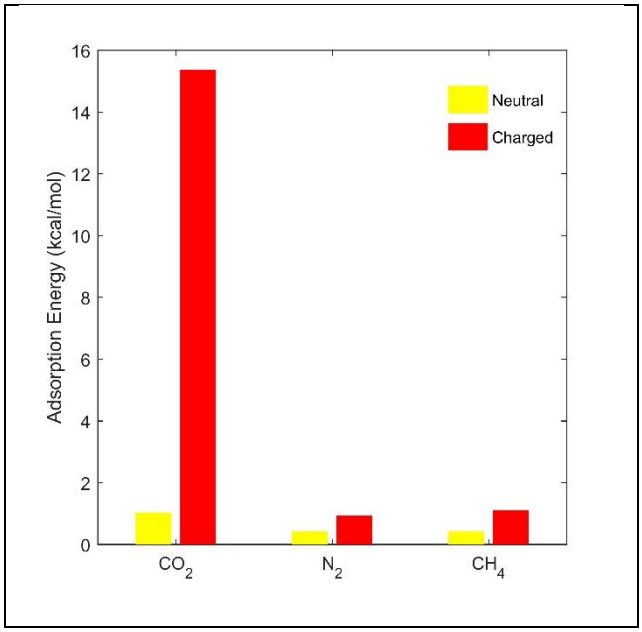

Figure 4.8: Comparison of adsorption energies of each gas type on a neutral BC_{59} fullerene and when the adsorbent is under a (-1) electric field

This study focuses on assessing the feasibility of using fullerene-based materials, which inherently have favourable chemical, mechanical and thermal properties to be used as gas adsorbents in industrial conditions. The study successfully incorporates a combination of chemical functionalization and charge tuning to achieve effective CO_2 separation. Figure 4.8 graphically compares the influence of the electric field on adsorption energies of the three gas molecules. The profound change in the CO_2 gas molecule's adsorption behaviour, when the adsorbent is under an electrical field, makes it a suitable candidate for CO_2 adsorptive separation. The electrophilic nature of CO_2 leads to the stronger interaction and charge transfer with the boron atom, which takes most of the introduced electron charge to the system. Upon adsorption, the CO_2 molecule undergoes significant structural alterations. Because adsorption is controlled by varying the electric field, this adsorption system would not require large pressure changes to regenerate the adsorbent. In fact, a combination of charge control and considerably smaller pressure swinging can be used to extract the adsorbed gas molecules from the adsorbent. This will address one of the inherent downsides in adsorption gas separation to a certain degree.

However, in contrast to the CO_2 adsorption on BC_{59} fullerene, the alterations to N_2 and CH_4 adsorption behaviour by charge tuning is insignificant. Both gases only weakly physisorb on the

BC_{59} fullerene irrespective of the adsorbents charge state and hardly undergoes any structural changes. Considering the strong chemisorption of the CO_2 through charge tuning and the noticeably weak interactions between the N_2 gas molecules and the adsorbent, this kind of adsorbents can find applications in carbon capture from flue gas. The main constituents of a flue gas stream are N_2 and CO_2. The preferential adsorption of CO_2 over N_2 will lead to effective separation of CO_2 from N_2. Combining the selective gas adsorption of boron-doped fullerene with its high thermal and mechanical stability inherited from pristine C_{60} fullerene structures, make this structure a suitable adsorbent to be used in conditions in a flue gas outlet. Similarly, CO_2 removal from gas mixtures primarily containing CO_2 and CH_4 is essential in industrial processes in natural gas sweetening and biogas upgrading. Similar to CO_2/N_2 separation, the substantial differences in the adsorption energies between CO_2 and CH_4 on BC_{59} under an electric field can be exploited to effectively remove CO_2 gas molecules from gas streams containing gas mixtures of CO_2 and CH_4 found in the aforementioned industrial applications.

4.4 CONCLUSION

Using DFT calculations, we have studied the adsorption mechanisms of CO_2 on a C_{60} fullerene cage where a single C atom is substituted by a B atom. Our calculation results show that the BC_{59} cage, in its neutral state shows low chemical interaction with a CO_2 molecule, which only physisorbs with an E_{ads} of -2.04 kcal/mol. However, the CO_2 adsorption on the BC_{59} can be significantly enhanced by injecting the structure with negative charges. The CO_2 molecule chemisorbs on the $1e^-$ charged BC_{59} with an E_{ads} of -15.41 kcal/mol. On the other hand, the N_2 and CH_4 adsorption on both neutral and charged BC_{59} remains physical. This study suggests that we can conclude $1e^-$ charged BC_{59} cage structure is a promising CO_2 adsorbent.

CHAPTER 5 POROUS HEXAGONAL BORON NITRIDE MEMBRANES FOR GAS SEPARATION

This chapter details the theoretical analysis of porous hexagonal boron nitride membranes for gas purification. These studies also evaluated the possibility of increasing the targeted gas permeability across the membrane, while keeping its selectivity intact by subjecting the membrane to minor external biaxial strains. The expectation is that a small biaxial strain will cause the porous area to increase slightly, sufficient to improve the permeability of the targeted gas molecules, but not too high to alter the impermeability of impurity gas molecules. *Ab initio* DFT simulations are used to optimize the membrane geometries with and without added strains. Classical MD simulations are used to study the gas permeability across the membrane.

Boron nitride is the most commonly studied two-dimensional graphene-like structure after graphene itself. A number of studies have been carried out to analyse the use of porous graphene monolayers as a membrane in gas separation and water desalination as mentioned in section 2.1.2.1. Motivated by such studies, here we analyse the prospects of porous boron nitride membranes in gas separation applications. The superior structural properties due to its graphene-like nature and unique properties inherent to boron nitride, makes it an interesting candidate for gas separation membrane. In this study, hexagonal boron nitride is chosen due to its similarity to graphene and excellent chemical and structural stability. Similar to graphene and other 2D monolayer membranes proposed such as porous MoS_2 membranes, the pores can be created by removing a number of chosen atoms to create a pore with desired shape and size. Techniques to remove atoms from a pristine monolayer are discussed in detail in section 2.1.2.5.

In this chapter, the permeability of H_2, CO_2, N_2 and CH_4 through porous h-BN is evaluated where the study focuses on different pores distinguished by the shape, the number of atoms removed or the type of atoms (boron or nitrogen) at the pore rim. Furthermore, the effectiveness of strain tuning to control the desired gas permeability and selectivity is explored. While first-principles quantum mechanical simulations were used to obtain optimized geometries of the created

nanoporous structures, non-equilibrium molecular dynamics simulations were used for gas permeability study. Section 5.2 includes the detailed computational details while section 5.3 presents the results of molecular dynamics simulations.

5.1 POROUS BORON NITRIDE STRUCTURES

The nanoporous h-BN membranes are created by selectively removing boron and nitrogen atoms from a pristine hexagonal boron nitride monolayer. The edge of the pores, the dangling boron and nitrogen bonds, are terminated with hydrogen atoms. The types of pores created and evaluated for gas permeability for this study are shown in Figure 5.1 and Figure 5.2. The choice is based on the dimensions of the pores and the gases' kinetic diameters. In this thesis, the different pore types are identified by the number of removed atoms. In pore-10, 5 each of boron and nitrogen atoms are removed and the pore edges are terminated with eight hydrogen atoms. In this porous structure, the length of the pore is aligned in the zigzag direction of the hexagonal boron nitride monolayer. A similar pore shape with similar dimensions could be obtained by removing four of each boron and nitrogen atoms, but aligning the length of the pore along the armchair direction. In this case, however, the terminating hydrogen atoms will be too close to each other and make the pore structure unstable as shown in Figure 5.1. Therefore, this pore is not studied for gas separation in this thesis.

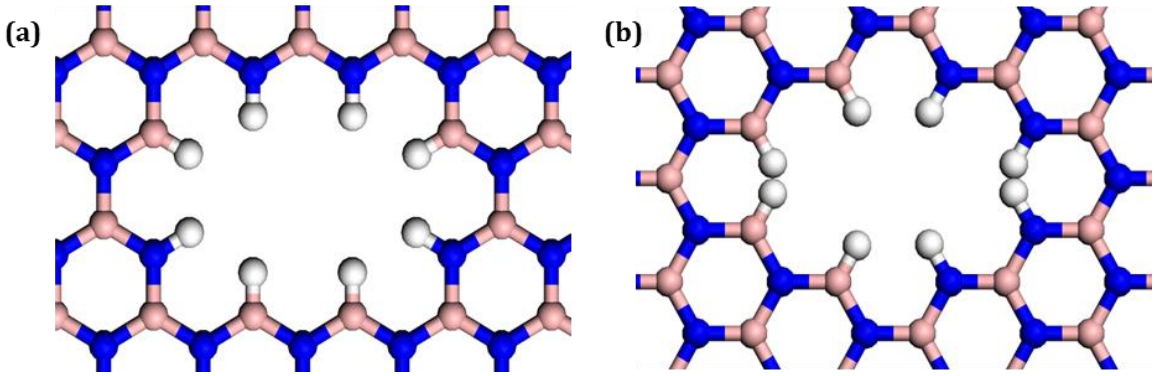

Figure 5.1: (a) Pore-10 and (b) Pore-8. These two pores have similar openings, however the difference in alignment of length of the pore opening along the zigzag edge or the armchair edge make them structurally different and therefore affects its structural stability. Atom colour code: hydrogen, white; boron, pink; carbon, grey; nitrogen, blue.

In pore-13-B, six boron atoms and seven atoms are removed and the pore edge is terminated with nine hydrogen atoms. In this pore, the edge of the pore consists predominantly of boron

atoms, and it is therefore denoted as pore-13-B. As shown in Figure 5.2, the pore-13-N has a similar shape to pore-13-B, but has more nitrogen atoms at the edge of the pore with 6 nitrogen atoms and 7 boron atoms removed and 9 hydrogen atoms terminating the pore edges. Similar to pore-10, these two pores can be modified by swapping the alignment from along the zigzag direction to along the armchair direction. However, these two configurations also make the terminating hydrogen atoms too close to each other, and therefore leading to a less stable structure. Hence, those two configurations are ignored in this study. The difference in the pore edge leads to different pore dimensions and different behaviour under strain.

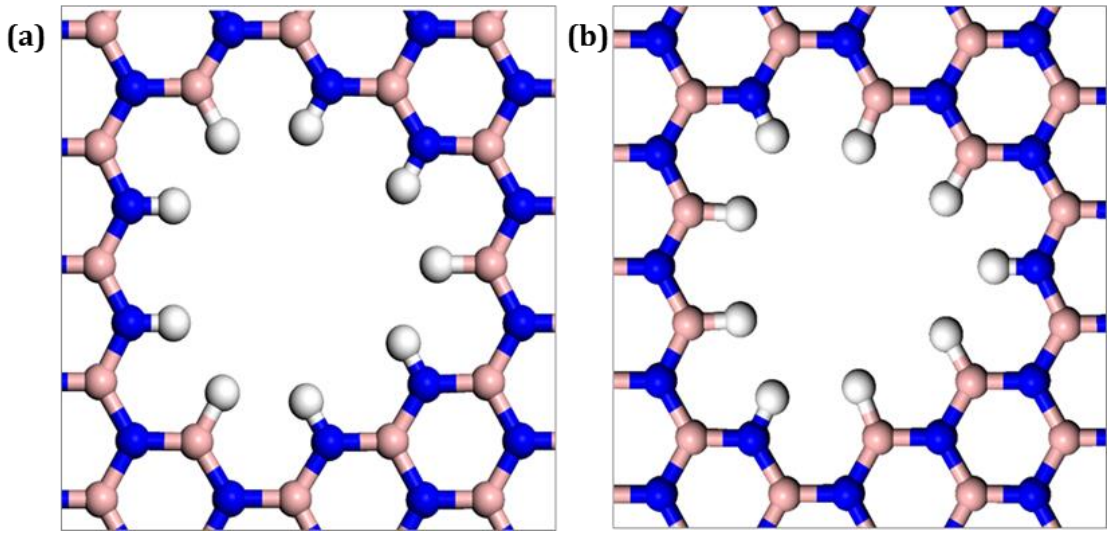

Figure 5.2: Pore-13-B and Pore-13-N. The predominant atom type at the edge of the pore opening distinguish these two similar looking pore openings. Atom colour code: hydrogen, white; boron, pink; carbon, grey; nitrogen, blue.

5.2 COMPUTATIONAL DETAILS

In this study, molecular dynamics simulations were used to analyse the H_2, CO_2, N_2 and CH_4 permeation across the membrane, and first-principles DFT calculations were used for geometry optimization of boron nitride monolayer and various porous structures.

5.2.1 Density Functional Theory Calculations

All DFT calculations were carried out using the DMol3 module in Materials Studio [144, 145]. First, a pristine boron nitride supercell approximately of 25 Å × 25 Å was built and fully relaxed. Next, pores were created in the optimized pristine boron nitride membrane as mentioned in section 5.1. The various pore structures were fully relaxed, allowing the relaxation of both atomic

positions and the lattice parameters. Finally, the lattice size was increased by 2.5 and 5% to mimic the porous membrane being under biaxial strain of respective value. For these geometry optimizations, the lattice parameters were kept fixed while allowing the atomic positions to relax.

The generalized gradient approximation treated by the Perdew-Burke-Ernzerhof exchange correlation [135] with a basis set of all electron double numerical plus polarization (DNP) was used for the final DFT geometry relaxations. The DFT-D method developed by Grimme et al.[169], was used for the long-range van der Waals corrections. A three dimensional crystal with a vacuum slab of 10 Å between sheets in the Z-direction was used. The Brillouin zone was sampled by 4x4x1 k-points using the Monkhorst-Pack scheme[170]. Atomic charges were calculated using the Mulliken charge analysis [161]. The convergence tolerance parameters were set as below.

Energy	:	2.0×10^{-5} Ha
Maximum force	:	4×10^{-3}Ha/Å
Maximum displacement	:	5×10^{-2} Å
Maximum iterations	:	50
Maximum step size	:	0.3 Å
Self-Consistent Field tolerance	:	1.0×10^{5}
Maximum SCF cycles:	:	50
Multipolar expansion	:	Octupole

5.2.2 Molecular Dynamics Simulations

All MD simulations were performed using the Forcite Module in Materials Studio package. The simulation box was setup with a frozen ~25 × 25 Å monolayer of porous BN with a single pore, obtained from DFT geometry optimizations. It was placed at the middle of the simulation box, as shown in Figure 5.3. Periodic boundary conditions were applied in all three directions and a non-porous pristine boron nitride layer was fixed to separate the vacuum phase. Initially 80 gas molecules were placed in one side of the membrane, which behaves as the gas reservoir.

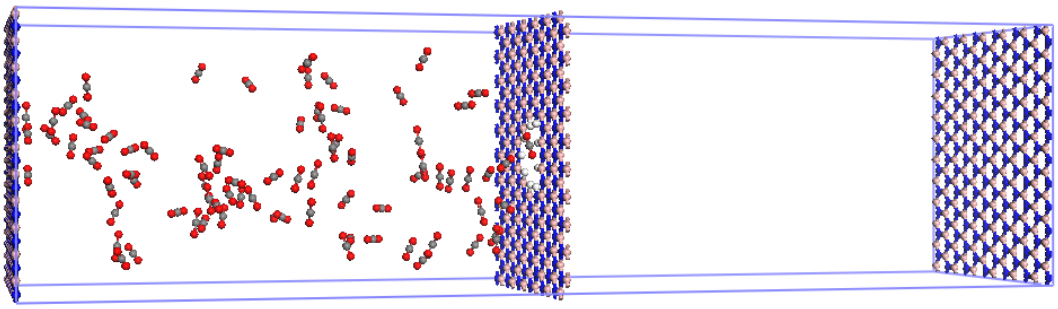

Figure 5.3: Simulation box setup for MD simulations. The length of the simulation box is reduced for illustrative purposes. Atom colour code: white. hydrogen; pink, boron; grey, carbon; blue, nitrogen; red, oxygen.

Simulations were carried in the NVT ensemble, with the Nosé thermostat to maintain system temperature at 298.0 K. The system was equilibrated for 100 ps using velocity scale thermostatting with a temperature difference of 2.5 K. Next production simulations were carried out for a total time-period of 10ns with a time-step of 0.25 fs. The number of gas molecules in the feed is chosen such that the initial feed pressure is approximately 50 bar (calculated assuming ideal gas behaviour). However, this value is reduced during the simulation period due to the following reasons.

- Gas molecules crossing through the membrane reduces the number of molecules in the feed side
- Molecular adsorption of gas molecules on the membrane. The adsorbed gas molecules are considered to be in the solid phase and may not contribute to the overall pressure in the gas phase reducing the total pressure of the simulation system.

The atom trajectories were recorded at every 1000 step (25 fs) and the Z coordinates of the gas atoms were extracted by running a Perl script. Only the Z-coordinates were extracted, because it is the most important in identifying the gas transport behaviour through the nanopores. Next, the Z-coordinate matrix was post processed using Matlab codes written to analyse the gas permeation behaviour.

The simulation parameters used in this simulation are summarized below.

Simulation setting	:	Value
Ensemble	:	NVT
Temperature	:	298.0 K
Thermostat	:	Nosé
Q- ratio	:	0.01
Time step	:	0.25 fs
Number of steps	:	40000000
Initial velocities in equilibration	:	Random
Initial velocities in production	:	From equilibration simulations
Charges	:	Mulliken Analysis from DFT simulations
Electrostatic summation method	:	Ewald
Electrostatic summation accuracy	:	0.01 kcal/mol
Electrostatic summation buffer width	:	0.5 Å
van der Waals summation method	:	atom based
van der Waals cut-off distance	:	12.5 Å
Spline width	:	1 Å
Long range correction	:	Yes
Buffer width	:	0.5 Å

5.3 RESULTS & DISCUSSION

First, the pore dimensions of the optimized membranes were analysed and the results are summarized in Table 5.1. As expected, the pore-10 has the smallest pore opening due to the lower number of atoms being removed to form it. Interestingly, a comparison of the pore dimensions of pore-13-B and pore-13-N shows that the latter has a reasonably larger pore area compared to the former despite having the same total number of atoms removed from the monolayer. The only difference between the two kinds of pores is the type of atom species on the edge rim. When the distances between the boron or nitrogen atoms at opposite ends of the pore rims (ignoring the terminating hydrogen atoms) are compared, it is evident they are almost similar in values.

Therefore the increased pore area is largely due to the much shorter N-H bond length of 1.02 Å (according to our DFT calculations, which is also confirmed by previous theoretical values published in literature) compared to the B-H bond length of 1.21 Å, which causes the noticeable difference in the pore dimensions.

The three different pores were subjected to 2.5 and 5% biaxial strains, where the strains were modelled by increasing the unit cell size by the respective strain values. Then energy minimization simulations were carried out, allowing the atomic positions to relax but keeping the altered lattice dimensions fixed. Table 5.1 summarizes the changes to the critical pore dimensions of the three pores under biaxial strain. Analysis of structural changes caused by biaxial strain shows, how most of the changes observed, occurred at the pore opening. This behaviour is expected due to the absence of interatomic bonds to resist the deformation due to straining, while the bonds within unaltered regions, hardly undergo any changes due to the stronger interatomic attractions.

Table 5.1: Summary of structural changes induced by biaxial strain

	Strain Percentage (%)	D1	D2	D3	D4
Pore-10	0	3.83	5.52	6.02	-
	2.5	4.24	5.83	6.38	-
	5	4.66	6.12	6.74	-
Pore-13-B	0	5.78	5.32	6.00	6.10
	2.5	6.21	5.83	6.39	6.49
	5	6.58	6.24	6.88	6.95
Pore-13-N	0	5.52	5.89	6.08	6.16
	2.5	5.86	6.30	6.44	6.57
	5	6.22	6.72	6.88	7.03

5.3.1 Gas permeation study

The gas permeability of the membrane was evaluated with non-equilibrium molecular dynamics simulations. Figure 5.4 shows the temperature and energy variation during the simulation period.

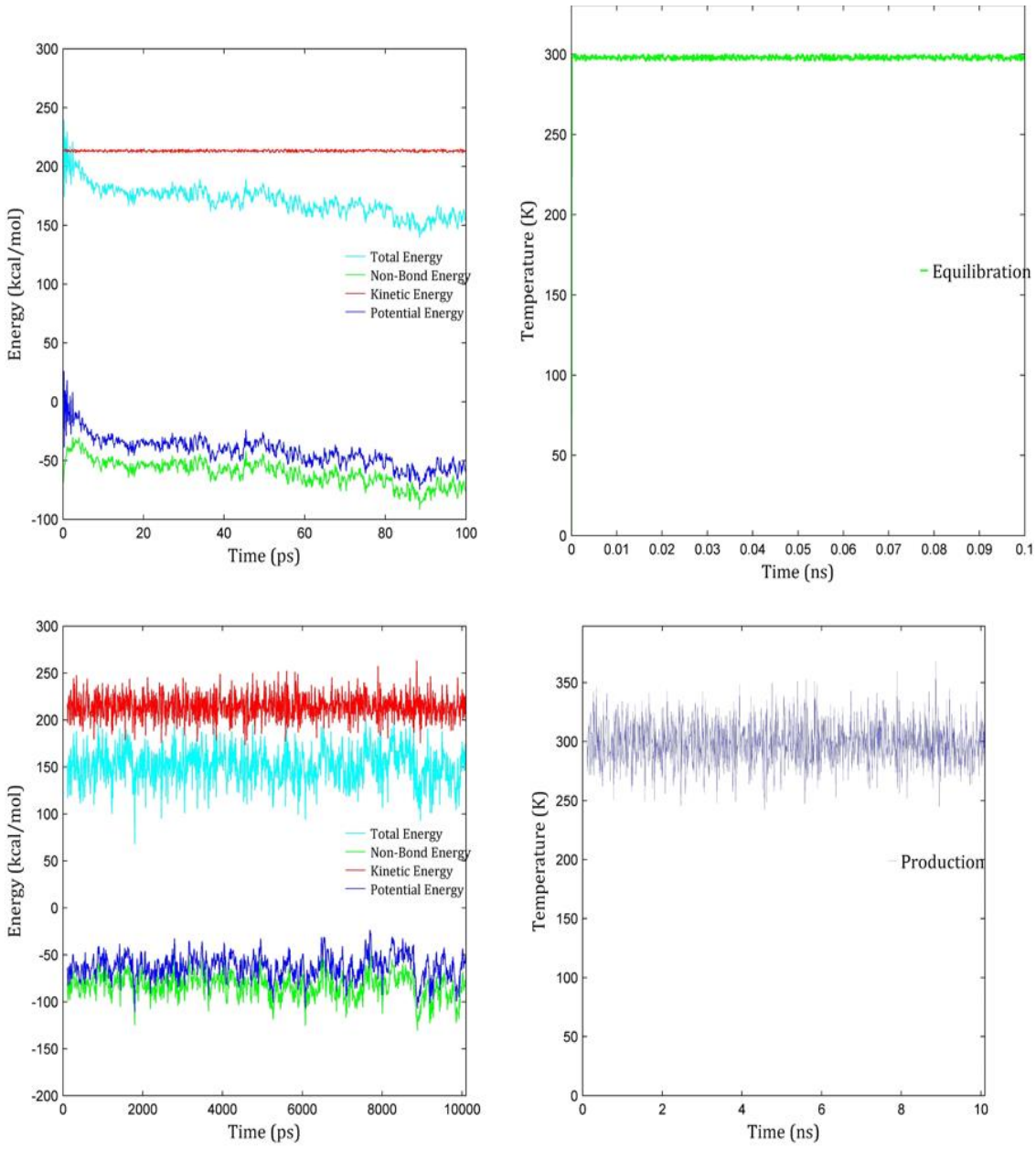

Figure 5.4: Temperature and energy variation during equilibration and production simulations. These results are sample representations from the CO_2 permeation through pore-13-B subjected to 5% biaxial strain

Analysis of the molecular trajectories confirms that the chosen time step is appropriate. The permeability across porous boron nitride is evaluated by quantifying the molecular crossings, across the three different pores studied under various strain values. For quantified analysis, the crossings occurring during the equilibration stage of 100ps were ignored. Table 5.2 is a summary of the total number of crossings across each pore during the 10ns simulation production time. When a nano-pore under a certain biaxial strain value is permeable to the largest gas molecule, CH_4, further permeation studies for other gases and the same pore under larger biaxial strains

were aborted, because we cannot achieve any separation for the gases analysed in this study. For example, the pore-13-N will show gas permeability to all the gases because it is permeable to CH_4 under 2.5% strain. Since this is the gas type with the largest kinetic diameter, it implies that the membrane is permeable to H_2, CO_2 and N_2, all of which have smaller kinetic diameters. Therefore, no further studies were done for these gases with the membrane subjected to 2.5% or 5% biaxial strains since the latter would certainly be permeable to every gas and any significant separation based on size sieving cannot be expected.

Table 5.2: Summary of number of crossing for each gas type through the studied pore types

	Strain (%)	**H_2**	**CO_2**	**N_2**	**CH_4**
Pore-10	0	0	0	0	0
	2.5	11	0	0	0
	5	22	0	0	0
Pore-13-B	0	11	0	0	0
	2.5	310	71	19	0
	5	526	94	115	123
Pore-13-N	0	48	0	0	0
	2.5	624	Permeable to largest gas molecule CH_4-101		
	5				

5.3.1.1 Porous boron nitride for H_2 purification

The results show that the membrane with the smallest pore, pore-10 is impermeable to any gas considered in this study. Both pores, pore-13-B and pore 13-N, are only permeable to H_2, whereas they are impermeable to CO_2, N_2 and CH_4. The Figure 5.5 compares the number of H_2 molecules on the permeate side of the simulation box at each time step and the number of H_2 molecules crossings each type of porous membrane in each direction, respectively. Analysis of the trend in gas permeation, especially through pores with high permeability indicates, once the number of gas molecules on the permeate side of the membrane reaches a considerable value, the gas transport occurs in both directions. Therefore, to get an accurate estimate of the number of crossings through the porous membrane, the number of gas crossings in each direction was

recorded. The values reported in Table 5.2 and the graph in Figure 5.5 include gas-crossing events in both directions.

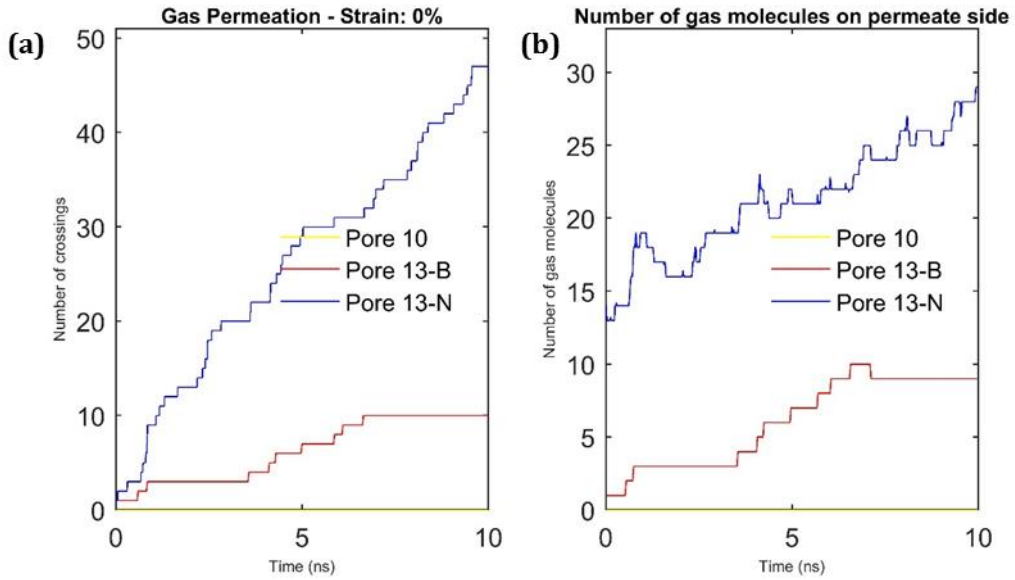

Figure 5.5: The variation of number of H_2 molecules and (b) the number of H_2 crossing events occurred during the simulation period for membrane systems under no strain. Since the pore-10 is impermeable to H_2 in the absence of strain, the plot is on the y=0 axis.

Being only permeable to H_2 gas molecules, the results suggest that the boron nitride membrane with a type of pore -13-B and pore-13-N can be effectively used for hydrogen separation from gas mixtures of CH_4 and CO_2. Out of these two types of membranes, the pore-13-N membrane, with a comparatively larger pore dimension, is more permeable to H_2 molecules. The results comparison indicates, that an approximately 5% difference of total pore area of the two types of pores, has tripled the H_2 flux across the pore.

Next, we compared the molecular permeation when the nano-membrane is subjected to biaxial strain. The results show that the h-BN membrane with pore-10 is impermeable to CO_2, N_2 and CH_4 even under 5% biaxial strains. However, the strain-induced pore area expansion leads to increased H_2 flux through the pore. Therefore, for each increase in biaxial strain by 2.5%, which effectively leads to an approximate 17% increase to the pore area, the number of H_2 crossings increase from 0 to 10 to 22, respectively. Therefore, this type of membrane subjected to biaxial strains of 2.5 and 5% can be effectively used to separate H_2 from mixtures of CO_2 and CH_4.

Similarly, the pore-13-B under a 2.5% biaxial strain, demonstrates the ability to permeate both CO_2 and H_2 gas molecules. Therefore, while it has a larger permeability for H_2 gas molecules, this membrane cannot be used for H_2/CO_2 separation applications, which is commonly required in pre-combustion carbon dioxide capture. However, due its high H_2 permeability and CH_4 screening, the pore-13-B under biaxial strains up to 2.5% is an excellent candidate for H_2 purification from gas mixtures of H_2 and CH_4. Membrane with pore-13-N, even under biaxial strains of 2.5% loses its impermeability to CO_2 and CH_4 gas molecules. Therefore, this type of membrane can only be used for H_2 purification from CO_2 and CH_4 in the absence of any strains. However, its remarkably high permeability to H_2, even in the absence of any biaxial strain, makes this membrane an ideal candidate for H_2 purification.

5.3.1.2 Porous Boron Nitride Membranes for CO_2 Capture

The membrane with pore-13-B type opening, under 2.5% biaxial strain displays reasonable CO_2 permeability across the membrane, while maintaining its CH_4 and N_2 impermeability. This characteristic is drastically changed when biaxial strain is increased to 5%. Therefore, this kind of membranes under biaxial strains around 2.5% can be proposed to separate CO_2 from CH_4 and CO_2 from N_2. In this case, under 2.5% biaxial strain, the increase in size of the opening is sufficiently large to allow CO_2 passage through it, but is not large enough for the N_2 and CH_4 passage through the pore opening. The 100% rejection of CH_4 and high permeability of CO_2 makes h-BN membranes with 13-B type pores, a suitable candidate in CO_2/CH_4 separation applications, especially in natural gas processing, where the presence of CO_2 significantly reduces the overall energy content and causes corrosion in natural gas transport pipes. Similarly, due to the membrane's demonstrated ability to extract CO_2 from N_2 with a significant difference in the flow rates, it can find applications in post-combustion carbon-capture, where CO_2 is removed from the flue gas as a mean to curb greenhouse gas emissions.

5.3.2 Discussion

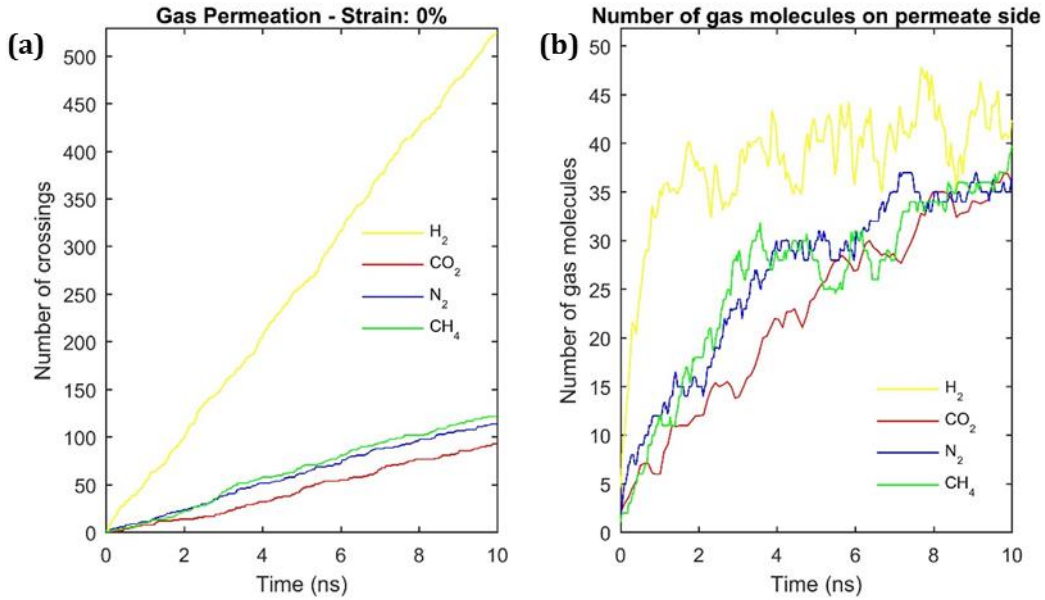

Figure 5.6: Comparison of gas permeability of Pore-13-B under 5% strain. (a) Variation of number of crossings recorded during the entire simulation period. (b) Number of gas molecules in the permeate side during the simulation period

As mentioned earlier, the membrane with pore-13-B type opening, under 5% biaxial strain is permeable to all gases investigated in this study. The results of this simulation study were used to analyse the gas permeability behaviour of each gas type through a porous hexagonal boron nitride membrane. These simulations give an insight into the gas permeability behaviour through the pore opening, but under 5% strain this kind of pore cannot achieve any separation.

Figure 5.6 (a) compares the H_2, CO_2 and CH_4 crossing events across the pore-13-B membrane under 5% strain, while Figure 5.6 (b) represents the variation of gas concentration on the permeate side of the membrane with time for each gas type. The results indicate under a higher biaxial strain and enhanced pore area; both N_2 and CH_4 gas molecules shows a slightly higher number of crossings events compared to the CO_2 gas molecules. This suggests when the pore area is increased, the physical barrier to gas atoms crossings is no longer the dominant influential factor, and in fact, N_2 and CH_4 are more permeable across a porous boron nitride membrane compared to the smaller CO_2. The intermolecular chemical interactions that causes higher molecular concentrations around the membrane and superior adsorption-diffusion, becomes stronger than the steric effects, leading to higher overall gas fluxes through the membrane.

5.3.3 Adsorption and diffusion

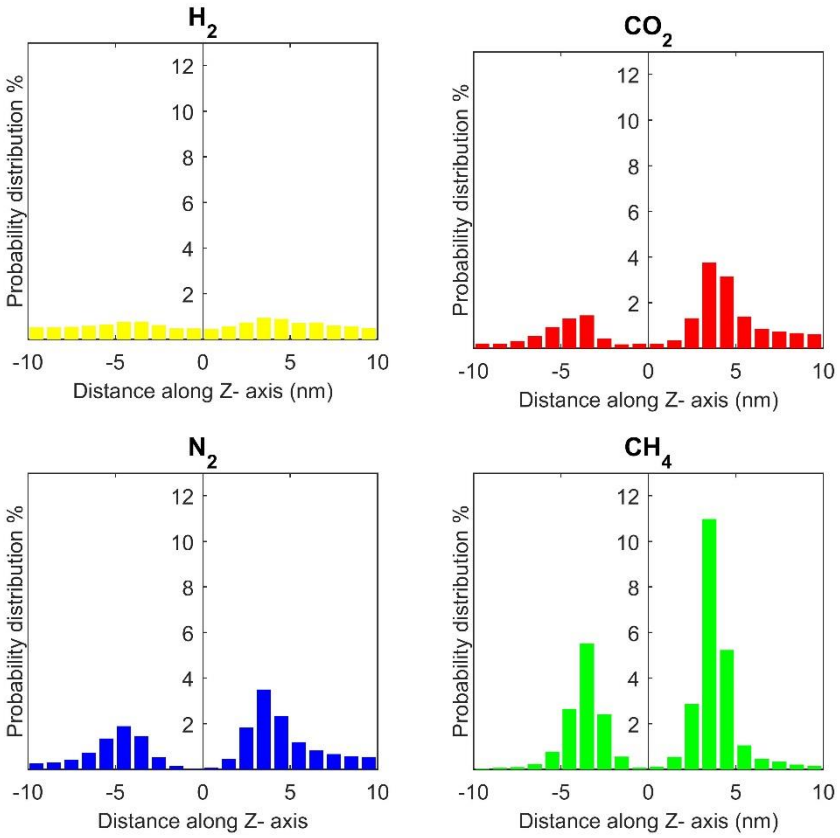

Figure 5.7: The probability distribution of the gases along the Z-direction perpendicular to the membrane. The figure shown here is the results from gas permeation study of pore-13-B under 5% biaxial strain.

Evaluation of the mean-distribution of gases along the z-axis shows that the gases assessed in this study adsorb on the boron nitride membrane to varying degrees. The variations of the probability distributions of each gas type from 1nm from the membrane in both directions, along the z-axis perpendicular to the membrane, are depicted in Figure 5.7. Clearly, the polar gas molecules show higher concentration around the boron nitride membrane, while the H_2 gas molecule shows the least interaction. This is due to the higher intermolecular interaction between these gas molecules and the membrane compared to H_2 which leads them to physically and/or chemically adsorb on the membrane. Given that the highest gas concentration is found between 0.3-0.4 nm from the boron nitride layer, it can be concluded that physical adsorption is more prevalent.

These trends for gas adsorption on hexagonal boron nitride agree with trends observed in previous studies by Sun et.al., [105] who studied the H_2, CO_2 and CH_4 adsorption on pristine boron nitride sheets and observed that CO_2 and CH_4 had a substantially higher adsorption energy compared to H_2. The stronger physisorption creates an adsorbed layer on the boron nitride membrane contributing to stronger flux across the porous layer. The higher concentration of CH_4 within the adsorbed layer leads to higher CH_4 permeation through the membrane compared to CO_2, despite having the larger molecular size.

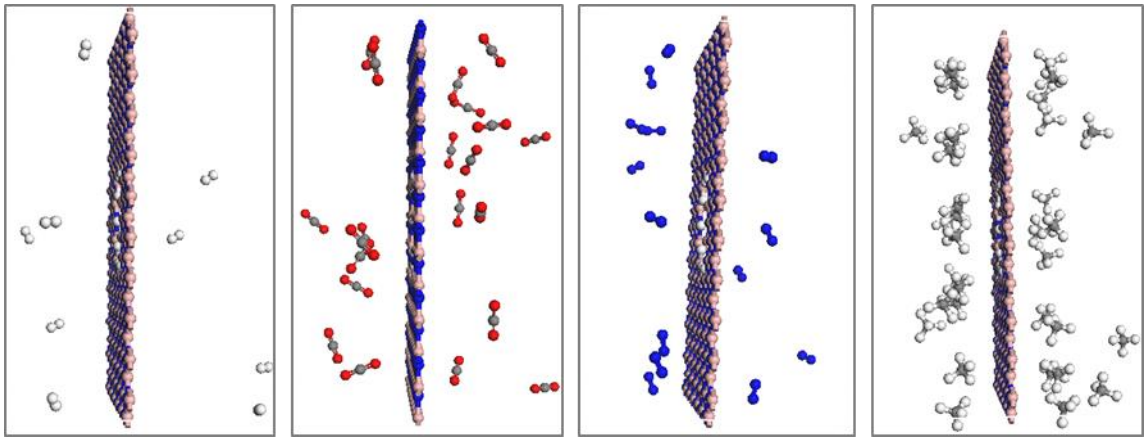

Figure 5.8: Snapshots of membrane and adsorption zones at the end of simulation for each gas type. The contrast in adsorptive behaviour is clearly visible. Atom colour code: hydrogen, white; boron, pink; carbon, grey; nitrogen, blue, red; oxygen.

Analysing the concentration of H_2 around the membrane shows that the concentration is only slightly higher compared to the other zones. Therefore, this confirms the H_2 permeation is predominantly due to the size sieving effects and the intermolecular interactions between the membrane and the gas molecules are negligible compared to other gases. On the other hand, as mentioned above, the differences in CO_2 and CH_4 permeation can be attributed to the differences in chemical affinity. However, the significantly lower permeation of CH_4, N_2 and CO_2 compared to H_2, which has the smallest chemical interactions with the membrane, establishes that there are still size effects hindering these three gases crossings through the membrane pore. The lower overall gas concentration on the negative side of the membrane is due to the fact, at the start of the simulation; the gas concentration on this side is zero and only starts to gradually increase when gas molecules start to permeate through the membrane.

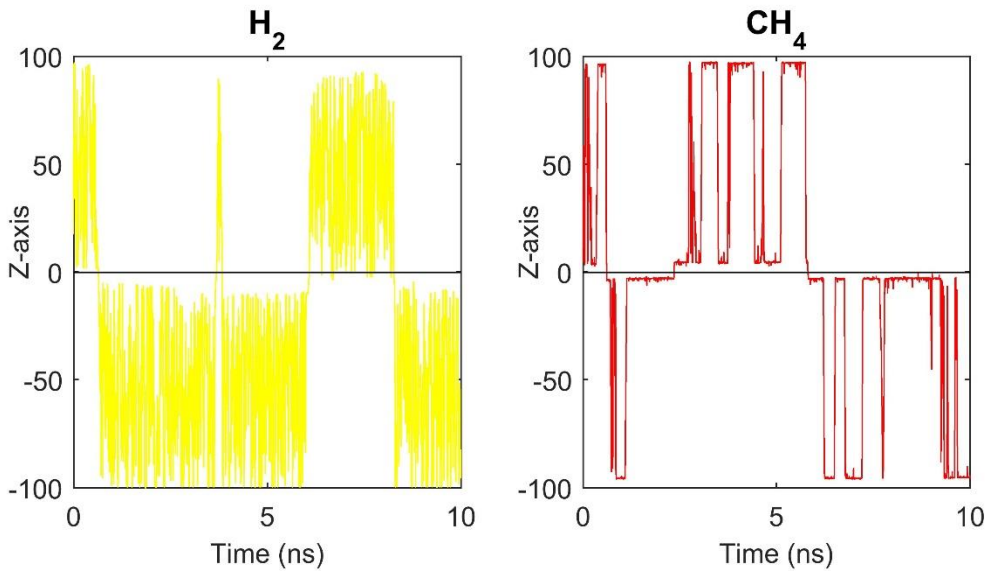

Figure 5.9: A typical molecular trajectory of H_2 and CH_4 respectively. The membrane is positioned at the centre where Z=0.

From the gas probability distribution with respect to the membrane, three zones with different characteristics can be identified. The region closest to the membrane has lower gas concentration due to being occupied by the membrane. This zone can be identified as the membrane zone. From here, the gas concentration increases and peaks within 0.3-0.4 nm and gradually declines to a constant value at about 0.7 nm from the membrane. Since the higher concentration within this zone is primarily due to gas adsorption, this zone can be termed as the adsorption zone. From 0.7 nm onwards, the gas concentration more or less remains a constant and the interactions between the membrane and gas molecules are almost non-existent beyond this point. Therefore, this zone will be named as the bulk zone.

Figure 5.9 represents a typical molecular trajectory of an H_2 and CH_4 gas molecule. Observing this trajectory and the gas concentration profiles we can identify three different possible paths a gas molecule can follow.

1. A gas molecule reaches the membrane and bounces back without crossing the membrane. This can be due to a number of reasons, such as the gas molecule's position with respect the pore, adsorption on the membrane, orientation with respect to the pore and the energy of the molecule not sufficient to overcome the energy barrier for the gas penetration through the membrane.

2. A gas molecule momentarily crosses through to the opposite side, but returns to the original side.
3. The gas molecule migrates from the bulk zone in one side to the bulk zone of the opposite side.

These patterns are consistent with observations by Sun et al [19]. For the analysis of this study, the definition of a crossing event recorded in Figure 5.6 and Table 5.2, is when a gas molecule actually crosses from the bulk zone on one side to the bulk zone on the other side. Examining the gas trajectories, it can be observed that a H_2 molecule, once it reaches the membrane, either would typically move back to the bulk zone on the same side or will cross to the opposite side of the membrane. This kind of crossing, where the gas molecule straightforwardly migrates from the bulk zone of one side to the bulk zone of the opposite side is classified as the direct flux. However, the CH_4 trajectory shows that once the gas molecule reaches the membrane, it either would directly cross to the bulk zone on the opposite side similar to a H_2 molecule, or would linger around the adsorption zone before crossing to the opposite side or moving back to the bulk zone of the same side. The reason for a gas molecule to remain closer to the membrane is due to the molecular adsorption on the membrane. When an adsorbed gas molecule crosses to the opposite side, it is known as surface flux. This phenomenon further confirms that the adsorptive interactions between the membrane and H_2 gas molecule is minimal and the diffusion process of CH_4 is aided by its intermolecular interactions with the membrane.

Figure 5.10 is a comparison of molecular-crossing events as defined above, from the bulk zone on one side to the bulk zone on opposite side (type 3 movement) and simply crossing the membrane from one side to another (sum of type 2 and 3) . For this analysis, the results of simulations carried out for CO_2 and CH_4 permeability through a pore-13-B membrane under 5% biaxial strain are chosen. The results show that type 3 crossings are about 60 ±3% of the total number of crossings (sum of type 2 and type 3 crossings).

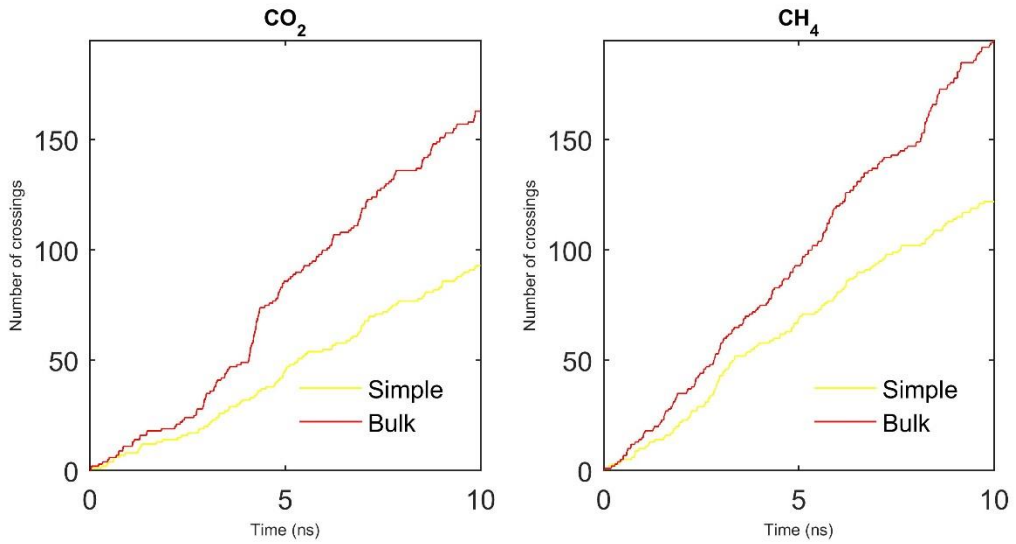

Figure 5.10: Comparison of simple crossing vs bulk crossings. Here a simple crossing is considered when a gas molecule simply crosses the membrane from one side to the opposite side, while bulk crossing represents when a gas molecule crosses from the bulk zone of one side to the bulk zone of the opposite side. The comparisons shown here are that of the CO_2 and CH_4 gas molecular permeation through a membrane with pore-13-B under 5% biaxial strain

$$\text{Gas flux} = \frac{\text{Number of crossings (mol)}}{\text{membrane area} \times \text{simulation time}} \qquad \text{Equation 5.1}$$

Table 5.3: Summary of calculated gas flux

	Strain (%)	Flux (×10⁴ mol/m².s)			
		H_2	CO_2	N_2	CH_4
Pore-10	0	0.00	0.00	0.00	0.00
	2.5	0.03	0.00	0.00	0.00
	5	0.05	0.00	0.00	0.00
Pore-13-B	0	0.03	0.00	0.00	0.00
	2.5	0.74	0.17	0.05	0.00
	5	1.20	0.21	0.26	0.28
Pore-13-N	0	0.12	0.00	0.00	0.00
	2.5	1.49	N/A		0.24
	5	0.00			

Interestingly when pore -13-B is under 5% strain and is sufficiently large to allow all the gas types to cross through, it becomes more permeable to CH_4 than N_2 and CO_2, even it has larger kinetic diameters than the latter gases. Furthermore, CO_2 has the lowest flux despite having the second smallest kinetic diameter out of the four gas types under study. Theses simulations were repeated twice to eliminate the statistical uncertainty given that differences in fluxes were less than 300mol/m^{2}s. In both simulations, the same trend was observed and the differences between fluxes remained the same. (Appendix A)

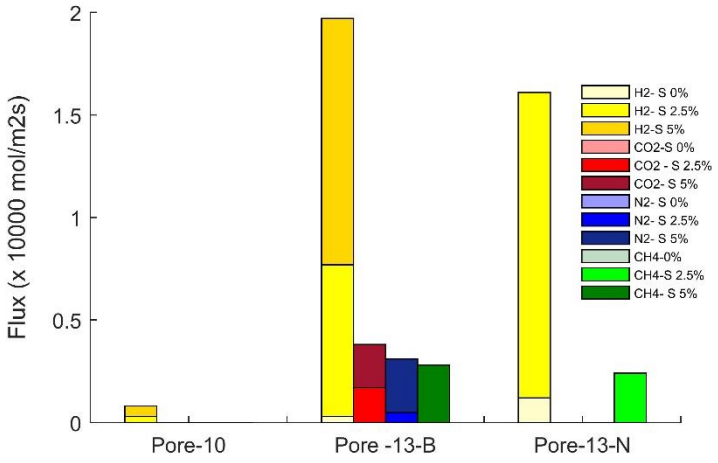

Figure 5.11: The summary of gas flux through the membrane

As aforementioned, the departure of correlation in flux rates, from the kinetic diameters of the gas molecules can be attributed to that, under 5% strain the pore opening becomes sufficiently large, and size-sieving properties are no longer the dominant factor. When the pore opening becomes large enough, the chemical interactions between the pore opening and the gas molecules have a significant contribution towards the gas permeability. The lower gas flux of CO_2 and the increased flux of CH_4 gas molecules in particular, can be attributed to the polar nature of these molecules. The attractive or repulsive interactions between the membrane and the gas molecules are heightened when the size effects of the pore become less apparent. The higher CH_4 flux compared to N_2 and CO_2, is due to the higher CH_4 concentration in the adsorption region and hence due to the added contribution of surface flux in addition to direct flux. CO_2 and N_2 permeation are also aided by surface flux, however not to the extent to that of CH_4. The reduced

CO_2 flux compared to N_2 and CH_4 could be due to the electrophilic nature of the CO_2 molecule. The positively charged hydrogen atoms at the pore-edge could retard the movement of the CO_2 molecule through the pore. The positivity or the negativity of the edge hydrogen atoms is determined by whether they are bonded to nitrogen atoms or boron atoms. Therefore, the edge-terminating hydrogen atoms have a mixture of positive and negative charges. The magnitude of the positively charged atoms is considerably higher compared to that of the negatively charged hydrogen atoms, however. Therefore, the repulsion effect of these atoms overall impedes CO_2 molecule diffusion through the pore opening.

5.3.4 Gas separation in binary systems

In this study, the permeability was assessed based on pure gas simulations, where in a simulation system only a single type of gas was studied. This gives a solid understanding of how the permeability of a certain gas type is affected by the changes in pore structure and dimensions. Furthermore, it gives insight into how the membrane interacts with a specific gas and how these interactions influence the gas permeability. However, in a real application of gas separation, the system would consist of two or more components. To evaluate how gas permeability characteristics deviate in the presence of other gaseous components, a sample simulation of a simulation system consisting of a binary-equimolar mixture was performed. For the sample simulation, the permeability characteristics of a mixture of H_2 and CO_2 through a membrane with pore-13-B under 2.5% biaxial strain were considered. In the binary simulation system, the initial feed pressure was matched with that of a pure-gas simulation system. Specifically, the number of gas molecules of each type was reduced by half (40 each) and the total number of gas molecules in the mixture was matched with that of pure-gas simulations (80 molecules).

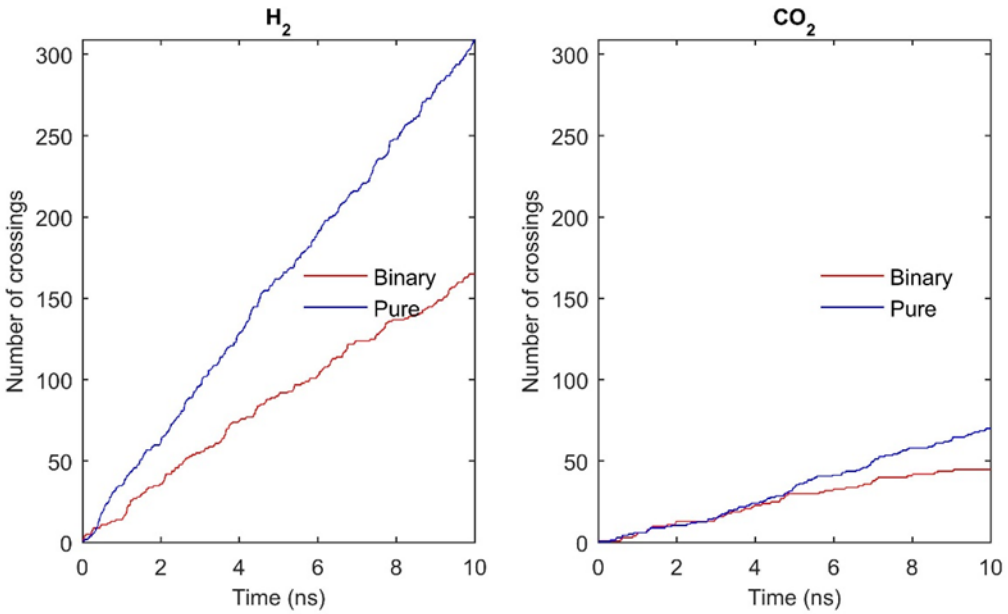

Figure 5.12: Comparison of gas permeation in pure gas simulation systems of H_2 and CO_2 with permeation in an equimolar mixture of the two gases

Next, the number of total crossings during the simulation for each gas type in the binary mixture was compared with the total crossings in the pure gas simulation study of each respective gas type. The comparison shows that the number of total crossings for each gas type is lower compared to that of the corresponding pure gas simulation results. However, it should be noted that for each gas type only half of the gas molecules from each type is present in the simulation box. The number of gas crossings in pure gas simulations is 310 and 71 for H_2 and CO_2 respectively. The total number of gas crossings in the binary system lies in between these two values at 210, which consists of 165 H_2 crossings and 45 CO_2 crossings. Considering the CO_2 permeability, the number of individual crossings is reduced by 37%. Similarly, the H_2 permeability is reduced by 47%. Bearing in mind, that in the binary simulation system only half of the gas molecules are in the gas feed, if the gas permeability is considered with respect to the partial gas pressure of the respective gas type in the feed, it can be observed that the gas permeability actually increases in the binary system especially for CO_2. However, the scale of the change in number of crossings for each gas type is different. For example, the increase in H_2 permeability is lower compared to that of CO_2. This is due to the higher concentration of CO_2

molecules around the membrane owing to the strong interatomic interactions between CO_2 and the membrane, and thereby blocking the H_2 molecules from reaching the pore opening.

In Figure 5.13 (a), the gas concentration variation is compared for each gas type in binary and pure gas permeation simulations. The analysis shows that the H_2 probability distribution is lower in the binary gas simulation system compared to the pure gas simulations, confirming our hypothesis of reduced H_2 concentrations due to CO_2 occupying this space.

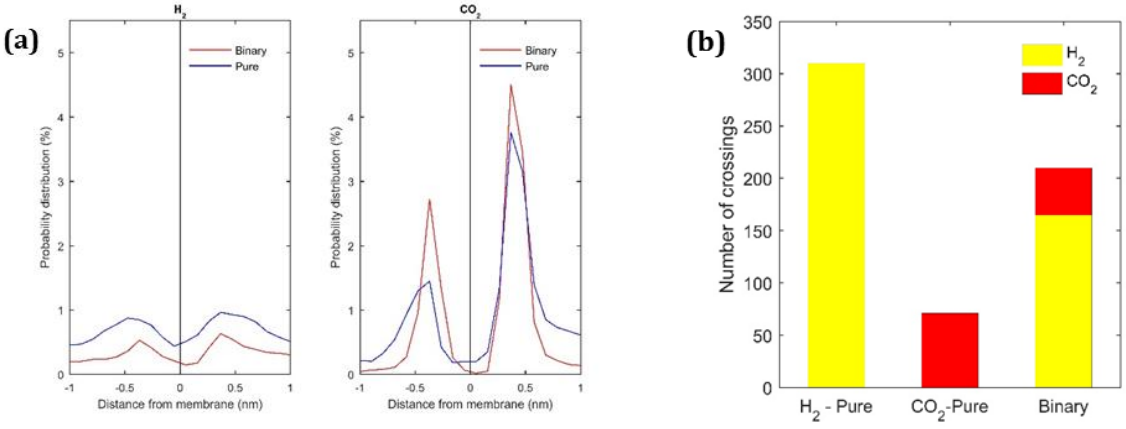

Figure 5.13: (a) The normalized probability distribution of gas molecules around the membrane area for H_2 and CO_2. The figure compares the concentration in pure gas simulation system with the binary gas simulation system. (b) The summary of number of crossings in each system for each gas.

Overall, the simulations show that the gas permeation characteristics remain essentially the same irrespective of the composition of the system. In binary systems, the gas type that shows stronger surface diffusion in a pure system can be expected to have an enhanced flux. The H_2/CO_2 selectivity in the binary simulation system is slightly reduced, compared to the selectivity calculated from pure gas simulations. The change in gas selectivity in binary feed mixtures compared to pure mixtures is mainly dependent on the level of selective adsorption of the individual gas type on the membrane. However, the permeability and diffusion patterns of the two types of simulations are comparable, showing that a pure-gas simulation can reasonably represent the gas diffusion behaviour through a membrane giving a good understanding of the underlying chemical and physical phenomena affecting the overall permeability.

5.4 SUMMARY

This study focused on the gas permeability of three structurally stable porous openings on hexagonal boron nitride membranes. The study shows that the pore-10, which is created by removing 10 atoms from the pristine monolayer, is impermeable to any type of gas under evaluation. The results, however demonstrates this porous structure can be strain-tuned by subjecting it to biaxial strains of 2.5% and 5%, making the membrane permeable to H_2 gas molecules. Furthermore, the fact that the strained membrane maintains its inherent impermeability to the other gas types studied: CO_2, N_2 and CH_4, makes the strained membrane, a suitable candidate for H_2 purification from gas mixtures containing the aforementioned gas types.

The 13-B and 13-N pores, which are reasonably larger than pore-10, even under fully relaxed conditions, are selectively permeable to only H_2 gas molecules. This makes these two types of pores suitable for H_2 purification from mixtures of CO_2 and/or CH_4 mixtures. Out of these two opening types, the pore-13-N, which has a larger effective pore area, predictably has a higher H_2 flux, making it the preferred pore structure for H_2 purification. When these two types of pores are subjected to biaxial strains, the larger pore with a larger opening: pore-13-N loses its ability to transport H_2 only and becomes permeable to the other gases studied in this analysis. Meanwhile, the pore-13-B under 2.5% biaxial strain expands sufficiently, to allow CO_2 passage through the membrane. The pore-13-B membrane, due to its selective H_2 and CO_2 permeability, is an ideal membrane for H_2/CH_4, CO_2/N_2 and CO_2/CH_4 purification. This membrane under 5% biaxial strain becomes permeable to all the gases studied. The permeability behaviour of each gas molecule type through the 13-B opening under 5% biaxial strain is used to analyse the intermolecular interactions between the gas molecules and the porous boron nitride membrane and to explain how such characteristics affect the gas permeability and selectivity.

CHAPTER 6 STRAINED GRAPHITIC CARBON NITRIDE FOR HYDROGEN PURIFICATION

This chapter details the theoretical studies on H_2 purification using g-C_3N_4 membranes. A combination of first-principles DFT calculations and non-equilibrium MD simulations is used to study the gas permeability through a g-C_3N_4 membrane. In this study, two different approaches; variation of feed pressure and strain tuning were used to improve the separation efficiency of the membrane. The simulation approach is given in section 6.2 and the results and discussion are presented in section 6.3.

6.1 INTRODUCTION

The demand for cleaner energy has incited greater interest in hydrogen energy as it offers a superior alternative to conventional fossil fuel combustion, thanks to its high energy density [4], higher energy conversion efficiency and its environmental friendly nature [5]. Current H_2 production methods include, steam-methane reforming, coal gasification and water-electrolysis [6]. Irrespective of the production method, a critical step common to every production method is a hydrogen purification step from a mixture of gases.

Two-dimensional C_3N_4 is a graphene-like carbon nitride material that has attracted the interest of the scientific community due to its interesting chemical and photocatalytic properties, and excellent thermal properties [78, 80]. It is the most stable compound of the carbon nitride family, and consists of tri-s-triazine building blocks [171]. Another advantage of this material is its facile synthesis, which has been discussed in previous chapters.

Here we study the use of g-C_3N_4 for gas separation applications using first-principles and molecular dynamics approaches. Our study evaluates the permeability of small gas molecules: H_2, CO_2 and CH_4, across a g-C_3N_4 membrane. In this study, we primarily focus on the possibility of improving the gas permeability of the g-C_3N_4 membrane, by subjecting it to small biaxial strains. The findings of this study may find applications in H_2 separation from CO_2 and CH_4, in refinery waste recovery, H_2 purification and pre combustion CO_2 separation.

6.2 COMPUTATIONAL DETAILS

Molecular dynamics simulations were used to analyse the H_2, CO_2 and CH_4 permeation across the membrane, and first-principles DFT calculations were used for geometry optimization of g-C_3N_4 and potential energy scan (PES) for H_2 passage under various strained conditions.

6.2.1 First-principles quantum mechanical simulations

All DFT calculations were carried out using the DMol3 module in Materials Studio [144, 145]. First, the g-C_3N_4 supercell was fully relaxed, allowing the relaxation of both atomic positions and the lattice parameters. For subsequent geometry relaxations under induced strain, the strain was added by increasing the fixed unit-cell dimensions by 2.5, 5 and 7.5%, with the atomic positions allowed to relax. The potential energy barrier for the H_2 molecules crossing through a monolayer was simulated by analysing the gas passage through the centre of the pore of a 3×3 g-C_3N_4 periodic system based on transition state theory.

The generalized gradient approximation treated by the Perdew-Burke-Ernzerhof exchange corelation [135] with a basis set of all electron double numerical plus polarization (DNP) was used for DFT calculations. The DFT-D method developed by Grimme et al. [169], was used for the long-range van der Waals corrections. For geometry optimization calculations, a 2×2 cell, with a vacuum slab of 10 Å between sheets, was chosen, and the Brillouin zone was sampled by 3×3×1 k-points using the Monkhorst-Pack scheme [170]. The atomic charges were calculated using the Mulliken charge analysis [161]. The settings and parameters for the DFT calculations are given below.

Energy	:	1.0×10^{-5} Ha
Energy maximum force	:	2×10^{-3} Ha/Å
Energy maximum displacement	:	5×10^{-3} Å
Maximum iterations	:	50
Self-Consistent field tolerance	:	1.0×10^{6}
Maximum step size	:	0.3 Å
Maximum SCF cycles	:	50
Multipolar expansion	:	Hexadecapole

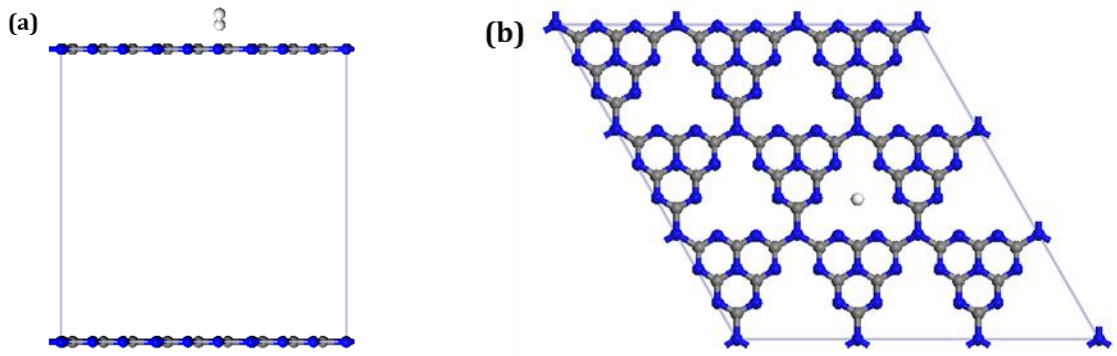

Figure 6.1: The simulation setting for TS search calculations (a) Side view, (b) Top view. Atom colour code: white, hydrogen; grey, carbon; blue, nitrogen

For Transition State theory calculations, a 3×3 cell with a 20 Å vacuum slab was used with a 7×7×1 k-point grid. The gas molecule was placed perpendicular to the membrane at a distance away from the membrane plane positioned such that, the geometric centre of the pore and the central axis of the gas molecule coincide as shown in Figure 6.1. First, DFT calculations were carried out to obtain the physisorbed conformations of the gas molecule on both sides of the membrane. Next, transition state theory calculations were performed to obtain the minimum energy pathway of a gas molecule crossing through the membrane, using complete linear and quadratic synchronous method with conjugated gradient refinements [172, 173]. The calculations were carried out with a convergence tolerance of 2×10^{-5} Ha for energy, 4×10^{-3} Ha/Å for gradient and 0.005 Å for displacement. In these calculations, similar to the geometry optimization simulations, the lattice

constraints were maintained to mimic applied strains, while the atomic positions of the membrane or the gas molecule were not constrained to maximize the accuracy of the simulation results.

6.2.2 Molecular dynamics simulations

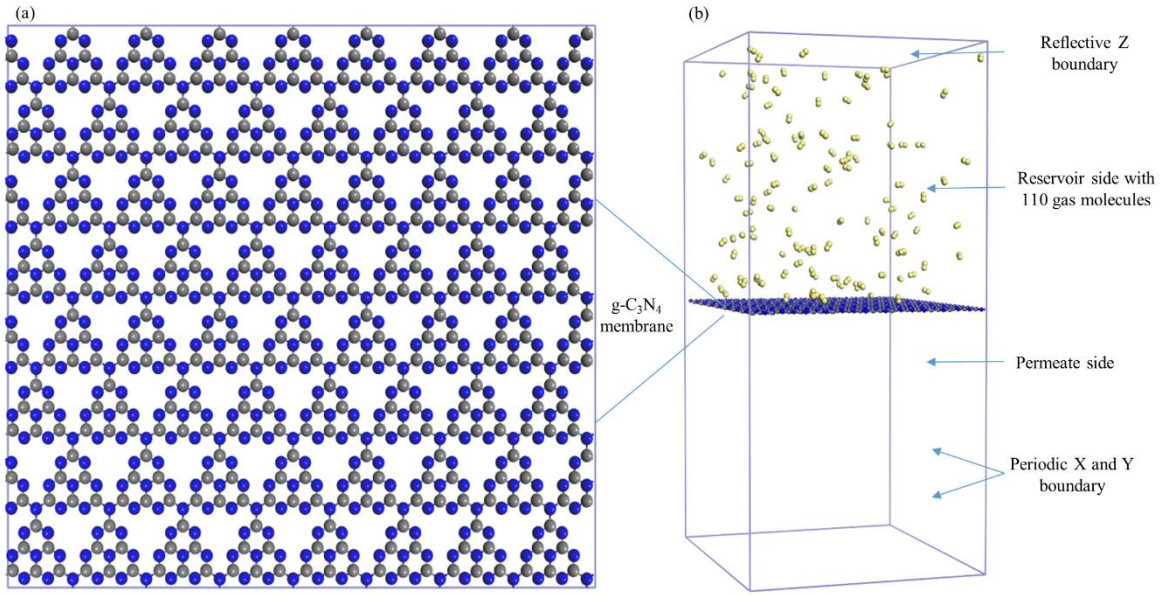

Figure 6.2: (a) Top view of the 5x5 nm, g-C_3N_4 membrane. (b) Illustration of simulations model. Atom colour code: grey, carbon; blue, nitrogen; yellow, hydrogen

As shown in Figure 6.2, a frozen 6×6 monolayer of g-C_3N_4 (approximately ~ 5.5×5.0 nm), obtained from DFT geometry optimizations, was placed at the middle of the simulation box. Initially 110 gas molecules were placed in one side of the membrane, which behaves as the gas reservoir. The simulation system has periodic boundary conditions applied in the x and y-directions and reflective boundary conditions in the z-direction. The height of the box was varied to achieve various feed pressures. All MD simulations were performed using the LAMMPS package [159]. Simulations were carried in the NVT ensemble, with Nosé-Hoover thermostat to maintain the system temperature at 298 K. Each simulation was carried out for a total time period of 10 ns with a time-step of 0.4 fs and the output data were recorded every 200 fs. The Reax potential developed by Mattson et al. for general purpose hydrocarbon parameterization was used to model the interatomic interactions [174].

6.3 RESULTS & DISCUSSION

6.3.1 Structural simulation results

Using first-principles simulations, first a fully optimized structure of g-C_3N_4 was obtained. This optimization is done without lattice constraints and therefore is considered to have no external stresses acting upon the structure. The Figure 6.3 is a fully relaxed 2×2 unit cell of the C_3N_4 structure, with a lattice dimension of 14.2746 Å (the dimension of a single unit cell is half of this value) and angle of 60°. The pore opening has a point to point to distance of 4.77Å. This area, formed by equally spaced six nitrogen atoms with equal charges, is the effective pore opening and the dimensions of this area is the critical parameter for size exclusion sieving. The geometric pore diameter of the structure can be approximated as 3.1 Å. This value is slightly larger than the kinetic diameter of a H_2 gas molecule, while it is smaller than the other three types of gases.

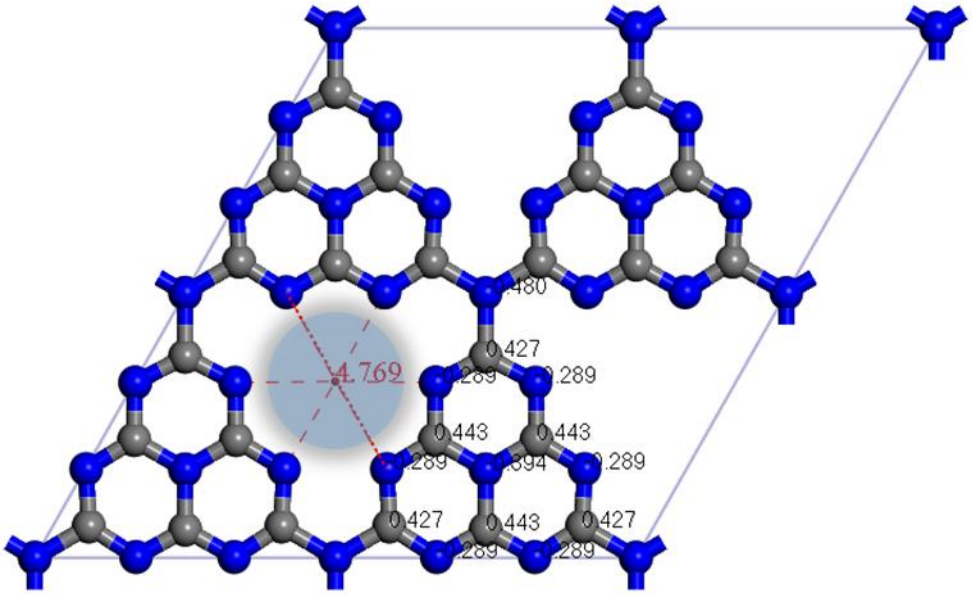

Figure 6.3: Depiction of structural properties and charge distribution obtained from DFT simulations

The critical bond lengths are summarized in the first row of Table 6.1. These observed values are in agreement with previously reported values [79]. The charge distribution on each molecule obtained from Mulliken charge analysis is shown in the figure. Compared to graphene, which has a zero charge in each atom, the carbon atoms of the g-C_3N_4 structure have a positive charge while the nitrogen atoms have a negative charge.

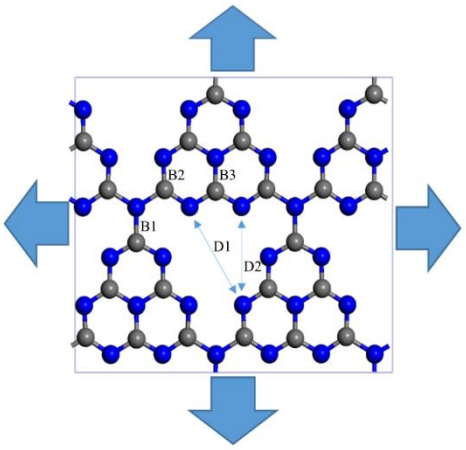

Figure 6.4: 2x2 supercell of g-C_3N_4. The bonds and distances are labelled. Atom colour code: grey, carbon; blue, nitrogen

Table 6.1: Effect of biaxial strain on g-C_3N_4 structure

Strain		B1	B2	B3	D1	D2
0.0 %	Length (Å)	1.48	1.33	1.40	4.77	4.13
2.5 %	Length (Å)	1.53	1.35	1.41	4.94	4.28
	Increase %	3.45	1.58	1.00	3.5	3.51
5.0 %	Length (Å)	1.57	1.38	1.43	5.08	4.40
	Increase %	6.50	3.46	2.65	6.48	6.49
7.5 %	Length (Å)	1.72	1.41	1.46	5.21	4.51
	Increase %	9.40	5.63	4.66	9.25	9.25

Next, the behaviour of the structure under applied biaxial strains was analysed. The structural changes induced by applied 2.5, 5 and 7.5% strain values are summarized and compared against the unstrained cell, in Table 6.1. The results signify that the change of molecular structure is not directly proportional to the increase of cell dimensions. The stronger aromatic bonds B2 and B3 within the hexagonal rings demonstrate higher resistance to stretching compared to the B1 bond outside the ring. Similarly, the percentage increase of the porous area of the monolayer (D1 and D2) exceeds the strain magnitudes due to the absence of interatomic bonds of an aromatic ring, resisting enlargement. Therefore, a 2.5% strain, which will cause an approximately 5% increase of the total membrane area, will in fact increase the porous area by approximately 7%. Similarly, a 5% biaxial strain will increase the pore area by 10%, while the total membrane area is only increased by 7%. For the subsequent study of the H_2 flux across a g-C_3N_4 by strain tuning, only the two membranes subjected to 2.5 and 5% biaxial strain were considered, since these results show that a 7.5% biaxial strain, increases the C-N bond outside the aromatic ring to 1.7 Å. This would lead to a bond weakening at this site and therefore, for the gas permeation study the membrane under 7.5% biaxial strain was excluded.

6.3.2 Gas Permeation Results – MD Simulations

The gas permeability of the membrane was studied using non-equilibrium molecular dynamics simulations. A sample of the temperature and energy variation during the production step of the simulation is given in Figure 6.5. In this figure, the simulation results for H_2 permeation through a C_3N_4 under 2.5% biaxial strain are used. The results confirm the simulation system is well equilibrated to a temperature of 298 K at the start of the production step, justifying the time period chosen for the equilibration part is a suitable choice for the thermostat.

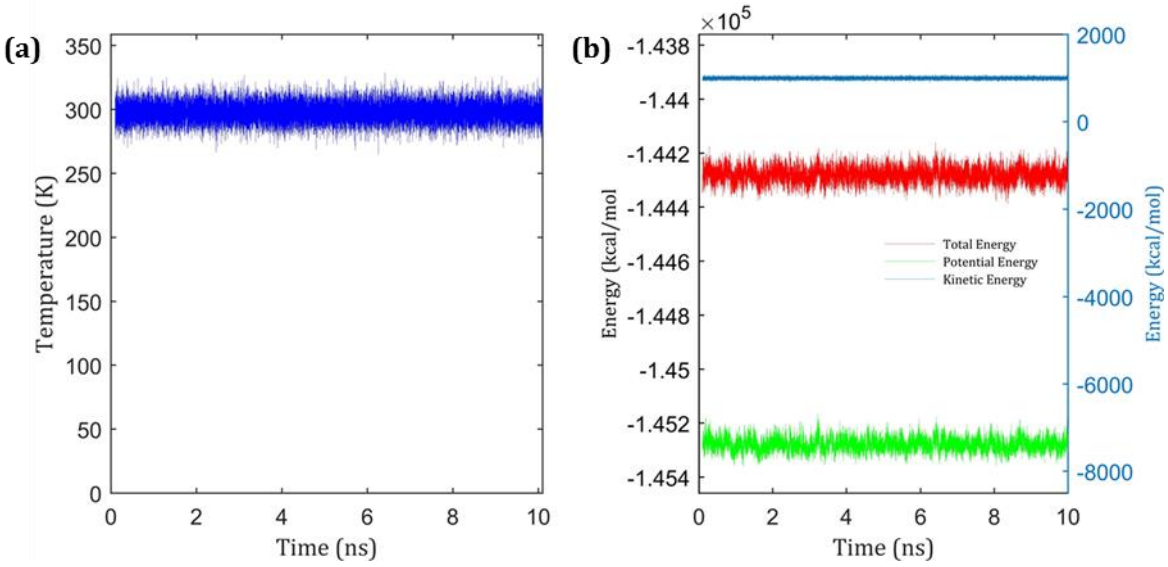

Figure 6.5: (a) Temperature and (b) energy variation during the production part of the simulation. The kinetic energy in (b) is scaled in y-axis on the right side, while total energy and potential energy are represented on the y-axis on the left hand side.

6.3.2.1 Effects on feed side pressure with gas permeation

First question addressed in our assessment was the gas permeability of graphitic carbon nitride under unconstrained conditions. The permeance of the g-C_3N_4 monolayer was evaluated by observing the gas concentration on the permeate side of the simulation box, at the end of the 10ns simulation period. Our studies show, only H_2 molecules with the smallest kinetic diameter of 2.76 Å are permeable across the g-C_3N_4 pores, while CO_2 and CH_4 with kinetic diameters: 3.3 and 3.8 Å, respectively, had zero crossings even at the highest pressure investigated.

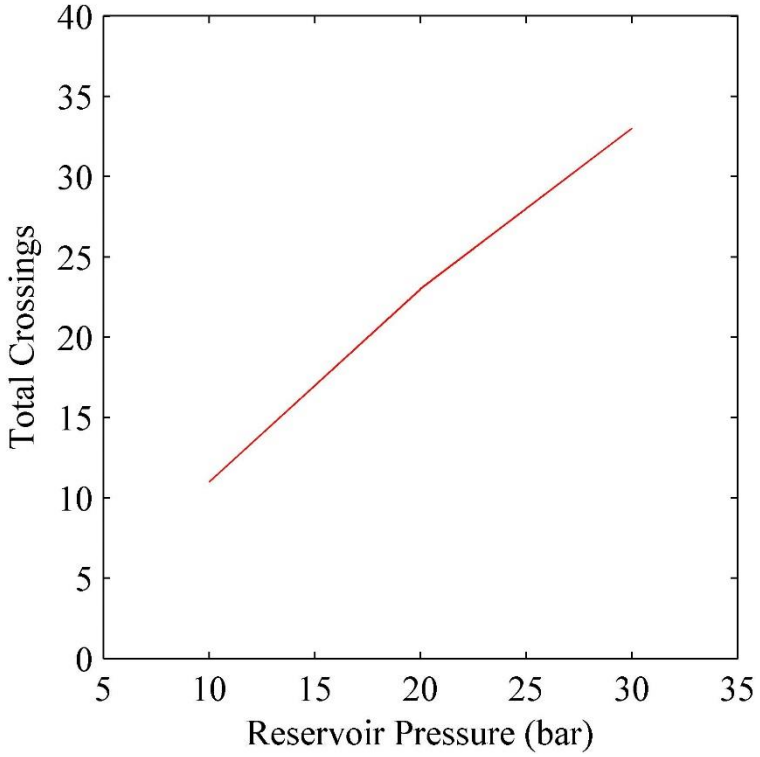

Figure 6.6: Variation of total number of crossings at the end of 10 ns simulation time, with the reservoir pressure

To investigate how gas permeance can be improved with feed side pressure, the simulations were carried at 10, 20 and 30 bar loadings, where the various feed pressures were achieved by altering the simulation box height. Here, feed side pressure means the initial pressure on the feed side at the beginning of the simulation. Figure 6.6 summarizes how H_2 permeability increases linearly with the initial feed side pressure. However, even at the highest feed pressure, only a few H_2 molecules cross the membrane indicating a weak H_2 flux across the unstrained membrane. Therefore, despite the perfect selectivity of H_2 over CO_2 and CH_4, in the absence of strain, g-C_3N_4 does not possess sufficient permeability to be considered a technically viable choice.

6.3.2.2 Gas permeability with strain tuning

Next, we explored the possibility of improving the hydrogen permeability, through strain induced pore enlargement. The study investigated gas permeation across g-C_3N_4 subjected to 2.5 and 5% biaxial strains at 10 bar initial pressure. Figure 6.7 (a) compares the fraction of gas molecules on the permeate side within a simulation system, for membranes under 0, 2.5 and 5% biaxial strains. Interestingly our findings reveal that even under a 5% strain, the membrane pores remain

impermeable to CO_2 and CH_4. We also tested the membrane under 5% biaxial strain for CO_2 and CH_4 at 30 bar, and found that even at a moderately high pressure, zero crossings occur across the membrane. However, under strain, the permeability of g-C_3N for hydrogen gas improves remarkably. The pore expansion induced by 5% biaxial strain results in the system reaching equilibrium (equal number of gas atoms on either side of the membrane where the molecular fraction on each side approximately equates to 0.5) in less than 1 ns. Similarly, the system under 2.5% strain achieves this during the 10ns simulation while the unstrained membrane, even at the highest studied pressure, fails to reach equilibrium.

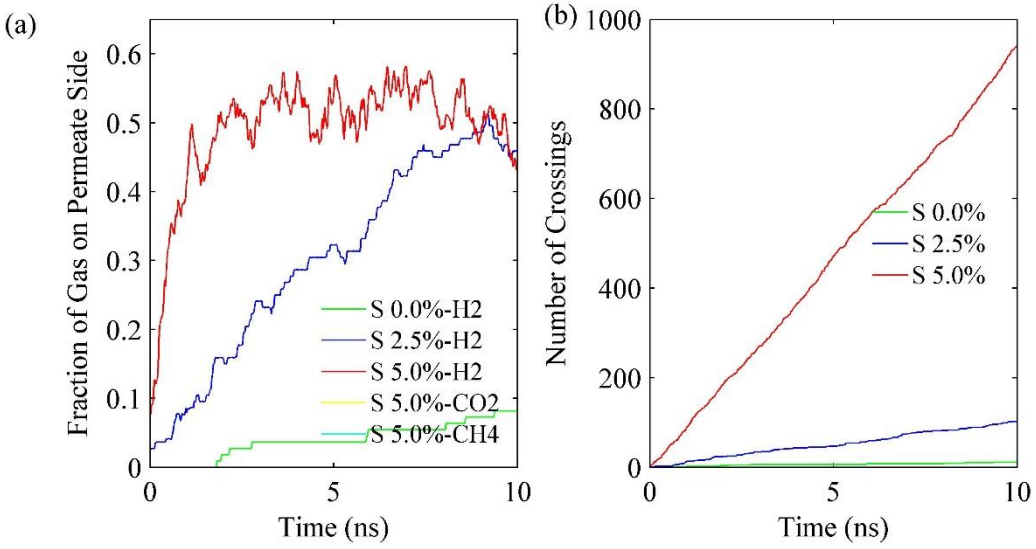

Figure 6.7: (a) Variation of fraction of gas molecules on the permeate side with time, the concentration remains zero for CO_2 and CH_4 (b) The number of H_2 crossings events through the membrane in both directions vs time

To estimate the actual gas flux, we analysed the gas crossings through each membrane in either directions, using the gas trajectories collected every 200 fs during the simulation time. Similar to previous chapters, a crossing event was considered when a gas molecule travels from the bulk zone on one side to the bulk zone on the opposite side. Figure 6.7 (b) compares the cumulative H_2 crossings in both directions, for each membrane system, versus time. The gas flux was calculated using Equation 6.1 in mols/m^2s. Our results indicate that the system under 2.5% strain, sees the flux increase to about 57.64 from the 6.47 mols/m^2s flux of the unstrained system, while the 5% strain increased the flux to 501.8 mols/m^2s. This implies that for each increase in 2.5% of strain the gas flux increases by approximately 9 times. The Figure 6.9 graphically summarizes the

calculated flux values for H_2 under various initial feed side pressure values and the effect of strain on the H_2 permeability of the membrane.

$$\text{Gas Flux} = \frac{\text{Number of crossings (mol)}}{\text{Membrane area} \times \text{Time}} \qquad \text{Equation 6.1}$$

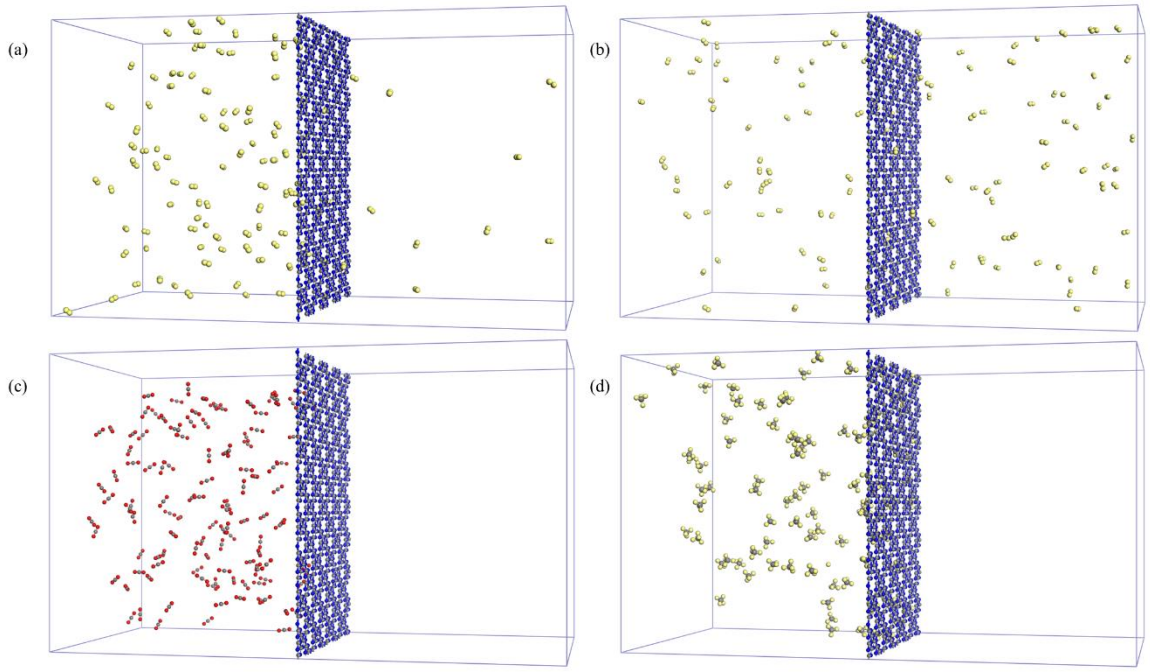

Figure 6.8: Illustrative snapshots of the system at the end of the 10 ns MD simulations for (a) unstrained system with H_2. System under 5% strain with (b) H_2, (c) CO_2 and (d) CH_4. The results indicate how even under a 5% strain the g-C_3N_4 membrane is impermeable to CO_2 & CH_4, and the significant improvement of the H_2 permeability under strained conditions in comparison to the unstrained membrane. Atom colour code: grey, carbon; blue, nitrogen; yellow, hydrogen; red, oxygen.

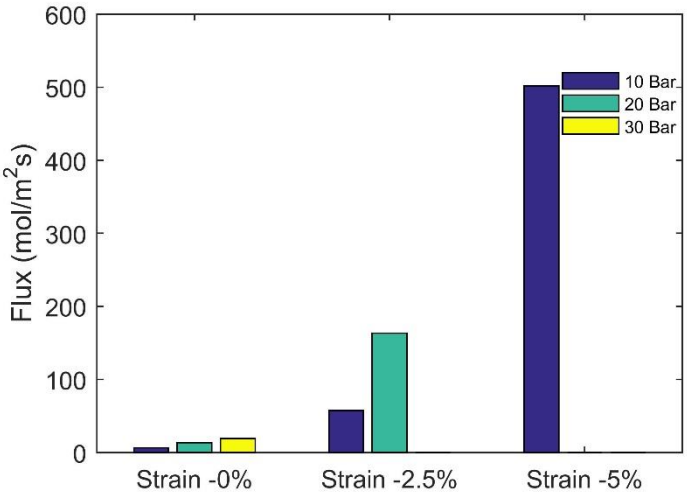

Figure 6.9: Summary of variation of H_2 flux with alterations to the feed side pressure and membrane strain

6.3.2.3 Justification of the chosen time step

For these simulations, a time-step of 0.4 fs was chosen, to balance the large simulation resources needed for REAX force field and the accuracy of the results. However, simulations with reactive force fields require sufficiently small integration time-steps to ensure the system remains stable during the simulation period. The REAX user-manual states that for simulations between 0-1500 K, a time-step up to 0.5 fs can retain reasonable energy conservation [175]. The chosen time-step of 0.4 fs is close to the upper limit of the recommended integration time-step. Therefore, to confirm the chosen time step is capable of producing quality results, a sample simulation was performed with a 0.1 fs time-step for 2.5 ns to study the H_2 permeability of a membrane under 2.5% strain. To reduce the statistical uncertainty associated with a lower number of overall crossings within the 2.5ns period, the simulations were carried out for a system under 30 bar initial feed side pressure, which will ensure a reasonable number of crossings during this period and will reduce probabilistic errors. Figure 6.10 compares the results from simulations on the sample system with 0.1 fs and 0.4 fs, where every simulation setting and initial conditions are identical. The figure shows that the simulation results with the two different integration time-steps are in good agreement with each other. Therefore, given that reducing the time-step does not affect the outcome of the simulation, and the temperature and energy of simulations with 0.4

fs time-step are appropriately in equilibrium, the use of 0.4 fs is justifiable for these simulations, while reducing the demand for computational resources.

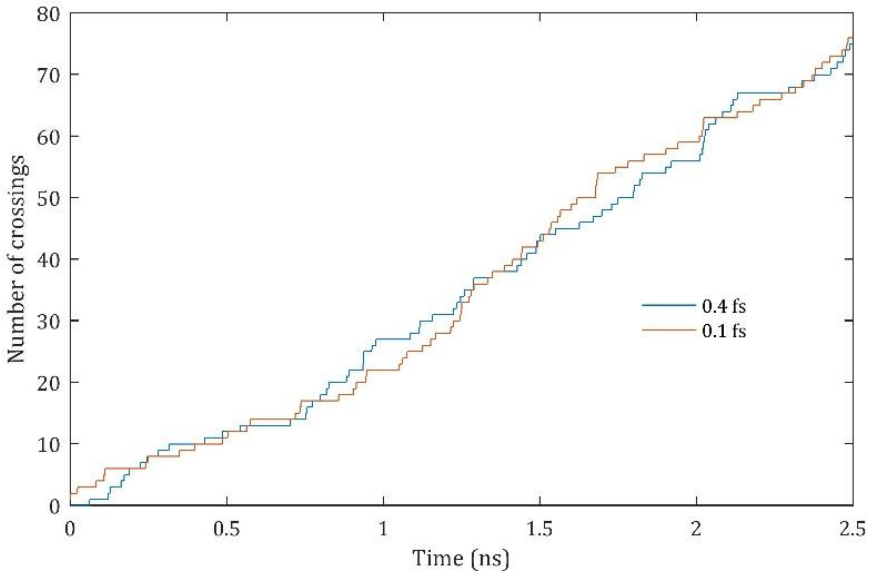

Figure 6.10: Comparison of number of crossings occurred during the first 2.5 ns of simulations carried out using a 0.4 fs time step with simulations using a 0.1 fs time step

However, these flux values are calculated based on the number of H_2 crossings from bulk zone to other bulk zone of the membrane. Figure 6.11 (a) compares the difference in gas flux calculated based on bulk-zone to bulk-zone (Type I as shown in Figure 6.11 (b)) with the flux calculated based on simply transferring from one side to the opposite side (sum of Type I and Type II). The results show the difference in two types is approximately 32% for simulations with a 0.1 fs time-step, while for simulations with a 0.4 fs time-step is only around 6%. The reason for the large discrepancy in gas flux values calculated based on two methods, for simulations carried out using 0.1 fs, can be attributed to the interval between which the outputs are recorded. Further elaborating on this, the coordinates of the gas atoms are written at a certain time interval, and based on these trajectories the number of crossings are calculated. For simulation with a 0.4 ns time-step, the output values are recorded every 200 fs, while the results of simulations with a 0.1 ns time-step, were dumped every 50 fs.

Therefore, the large discrepancies in the type I and type II gas crossings in simulations with a smaller time-step are due to the ultra-sensitivity of the output results. With atomic trajectories

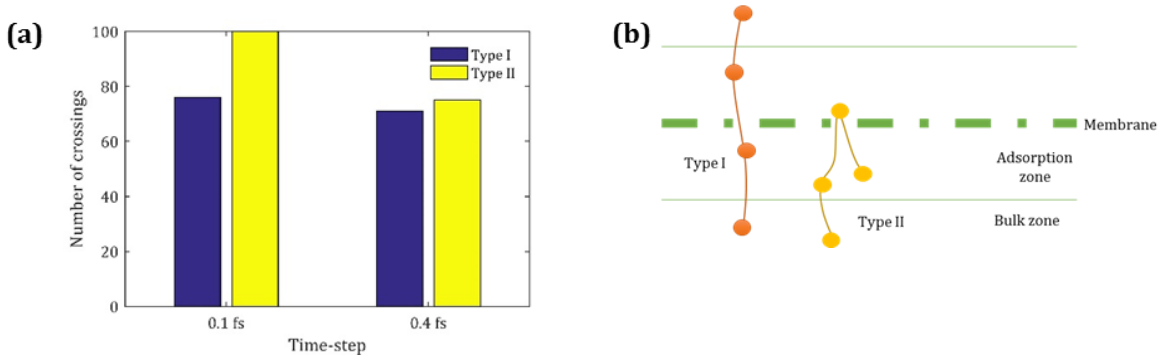

Figure 6.11: (a) Comparison of variation of gas permeability calculated based on Type I and Type II crossings. (b) Graphical illustration of Type I and II crossings

recorded at every 50 fs, the result analysis calculations can detect the faintest difference in gas molecular movement. Consequently, the post processing can identify when a gas molecule/atom moves to the opposite side even for a miniscule time period. Therefore, reducing the time interval between two output files would have increased the sensitivity of the results. However, since the actual gas flux is calculated based on type-I movements, i.e. a gas moves from bulk-zone to the bulk-zone of the opposite side, this level of high sensitivity to gas molecules' movement is nonessential for the simulation final results. This was confirmed by comparing the results analysed with output data every 50 fs, and analysing trajectories every 200 fs, of simulation results from 0.1 fs simulations.

As shown in Figure 6.12, there is a reasonable difference in type-II crossings between the two simulations, where the time-intervals between two trajectories used in data post-processing are different. The type–I permeation behaviours, however are identical. Considering the balance of accuracy of the simulation results and the management of computational resources and the time taken to handle large volumes of data, especially in post processing, the time interval of 200 fs chosen to record the molecular trajectories, is sufficient.

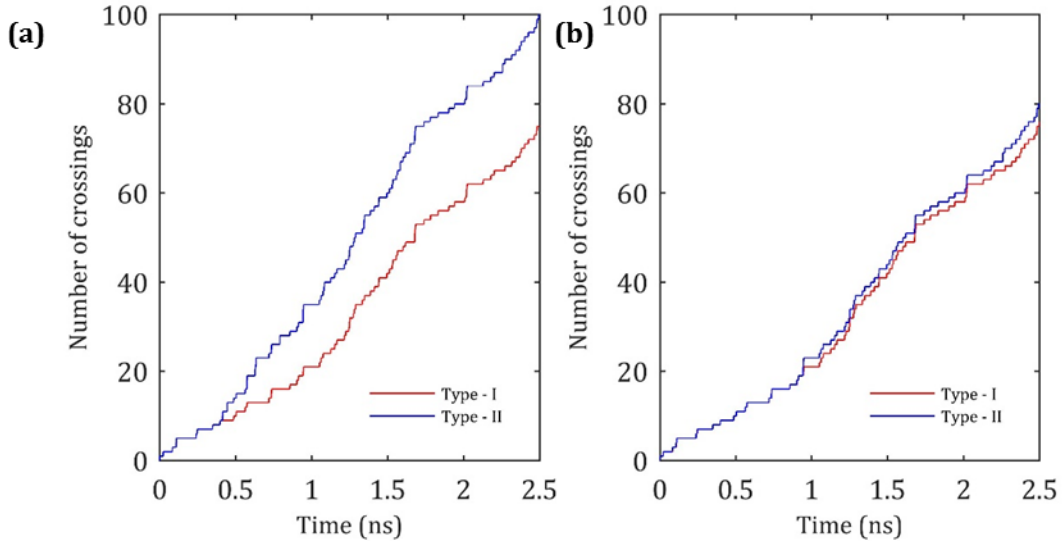

Figure 6.12: The comparison of data analysed from trajectories obtained (a) every 50 fs and (b) every 200 fs.

6.3.3 Gas Permeation Results – DFT Simulations

To further confirm our results, we performed first-principles DFT simulations to calculate the energy barrier for H_2 diffusion through the membrane. The energy adsorption/barrier was calculated as shown in Equation 6.2.

$$E = E_{system} - (E_{membrane} + E_{H_2}) \qquad \text{Equation 6.2}$$

Where E_{system}, $E_{membrane}$ and E_{H_2} represent the total energy of the system with the gas molecule adsorbed on the membrane or passing through the membrane, the ground state energy of the membrane and the energy of an isolated hydrogen gas molecule, respectively.

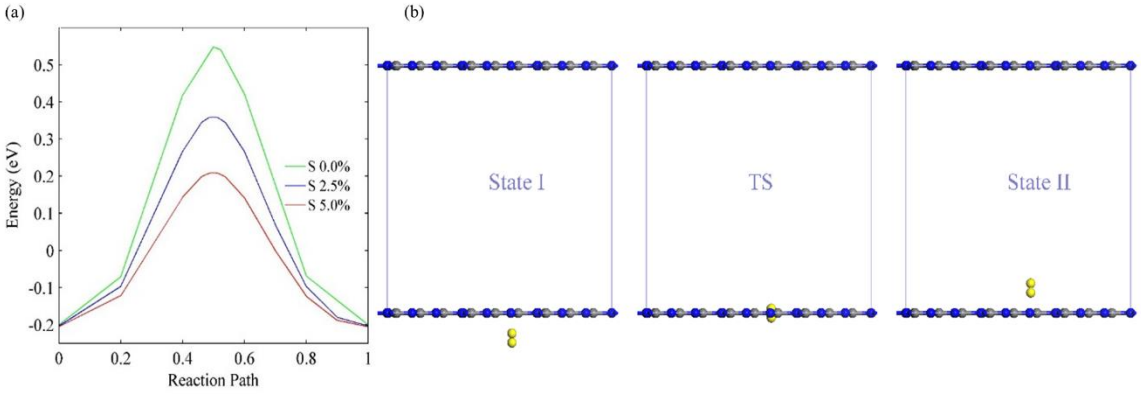

Figure 6.13: (a) The energy variation along the gas transport pathway, (b) Snapshots of H_2 physisorbed at state I transition state (TS) and state II. Atom colour code: grey, carbon; blue, nitrogen; yellow, hydrogen

Figure 6.13 shows the results of the DFT simulation studies. The reaction pathway was scanned from state I to state II. State I and II have a H_2 molecule physisorbed on the g-C_3N_4 membrane making a right angle with the membrane in nearly equal distances from either side of the membrane. This configuration has the lowest energy, and hence it is the most stable. At this configuration, the H_2 molecule is weakly physisorbed with a physisorption energy of 4.6 kcal/mol, on the membrane at a distance of 1.7 Å above/below the membrane plane. The transition state, where the geometric centre of the H_2 molecule is in the same plane as the membrane, has the highest energy due to the interatomic repulsions. The potential energy scans from state I to state II show that the energy barrier for H_2 passage decreases from 0.55 eV to, 0.36 and 0.20 eV when the membrane is subjected to 2.5 and 5% biaxial strain, respectively. The significant decrease in the energy barrier explains the substantial improvement of gas permeance across the membrane under strain, due to reduced steric hindrance.

Comparing the energy barrier for H_2 diffusion with the theoretical g-C_3N_3 (0.33 eV) reported by Ma et al. [29], our results show that under neutral conditions, g-C_3N_4 in fact has a higher energy barrier of 0.55eV, which is consistent with the observations of Ji et al. [176]. While the g-C_3N_3 membrane is, somewhat structurally similar to the g-C_3N_4 membrane, the larger pore opening diameter of 5.46 Å compared to the 4.77 Å of the latter reduces the energy barrier required to overcome in order to diffuse through the membrane. However, through strain tuning we were able to reduce the barrier for H_2 penetration to a 0.2 eV, which favourably contributes towards an increased gas flux. Given that g-C_3N_4 is the most stable graphitic carbon nitride compound and has been successfully synthesised this result shows the suitability of the use of this membrane.

Finally, our combined MD and DFT simulations show how a g-C_3N_4 membrane can be strain-tuned to possess superior H_2 permeability. Analysing the molecular trajectories of H_2, CO_2 and CH_4, we can conclude the size sieving effects of the pore opening, where steric effects hinders the diffusion of the larger CO_2 and CH_4 gas molecules, makes this material a highly selective membrane towards H_2 gas molecules. Conversely, the enlargement of the pore opening due to induced strain, leads to reduced steric repulsions between the nitrogen atoms at the pore edge and the hydrogen gas

molecules, which causes the reduced energy barrier and increased flux. Especially, given that the strain tuning does not affect the selective H_2 diffusion over CO_2 and CH_4 even in a high-pressure environment, the g-C_3N_4 membranes can find applications in pre-combustion carbon capture and hydrogen production from coal gasification.

6.4 CONCLUSION

In conclusion, gas selectivity and high permeability are the two dominant factors defining the effective performance of a gas separation membrane. Our combined classical MD simulation and first-principles DFT simulation results provide an accurate trend of gas selectivity and a reasonable approximation for the gas flux across a membrane. Our findings show that with minor mechanical tuning, the g-C_3N_4 membrane displays exceptional H_2 permeability, without compromising on its superior H_2 filtering capability. Subjecting the membrane to slight biaxial strains of 2.5 and 5% resulted in the increase of H_2 flux to about 57.64 and 501.8 mols/m^2s, respectively, from the 6.47 mols/m^2s of the unstrained membrane, without sacrificing its H_2 selectivity over CO_2 and CH_4. Furthermore, we performed a comparison simulation to justify the use of the larger time-step of 0.4 fs in our simulations. A sample simulation carried out using a smaller time-step of 0.1 fs shows that using the larger time-step, which reduces the computational time significantly, has not compromised the accuracy of the simulations.

CHAPTER 7 STRAIN CONTROLLED C_2N FOR HYDROGEN PURIFICATION AND CARBON DIOXIDE SEPARATION

The graphene-like carbon nitride allotrope, C_2N is a stable, atomically thin 2D layered structure with regularly distributed pores. A monolayer of this holey structure in micrometre-scale has been synthesized by a simple wet-chemical reaction. It possesses periodically distributed uniform pores with openings of 3.0 Å. This is within the range of the kinetic diameters of the gas molecules studied in this thesis, making it a possible candidate for gas separation membranes. Previous studies have shown the C_2N monolayer to possess structural stability under strain values up to 10%, opening up the possibility to modify its gas permeability and selectivity characteristics for optimum separation efficiency.

This chapter details our investigation of C_2N membranes in industrial gas separation applications. The study focuses on the permeability characteristics of H_2, CO_2, N_2 and CH_4 through a C_2N monolayer and the effects of strain tuning on the permeability characteristics. In section 7.2.2, results and analysis of non-equilibrium molecular dynamics simulations studies are presented, while section 7.2.3 focuses on first-principles quantum mechanical simulations to analyse and explain the observed gas permeability characteristics of the C_2N monolayer.

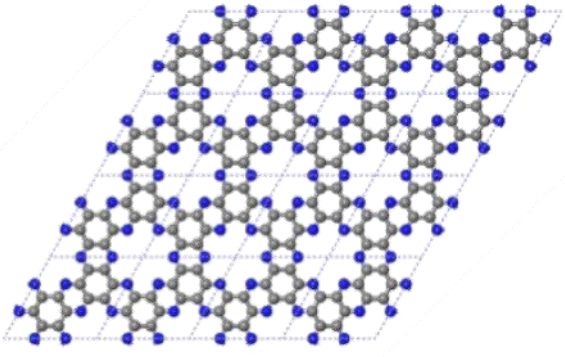

Figure 7.1: A 4×4 monolayer of 2D-C_2N

7.1 COMPUTATIONAL DETAILS

First-principles DFT simulations were carried out to obtain the fully relaxed geometry of the C_2N monolayer, the structure's behaviour under biaxial strains, and to scan the potential energy variation when a single gas molecule crosses the membrane. Non-equilibrium molecular dynamics simulations were used to simulate gas permeation across the membrane.

7.1.1 Density Functional Theory Calculations

DFT calculations were carried out using the DMol3 module in Materials Studio [144, 145]. First, a pristine 2×2 C_2N supercell was fully relaxed allowing both atomic positions and lattice parameters to relax. Next, the lattice size was increased by 3, 5 and 7%, to mimic the porous membrane being under biaxial strain of the respective value. For these geometry optimizations, the lattice parameters were kept fixed, while allowing the atomic positions to relax.

The generalized gradient approximation (GGA) treated by the Perdew-Burke-Ernzerhof (PBE) exchange corelation [135] with a basis set of all electron double numerical plus polarization (DNP) was used for the DFT calculations. The DFT-D method developed by Grimme et al. [169], was used for the long-range van der Waals corrections. A three dimensional crystal with a vacuum slab of 10 Å between the sheets in the Z-direction was used, with the Brillouin zone sampled by $7 \times 7 \times 1$ k-points using the Monkhorst-Pack scheme [170]. The atomic charges were calculated using the Mulliken charge analysis [161]. The convergence tolerance parameters were set as below.

Energy	:	1.0×10^{-5} Ha
Maximum force	:	2×10^{-3} Ha/Å
Maximum displacement	:	5×10^{-3} Å
Maximum iterations	:	50
Maximum step size	:	0.3 Å
Self-Consistent Field tolerance	:	1.0×10^{6}
Maximum SCF cycles:	:	50
Multipolar expansion	:	Hexadecapole

To study the effects of interatomic interactions between the gas molecule and the membrane, the preferred method is to scan the minimum energy pathway by carrying out transition state (TS) location calculations using a synchronous method. This calculation will locate the maximum point of the minimum energy pathway for a gas molecule to cross from the adsorbed phase of one side to the adsorbed phase on the opposite side. However due to the nature of the CO_2 gases' migration behaviour, the transition state search calculations would fail, without completing. The CO_2 molecule diffusing from one side of the membrane to the other side would adsorb on the pore, forming the strongest interaction when the molecule's geometric centre is in the same plane as the membrane. Since the TS search calculation would look for a maximum point along the pathway, the gradual decrease of the energy (stronger interactions imply larger negative energy values and thus the energy value will decrease) makes it unable to locate a maximum point.

Therefore, a series of step-by-step potential energy scan (PES) calculations were carried out for each gas molecule. A 3 × 3 cell of the C_2N monolayer under 5 and 7% strain values were used with the atomic positions and cell dimensions kept fixed. A gas molecule was placed perpendicular to the membrane material and its X and Y coordinates were constrained at the geometrical centre of the pore opening as shown in Figure 7.2. An exception is the CH_4 gas molecules where only the carbon atom at the centre was constrained and the hydrogen atoms were allowed to relax.

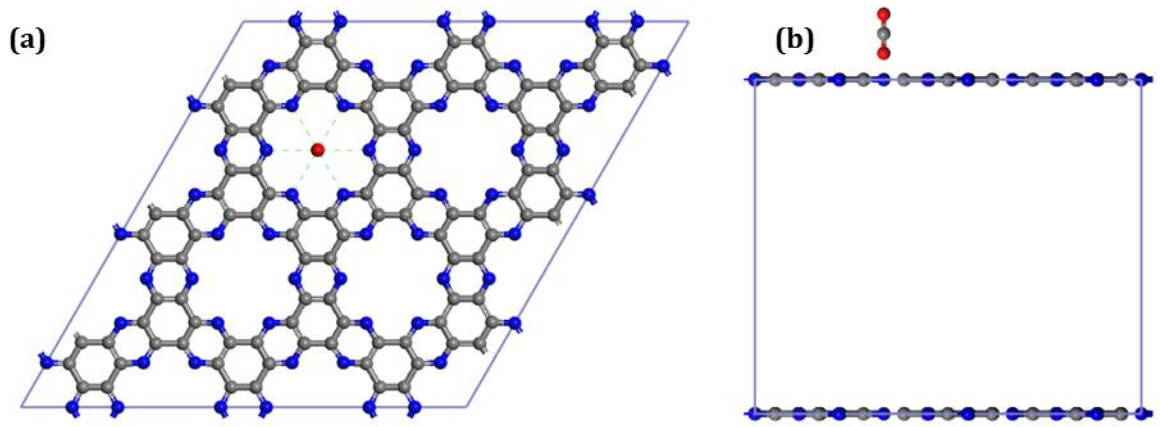

Figure 7.2: The simulation setup for energy scan of a gas molecule penetration through a pore opening. (a) The top view of a CO_2 molecule placed along the centre axis of the pore opening perpendicular to the membrane, (b) the side view of a CO_2 molecule placed. The distance between the membrane plane and the gas molecule is varied to scan the energy variation along the gas molecule pathway.

Then a series of constrained geometry optimizations were carried out to calculate the minimum energy by incrementing the Z-coordinates by 0.25 Å. For CO_2 and CH_4 gas molecules, the central atom position was increased by 0.25 Å and was constrained, while for H_2 and N_2, a single gas atom was kept fixed while the Z-coordinates of the other atom was allowed to relax. For these energy-scan simulations, the settings were maintained similar to the settings used in structural optimization simulations as mentioned above, except for using a 3×3 unit cell with a 20 Å vacuum slab between the membrane monolayers in Z-direction with $4 \times 4 \times 2$ k-point sampling. To discount the effects of the membrane's rigidity in the PES calculations, a sample TS search calculation of H_2 passage through the membrane was carried out. The comparison of the results of the two types of simulations allows determining how accurately the constrained system used in PES calculations resembles the actual system. Unlike with the energy scan simulations, the TS search calculations were performed allowing all the atomic positions to relax completely, and only the lattice parameters were maintained constant during the simulation.

7.1.2 Molecular Dynamics Simulations

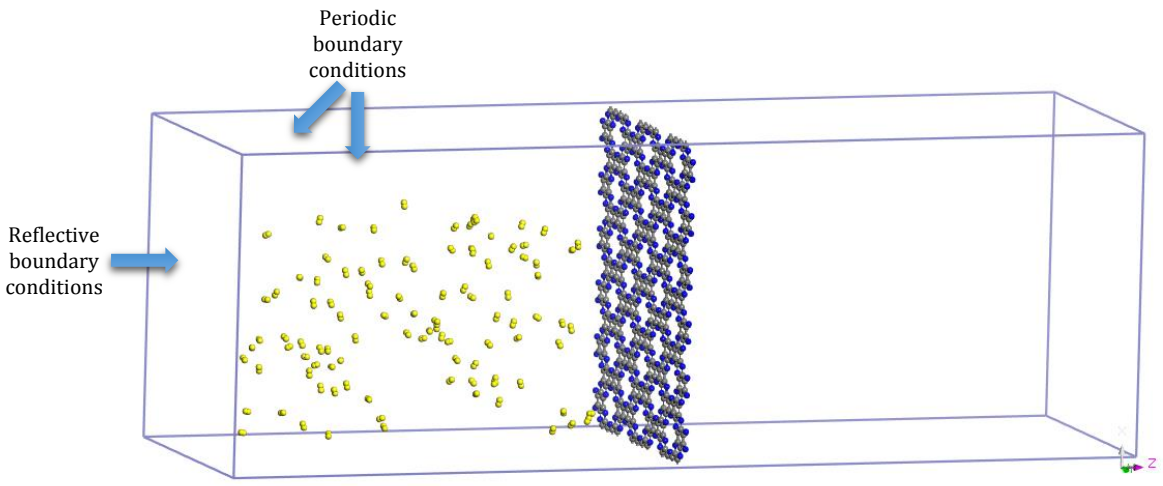

Figure 7.3: A typical simulation setup used in molecular dynamics simulation. The membrane is placed at the centre of the simulation box and the gas molecules were initially placed at one side of the box known as the reservoir. The simulation box is periodic in x and y directions and has a reflective boundary conditions in the z-direction. In this image, the length of the simulation box is reduced in half for illustrative purposes. The atom colour code: yellow. Hydrogen; blue, nitrogen; grey, carbon.

A frozen ~50 × 50 Å monolayer of C_2N obtained from DFT optimizations was placed at the middle of the simulation box, as shown in Figure 7.3. Periodic boundary conditions were applied in x and y directions and reflective boundary conditions were applied in the Z -direction. Initially 100 gas molecules were placed on one side of the membrane, which behaves as the gas reservoir. The simulations were performed using LAMMPS package. The NVT ensemble, with Nosé-Hoover thermostat was used to maintain the system temperature at 298.0 K. The system was equilibrated for 100 ps and next, production simulations were carried out for a total time period of 10 ns with a time-step of 0.25 fs. The atom trajectories were recorded every 1000 steps (25 fs) and the results were post processed using Matlab codes written to analyse the gas permeation behaviour. The simulation parameters used in this simulation is summarized below.

Ensemble	:	NVT
Temperature	:	298 K
Thermostat	:	Nose-Hoover
Q- ratio	:	0.01
Time step	:	0.25 fs
Number of steps	:	40000000
Initial velocities in equilibration	:	Random
Initial velocities in production	:	From equilibration simulations
Charges	:	Mulliken Analysis from DFT simulations for C_2N and from force field data for gases
Electrostatic terms	:	Summation method- Ewald Accuracy- 1×10^{-4} kcal/mol
Pair style	:	LJ with long range coulomb Cut-off distance- 12.0 A Mixing style- arithmetic

7.1.2.1 Force-field data

For the graphitic carbon nitride monolayer, only interatomic LJ potentials were required, while other bond, angle and torsional parameters were not needed, because the membrane was kept frozen during the simulations. The LJ parameters for C_2N were developed to be consistent with OPLS force field while the atomic charges were derived from the DFT calculations. A three-site model with a quadrupole moment of 0.651B [177] and a H-H bond length of 0741 Å developed by Alavi et al. [178] based on the model developed by Goldman et.al. [179] was used to model the H_2 gas molecules. The CO_2 molecule was modelled by the EPM2 model presented by Harris & Young [180], where it was treated as a rigid molecule of three sites with a quadrupole moment of 4.3B[2] [181] and a C-O fixed bond length of 1.149 Å. The N_2 gas molecule too is modelled as a three-site rigid molecule with a quadrupole moment of 1.44 B [177] with a rigid N-N bond length of 1.098 Å and a massless charge site at the centre of the molecule [182]. Finally the Stassen model [183] of five charged sites, a C-H bond distance of 1.09 Å and a H-C-H angle of 109.3°, was used to model the methane gas atoms. The force field data used are summarized in Table 7.1. The form of the Lennard-Jones potentials used in LAMMPS is given in Equation 7.1.

$$E_{LJ} = \sum_{i<j} 4\varepsilon_{ij}\left[\left(\frac{\sigma_{ij}}{r_{ij}}\right)^{12} - \left(\frac{\sigma_{ij}}{r_{ij}}\right)^{6}\right] \qquad \text{Equation 7.1}$$

[2] B-Buckingham (units of quadrupole moment)

Table 7.1: Summary of force field data used in MD simulations

Atom		σ (Å)	ε (kcal/mol)	Charge (e)
Membrane	C	3.3997	0.0860	Mulliken charge analysis –DFT simulations
	N	3.2499	0.1700	
H_2	H	0.0000	0.0000	0.4932
	Q	3.0380	0.0682	-0.9864
CO_2	C	2.7570	0.0559	0.6512
	O	3.0330	0.1599	-0.3256
N_2	N	3.3180	0.0723	-0.4048
	Q	0.0000	0.0000	0.8096
CH_4	C	3.5000	0.0660	-0.2400
	H	2.5000	0.0300	0.0600

7.2 RESULTS

7.2.1 C_2N under biaxial strain

From our first-principles density functional simulations, with no lattice constraints, we first obtained a fully relaxed geometry of a graphitic-C_2N unit cell. Figure 7.4 shows the geometry of a C_2N unit-cell with lattice length of 8.3 Å and a 60° angle. The lattice parameters are within the same range of previously published experimental value: 8.24±0.96 Å [83] and theoretical values such as 8.329 Å [85], 8.32 Å [115] and 8.354 Å [84]. The Figure 7.5 displays the charge distribution of the optimized unit-cell. The Mulliken charge analysis was used to analyse the charge density of the system. Compared with graphene where every atom is neutral, the C_2N shows obvious variation in charge distribution. Nitrogen, the more electrophilic atom out of the two, has a negative charge of -0.226, (-0.107 in Hirschfeld charge analysis) while the carbon atoms have a positive charge of 0.113 (0.059 in Hirschfeld). Similar to previous reports, the holey C_2N is estimated to have a pore opening of about 3.07 Å, and with a distance of 5.5 Å between two

opposite nitrogen atoms. The size of the opening is marginally bigger than the kinetic diameter of H_2, but is smaller than the rest of the gas molecules studied.

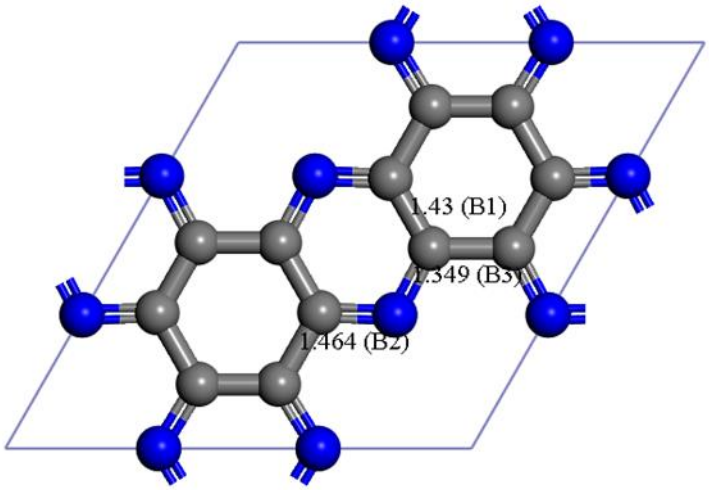

Figure 7.4: Fully relaxed structure of C_2N

Next, the behaviour of the C_2N monolayer under biaxial strain is evaluated. Table 7.2 summarizes the changes induced by various biaxial strains. The changes to the opening size are considered as those of the point-to-point distance between two opposing nitrogen atoms, but not the actual changes to the vdW pore dimensions.

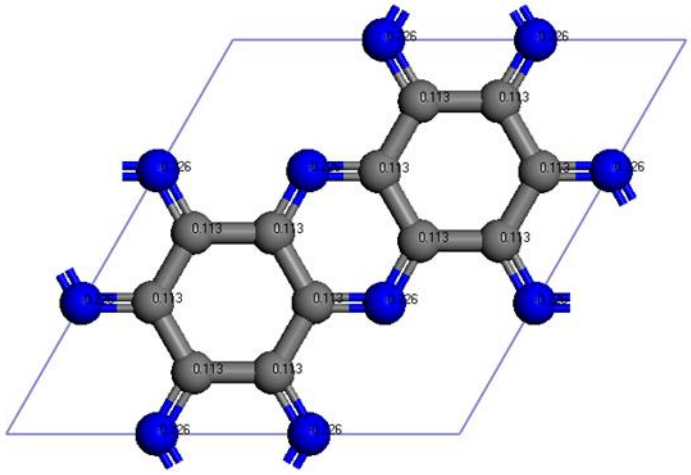

Figure 7.5: Charge distribution on C_2N, calculated using Mulliken charge distribution analysis

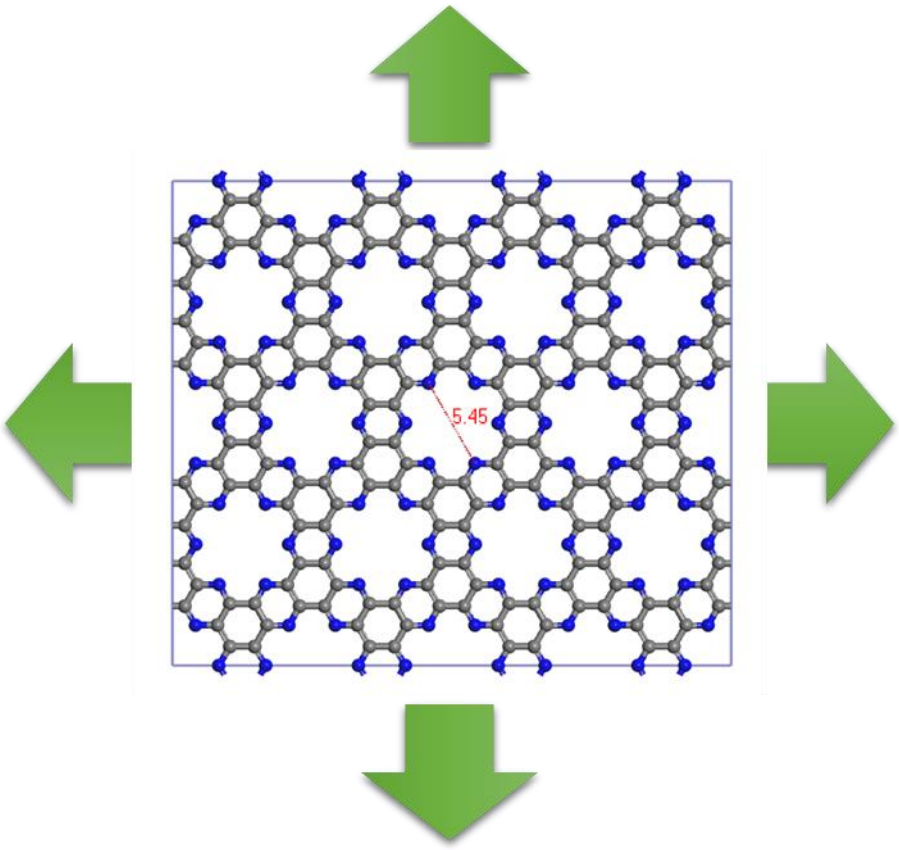

Figure 7.6: A fully optimized C_2N structure under biaxial strain. The distance shown in the image is the point-to-point distance between two nitrogen atoms directly facing each other.

Table 7.2: Structural changes induced on C_2N structure by increasing strain values

Strain (%)		**0**	**3**	**5**	**7**
Bond 1	**Length (Å)**	1.43	1.455	1.464	1.471
	Increase %	0	1.748	2.378	2.867
Bond 2	**Length (Å)**	1.464	1.547	1.595	1.651
	Increase %	0	5.669	8.948	12.773
Bond 3	**Length (Å)**	1.349	1.357	1.367	1.374
	Increase %	0	0.593	1.334	1.853
Pore distance	**Length (Å)**	5.449	5.848	6.036	6.225
	Increase %	0	7.322	10.773	14.241

The results tabulated show that the largest deformation occurs at the pore opening. The C-N bond shows most resistance to stretching, while out of the two C-C bonds, the bond forming an edge of the pore opening displays less resistance to elongation compared to the C-C bond within the aromatic ring, which has a high π-electron density. Interestingly, the C-C bond along the pore edge shows similar behaviour to the pore opening under biaxial strain, while the C-N bond and the C-C bond in the aromatic ring share the same trend. Generally, with the increase in each 1% of strain, the pore opening increases by around 1.6% in characteristic length except for the biaxial strain of 1%. When the membrane is subjected to 3, 5 and 7% biaxial strains, the point-to-point length of the pore opening increases by 7.3, 10.8 and 14.2%, respectively. Assuming a circular shape pore opening, this increases the pore area by approximately 15, 22 and 30% respectively. Our molecular dynamics simulations for gas permeation behaviour show, that these increases in pore area, significantly affect the gas permeability across the membrane.

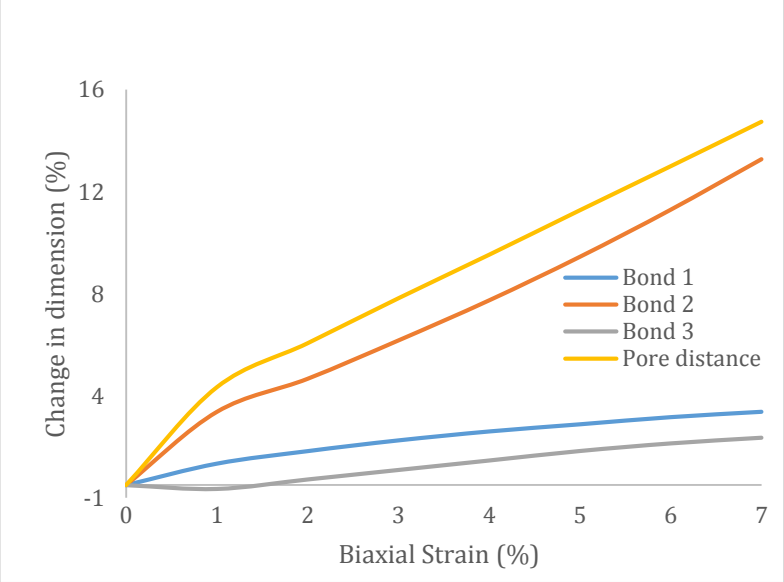

Figure 7.7: The variation of structural parameters with increasing biaxial strain

7.2.2 Molecular Dynamics Gas Permeability Simulation Results

Frist, the number of molecular crossing events that occurred in both directions during the simulation time was calcualted and the results are summarized in Table 7.3. Similar to the other two gas permeation studies, our results show that, while initially most of the molecular crossings occur in one direction: from the reservoir to the permeate side, once the number of gas molecules

on each side of the membrane becomes approximately equal, the gas crossings occur in either of the directions. A crossing event was considered to take place when one gas molecule traveled from the bulk layer on one side to the bulk layer on the other side. The definition of the bulk layer and the significance of calculating a gas crossing event in this manner is discussed in detail in section 5.3.2.

Table 7.3: Number of crossings across the membrane

	Strain - 0%	**Strain - 3%**	**Strain -5%**	**Strain - 7%**
H_2	3	5	58	645
CO_2	0	0	99	940
N_2	0	0	0	1
CH_4	0	0	0	0

The results summary shows that a pristine C_2N monolayer is nearly impermeble to any of the gases studied. During the entire 10 ns simulation period only three H_2 gas molecules, which is the gas with the smallest kinetic diameter, permeate through the C_2N membrane. The C_2N membrane under a 3% biaxial strain, which sees an approximately 15% increase to the pore area, still essentially remains impermeable to the gases studied, with only 5 hydrogen gas molecules crossing the membrane during the simulation period. However, when the biaxial strain of the membrane was increased to 5%, the ~23% increase in pore area caused the membrane to lose its impermeability to both H_2 and CO_2. The membrane shows remarkable improvement in permeability for both gases with 58 and 99 crossing events obeserved for the two gases, respectively, while still remaining impremeable to both N_2 and CH_4. Likewise, increasing the biaxial strain of the membrane to 7% sees the H_2 and CO_2 number of crossings increasing to 645 and 940 respectively. The 30% overall increase to the area of the pore opening has drastically reduced the energy barrier for gas transfer across the C_2N monolyaer, while still being impermeable to both N_2 and CH_4. The Figure 7.8 compares the H_2 and CO_2 crossings across the graphitic monolayer, under 5% and 7% biaxial strains, respectively.

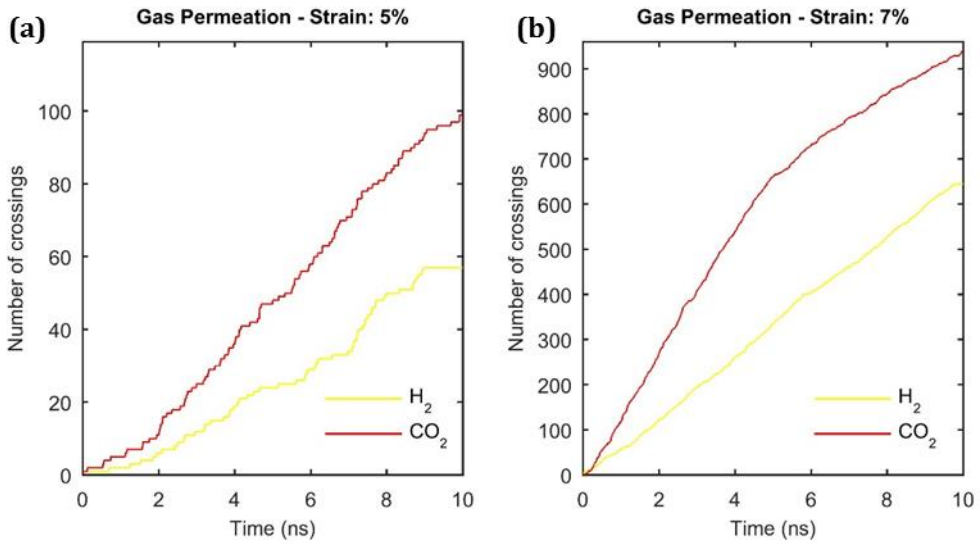

Figure 7.8: Number of crossings of H_2 and CO_2 gas molecules across the membrane in both directions under (a) 5% and (b) 7% biaxial strains respectively

Generally, the gas molecules with a smaller kinetic diameter are expected to have higher permeability. CO_2 however, exhibits a considerably higher permeability compared to H_2 which has a smaller molecular diameter. Therefore, we can assume that the gas permeability is not completely governed by the size effects of the membrane. The stronger inter-molecular attractions between CO_2 molecules and the membrane appear to have a dominant influence on the gas transport behaviour. These influences are further discussed in detail in sections 7.2.2.1 and 7.2.3.

However, the impermeability of the N_2 and CH_4 gas molecules can be attributed to the size exclusion effects of the membrane. Essentially, it can be concluded that despite being subjected to biaxial strains up to 7%, the membrane pore openings do not expand sufficiently to be permeable to the two larger gas molecules. This membrane therefore could be used in applications that require separation of H_2 or CO_2 from gas mixtures containing N_2 and/or CH_4.

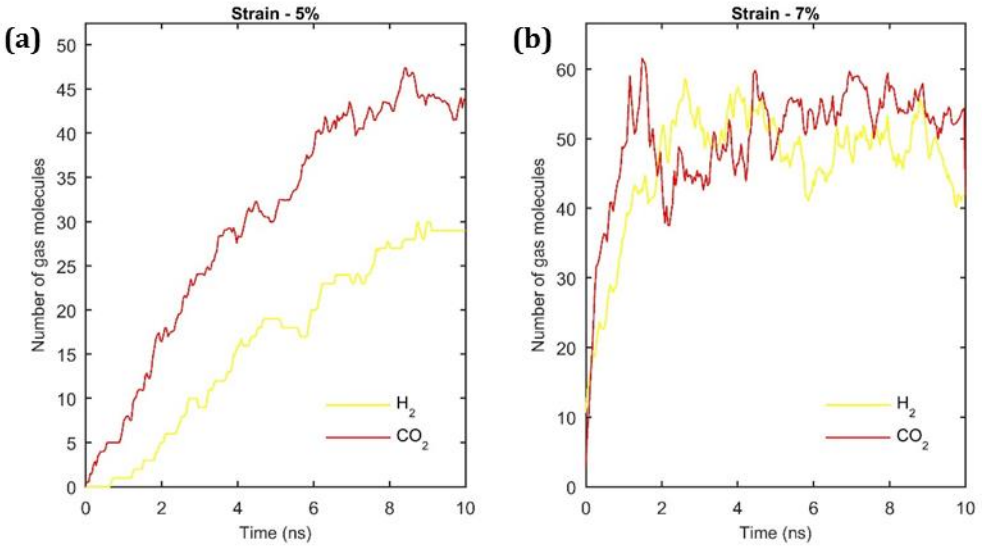

Figure 7.9: Variation of number of H_2 and CO_2 gas molecules on the permeate side of the membrane. These figures compare the number of gas molecules for membranes under 5 and 7% biaxial strains respectively.

7.2.2.1 Probability distribution and gas adsorption

The results show that while the H_2 and CO_2 permeation rates are dependent on the area of the pore opening, the order of flux does not depend on the kinetic diameter of the gas molecule. The higher CO_2 flux can be attributed to the adsorption of the CO_2 molecules at the pore opening. Figure 7.10 compares the gas distribution along the z-axis (in perpendicular direction to the membrane) for the four types of gases, while Figure 7.11 magnifies the distribution around the 1 nm distance from the membrane from either side of the membrane. The presented results are from molecular dynamics simulations for a C_2N membrane under 5% axial strain.

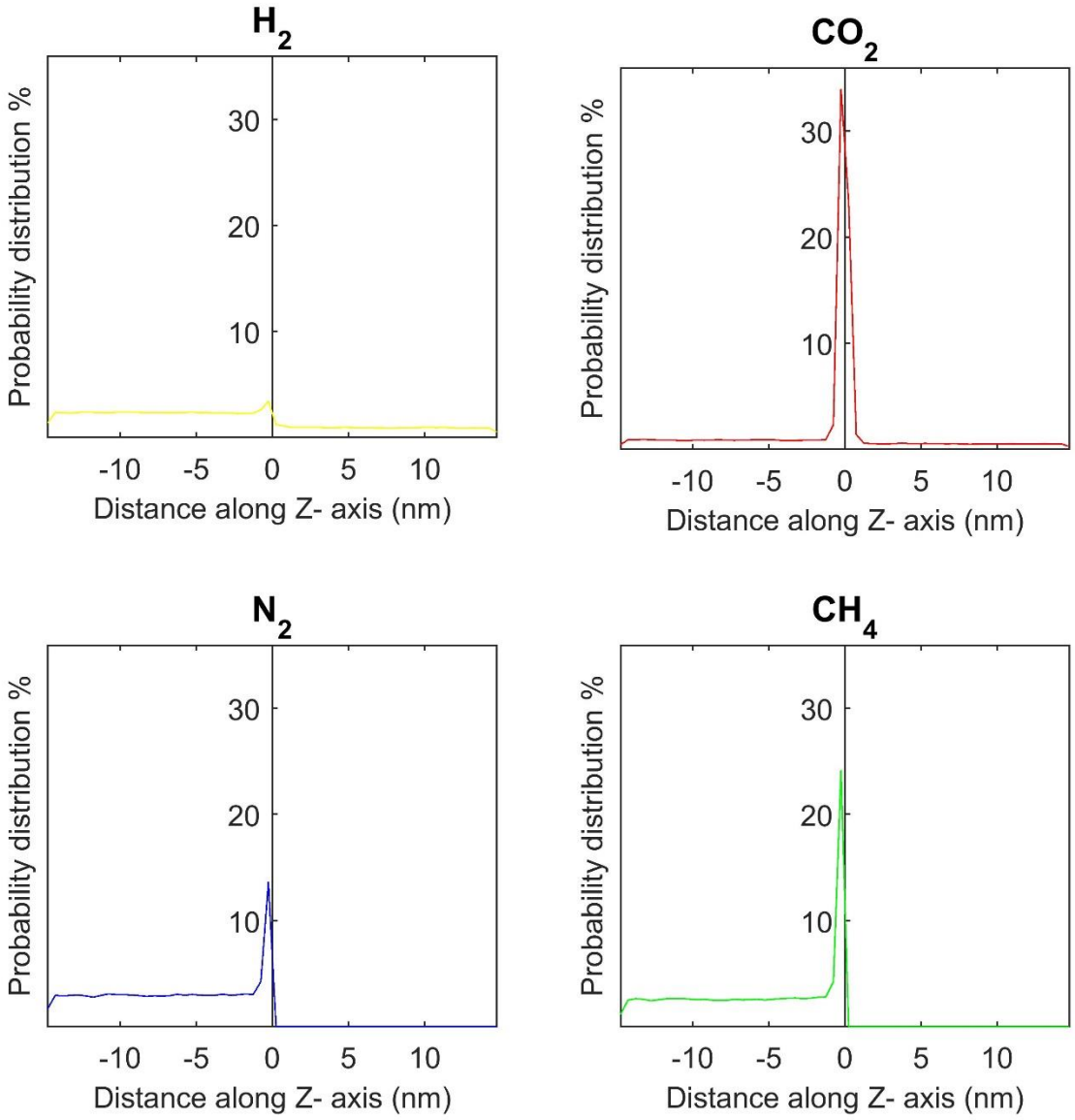

Figure 7.10: Probability distribution of gas molecules, along the Z-axis of the membrane. The membrane is placed at the centre where z=0 in the simulation box. The reservoir side is the negative side of the z-axis and while the permeate side is on the positive side. The N_2 and CH_4 gas molecules have zero probability on the permeate side. These results correspond to simulation systems under 5% biaxial strain

Analysing the trends in probability density of finding a gas molecule along the z-axis, shows CO_2 gas molecules experience a sizably stronger attraction to the membrane compared to the other three gas types. It is important to note that since the membrane is permeable to H_2 and CO_2 gas molecules, the probability distribution is spread along the z-axis on both sides of the membrane, while for N_2 and CH_4 gas molecules the probability distribution is concentrated only one side of the membrane. Even with this consideration, it is evident H_2 gas molecules are the least attracted to the membrane. The significantly higher CO_2 attraction can be attributed to its polarity and

electrophilic nature where the negatively charged N atoms at the pore edges, attract the electrophilic CO_2 gas molecule.

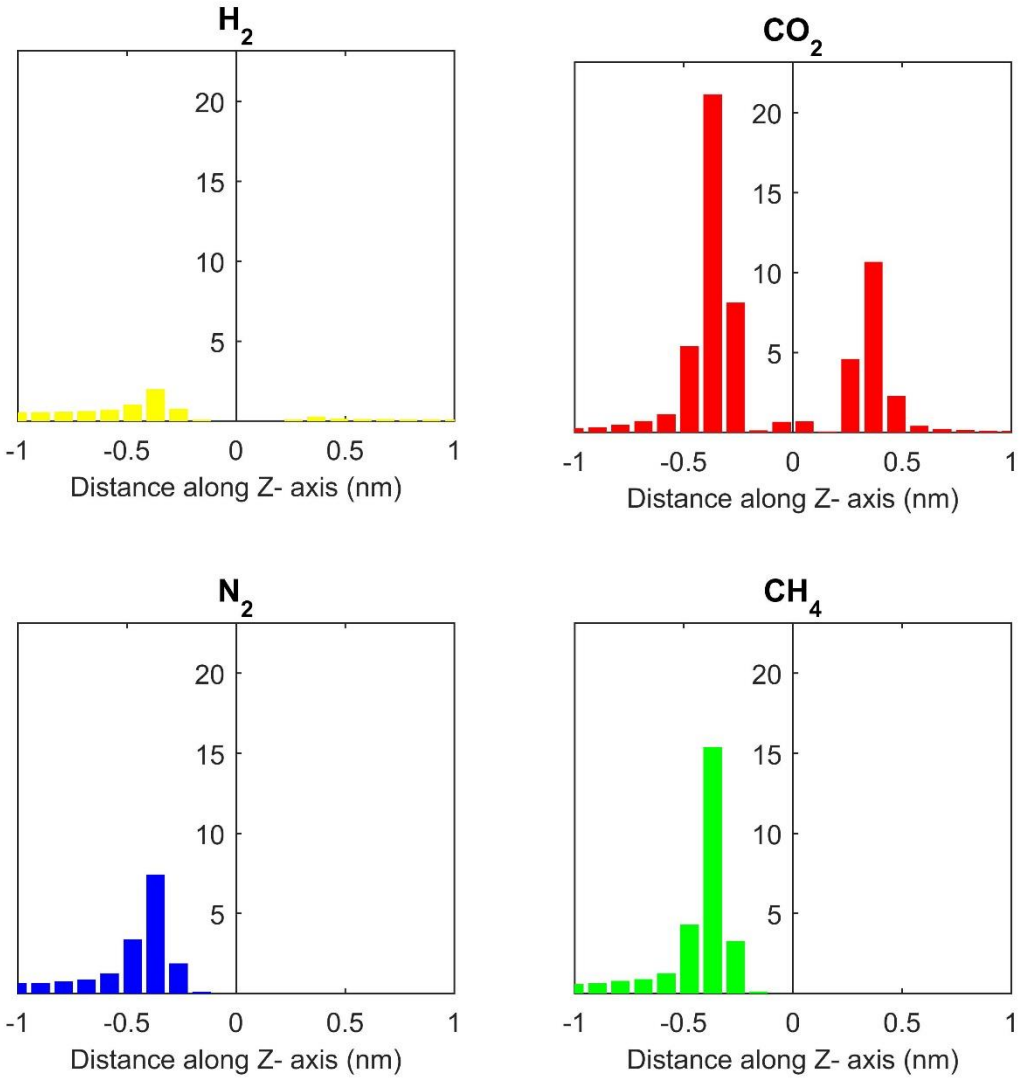

Figure 7.11: The probability distribution of gases from 1 nm (10 Å) from the membrane in both directions

The probability distributions of the gas molecules along 1 nm from the membrane position (at Z-axis=0) on both sides, confirm the strong attraction between the CO_2 gas molecules and the C_2N monolayer. The probability of finding a CO_2 molecule between 0.3 and 0.4 nm from the membrane in either side is in excess of 30% in total, implying that one third of the CO_2 molecules are concentrated at this zone. This molecular adsorption enriches the higher gas flux across the membrane, so that CO_2 gas molecules can overcome the steric hindrance at the pore opening. The H_2 molecule, with the weakest attraction to the membrane, only holds a probability distribution

of less than 5%. This further confirms that the H_2 molecular permeation occurs mostly due to direct molecular flux, and hence has a poorer flux despite having a smaller kinetic diameter than the CO_2 molecule.

Figure 7.11 highlights the fact that most of the gas molecules, can be found at a distance between 3 to 4 Å from the C_2N membrane (the interlayer spacing of a C_2N monolayer is 3.27 Å), suggesting predominantly physisorption behaviour between the gas molecules and the membrane. The table summarizes the calculated average distance of the adsorption layer within this range for each gas molecule. However, CO_2 molecules have a considerable concentration in excess of 1.5% within 1 Å distance from the membrane in both directions (the membrane zone) compared to the other gases, whose values are almost zero. This value increases to >5% for the membrane under 7% biaxial strain. This behaviour could be attributed to the stronger intermolecular interaction at the pore opening.

Table 7.4: The normalized position of the adsorption layer for each gas type

Strain	Gas type	Reservoir side (Å)	Permeate side (Å)
0 %	H_2	3.46	3.53
3 %	H_2	3.46	3.48
	CO_2	3.44	N/A
5 %	H_2	3.47	3.48
	CO_2	3.44	3.42
	N_2	3.49	N/A
	CH_4	3.53	N/A
7 %	H_2	3.47	3.47
	CO_2	3.45	3.44
	N_2	3.49	3.50
	CH_4	3.53	NA

The summary in Table 7.4 and the probability density analysis in Figure 7.10 and Figure 7.11 show that we can identify different zones for gas molecules along the Z-direction, with respect to the membrane. Between -1.5 to 1.5 Å in the z-axis, the probability density of gases is very low due to the occupancy of the membrane. The porous areas are occupied by only a few gas molecules due to the repulsion forces between membrane atoms and gas molecule atoms. This zone is named as membrane zone. From about 2 to 6 Å the highest gas density is observed, where the density peaks at about 3.4-3.5 Å and gradually decreases to a stable value at about 6 Å. This region can be identified as the adsorbed layer, and as mentioned earlier, the higher gas density is due to the intermolecular physical adsorption of gas molecules on the solid membrane. Beyond this region, the gas density distribution essentially displays a stable and constant distribution and this region will be identified as the bulk zone.

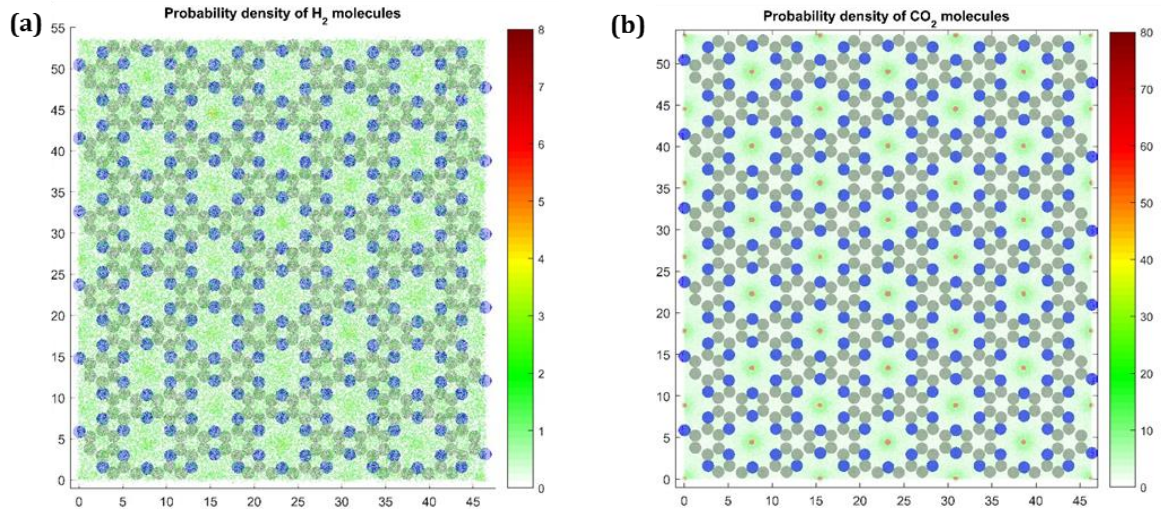

Figure 7.12: The probability distribution of (a) H_2 and CO_2 in the x and y directions for gas molecules within the membrane and adsorption zones. The shaded dark blue and grey areas represent the nitrogen and carbon atoms of the membrane.

In Figure 7.12, the probability distribution of H_2 and CO_2 molecules within the adsorption zone and the membrane layer are depicted with respect to the positions of carbon and nitrogen atoms of the C_2N membrane (in xy plane). The difference in the colour scale of the two distributions should be noted and was necessary to achieve visual clarity in the H_2 distribution, because the overall distribution is low and quite uniform barring the minor peaks at the centre of the pore opening. Alternatively, the CO_2 distribution shows how the CO_2 gas molecules have excessive

concentrations at the geometric centre of the membrane pore, with diminishing concentrations, moving away from the pore centre.

Figure 7.13 depicts a typical trajectory of each type of gas molecules along the Z-direction during the entire simulation period. These trajectories, further fortify the idea of an adsorption layer adjacent to the membrane area, where a gas molecule lingers around for an extended period. This behaviour is most apparent in the CO_2 gas molecule trajectory, which we have already established to display the strongest attraction to the membrane. The CH_4 and N_2 molecules exhibit such behaviour to a moderate extent and the least adsorptive behaviour is observed in the H_2 molecule.

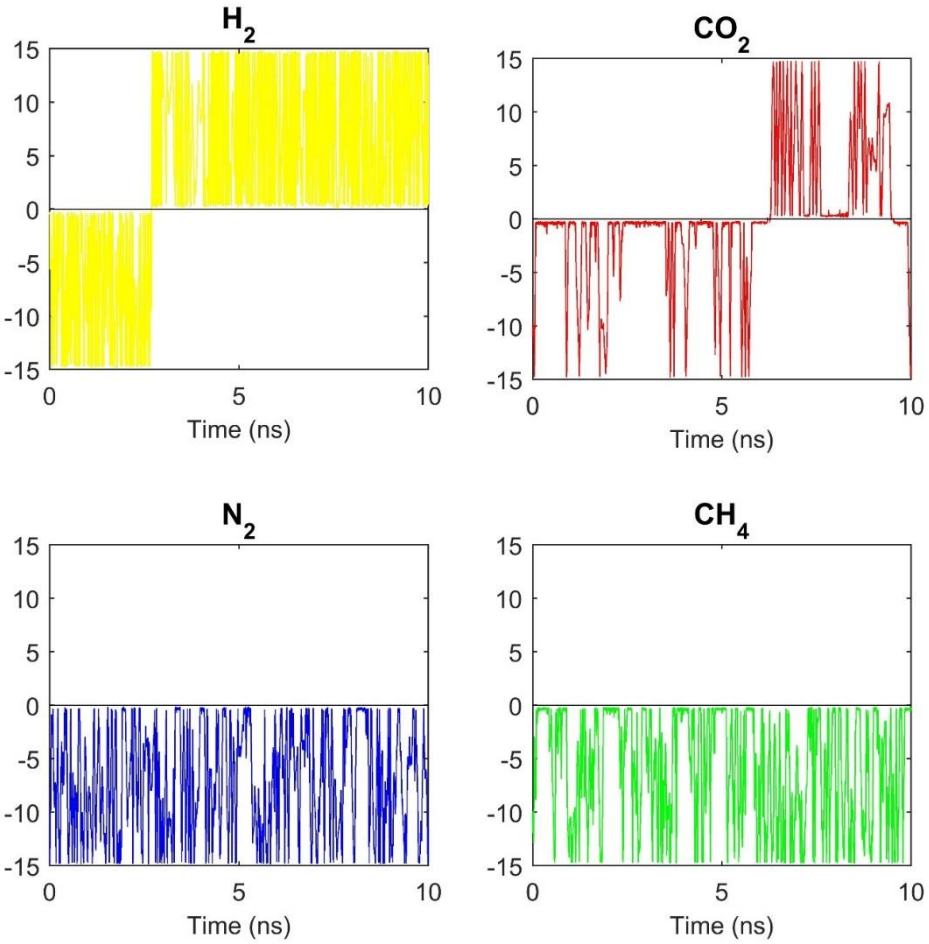

Figure 7.13: A typical trajectory of a gas molecule during the 10ns simulation period. these trajectories are representative of molecular simulation of membranes under 5% biaxial strain

Figure 7.14 shows a typical CO_2 molecule trajectory observed in simulations of a membrane under 7% biaxial strain. At this strain value, the pore area is expanded even more, and steric effects are less apparent. It can be seen that the CO_2 molecule occasionally, momentarily crosses over to the

opposite side of the membrane and at certain time intervals oscillates within the membrane nanopore, without actually crossing in to the bulk zone of the opposite side.

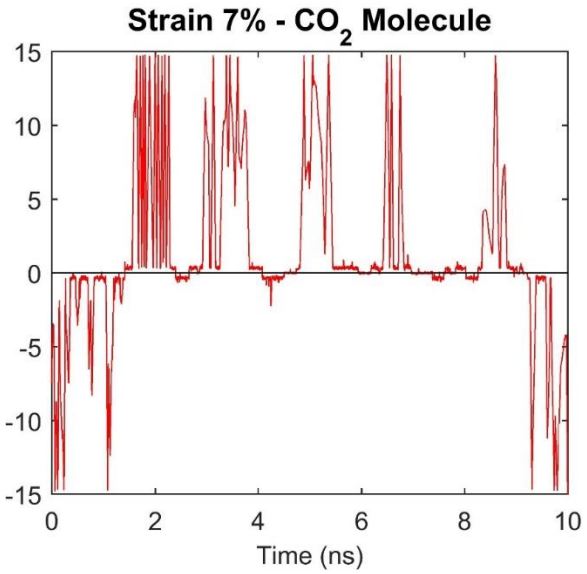

Figure 7.14: A typical trajectory of a CO_2 molecule in the membrane system under 7% biaxial strain

Based on trajectories of H_2 and CO_2 gas molecules, which are permeable through the nanopore, it is clear that every time a molecule reaches the membrane, it does not readily migrate to the opposite side of the membrane. While one of the main reasons for this is the membrane wall, Figure 7.12 shows that bulk of the gas molecules especially the CO_2 molecules in the membrane zone and the adsorption zone are concentrated above the distributed pores of the membrane rather than the membrane wall. Therefore, the factors preventing a gas molecule crossing straightforwardly to the opposite side could be attributed to the orientation of the gas molecule, the gas molecule's inability to overcome the energy barrier to diffuse through the nanopore and other intermolecular interactions in force such as interactions between gas-gas molecules. Regarding the molecular orientation, a gas molecule positioned perpendicular to the membrane, where its geometric centre coincides with that of the nanopore will have the smallest energy barrier.

Based on these observations, we can identify several possible pathways for a gas molecule to take. Therefore, in result analysis, a crossing-event is considered to occur, when a gas molecule, which

is in the bulk zone in one side of the membrane, moves to the bulk zone of the opposite side. Determining the flux, based on this method, prevents over-estimating the gas flux across the membrane, especially for CO_2 molecules, which tend to oscillate around the membrane.

7.2.2.2 Calculation of gas permeance

For the result analysis, the system pressure is calculated based on the pressure exerted by the gas molecules in the bulk phase, ignoring the gas molecules adsorbed on the solid membrane. It's important to note the gas density on the permeate side decreases to a certain degree for CO_2 and H_2 gas molecules due to the gas molecules crossings to the other side of the membrane. The gas permeance is calculated based on the overall nominal pressure of the system. The system pressure is calculated based on the median gas density throughout the entire simulation period as shown in Equation 7.3. Table 7.5 summarizes the pressure calculated based on the mean-gas-density in the bulk zone, the gas permeance calculated based on Equation 7.4 and the gas flux calculated from Equation 7.5, respectively. The third column lists the initial nominal gas pressure calculated from the nominal gas density, i.e. the total number of gas molecules in the feed side at the start of the simulation and total feed-side simulation box volume (Equation 7.2) for comparison. However due to the ambiguity of calculating the pressure, the gas permeability is discussed in terms of gas flux, in this report. The pressure is calculated using the ideal gas equation, since at lower pressure ranges, the deviation from ideal gas behaviour is considerably small.

$$\text{Nominal gas pressure } (P_N) = \frac{N_T RT}{N_A V_T} \qquad \text{Equation 7.2}$$

$$\text{Feed gas pressure } (P_F) = \frac{N_B RT}{N_A V_B} \qquad \text{Equation 7.3}$$

Where;

N_T : Total number of gas molecules placed in the feed zone initially. In this case 100 molecules

V_T : The total volume of the feed side of the membrane, i.e. half of the total volume of the simulation box

N_B : The normalized gas concentration in the bulk zone of the feed side

V_B : Volume of the bulk zone in the feed side

R : Gas constant

T : Simulation temperature

N_A : Avogadro number

$$\text{Gas permeation} = \frac{\text{Number of crossings (mols)}}{\text{Pressure} \times \text{membrane area} \times \text{time}} \quad \text{Equation 7.4}$$

$$\text{Gas flux} = \frac{\text{Number of crossings (mols)}}{\text{Membrane area} \times \text{time}} \quad \text{Equation 7.5}$$

Table 7.5: Summary of Gas permeation and flux

Strain	Gas type	Nominal Pressure (atm)	Feed pressure (atm)	Permeation (mol/m².Pa.s)	Flux (mol//m².s)
0%	H_2	12.58	11.85	~ 0	~ 0
3%	H_2	11.86	11.26	~ 0	~ 0
	CO_2	11.86	5.03	0.00000	0.000000
5 %	H_2	11.41	7.96	0.00043	403.7531
	CO_2	11.41	2.99	0.00172	689.1647
	N_2	11.41	9.99	0.00000	0.000000
	CH_4	11.41	8.72	0.00000	0.000000
7 %	H_2	10.99	5.65	0.00738	4323.732
	CO_2	10.99	2.24	0.02711	6301.253
	N_2	10.99	9.60	0.00001	6.703461
	CH_4	10.99	8.37	0.00000	0.000000

7.2.3 Quantum mechanical simulations

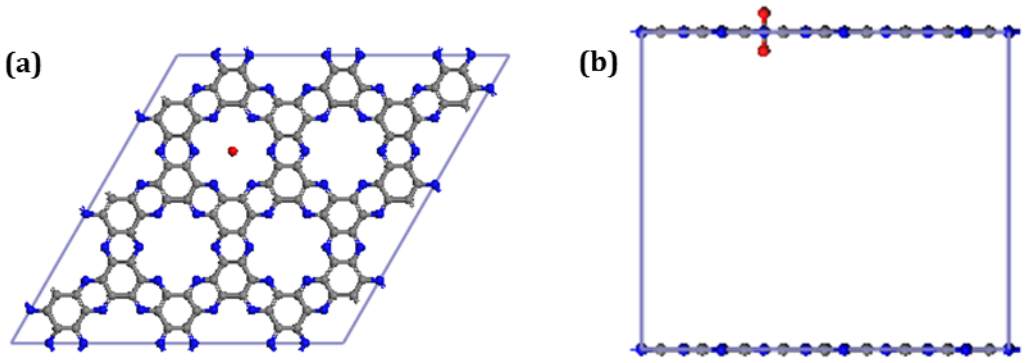

Figure 7.15: The (a) top view and the (b) side view of the PES calculation setup. The position of the geometric centre of the gas molecule was varied from 0 to 10 w.r.t the membrane and energy calculations at each position was performed

To understand the preferential diffusion of CO_2 compared to H_2, overcoming size-sieving effects, first-principles simulations were carried out to analyse the energy profile of a gas molecule crossing through the pore. The gas molecules were placed perpendicular to the membrane, aligned with the centre of the pore as shown in Figure 7.15. The total energy of the system was scanned as the gas molecule gradually penetrates the pore. A pathway where the gas molecule crosses the membrane perpendicular to it and through the centre yields the minimum energy barrier to crossing.

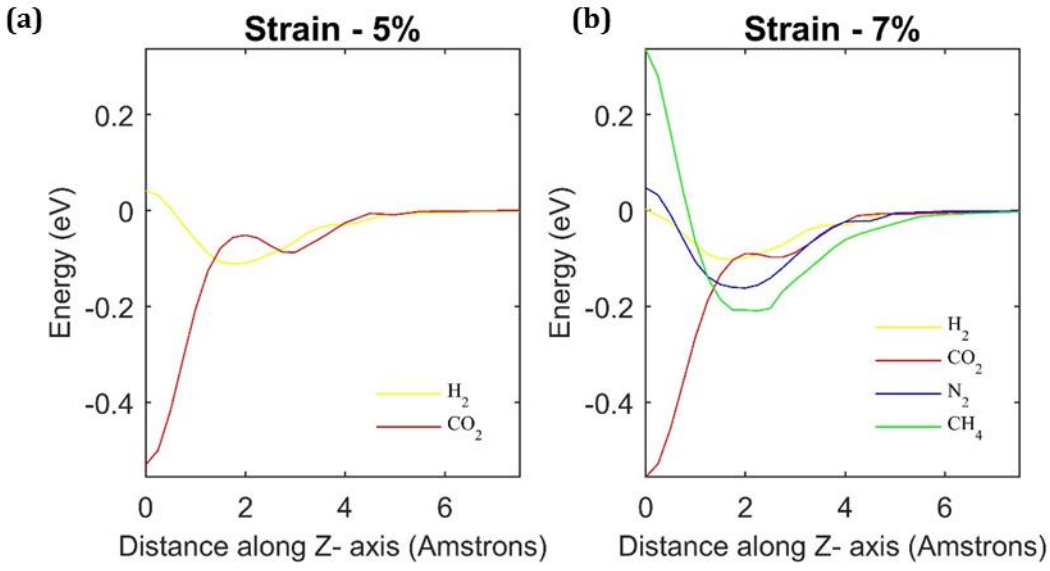

Figure 7.16: Energy profile for a gas molecule along the adsorption height for C_2N membranes under (a) 5% and (b) 7% biaxial strain

$$\mathbf{E_{Interaction}} = \mathbf{E_{gas+membrane}} - (\mathbf{E_{membrane}} + \mathbf{E_{gas}}) \qquad \text{Equation 7.6}$$

Where the $E_{gas+membrane}$ is the total energy of the system obtained from local, constrained geometry optimizations and the term ($E_{membrane} + E_{gas}$) is obtained from energy calculations of the total system containing the membrane cell and a gas molecule placed sufficiently far away from the membrane (10 Å in this case) such that the interaction between the membrane and the gas molecule is negligible.

Figure 7.16 shows the energy variation along the adsorption pathway. The energy represented in the figure was calculated as given in Equation 7.6. For the H_2 gas molecule, even when the membrane is subjected to biaxial strain, the repulsion energy (a positive interaction energy indicates intermolecular repulsion between the gas molecule and the membrane) gradually increases and reaches a maximum when the centre of mass of the H_2 molecule coincides with the geometric centre of the pore. However, we can observe when the increased biaxial strain causes the pore area to expand; the energy barrier for a gas penetration slightly decreases, promoting the increased gas flux across the membrane. Conversely, when the CO_2 molecule reaches towards the membrane plane the interaction energy gradually increases (the negative energy indicates stronger interaction) and reaches a maximum (of the absolute value) when the centre of gravity of the gas molecule overlaps the centre of the pore. It shows a minor bump from for the membrane under 5% biaxial strain indicating a small energy barrier for the gas when it transforms from the physisorbed phase to the chemisorbed phase. This adsorptive behaviour of the CO_2 molecule on the pore contributes towards the solution diffusion of the gas molecule. These observations further confirm the hypothesis that the CO_2 diffusion through the C_2N nanopore is not primarily governed by size exclusion effects but is mainly influenced by the CO_2 molecule adsorption on the nanopore.

The dip in the energy profile for all the gases between ~1.5 -3 Å is due to the physisorbed gases on the membrane. These observations are consistent with our probability distribution simulations where the CO_2 had the highest density in the adsorption region due to its strong

chemical interaction with the membrane, followed by CH_4, which has a somewhat strong physisorption energy, and hence the second largest gas probability density. The probability gas density and the physisorption energy of N_2 are placed third, while H_2 is the smallest on both accounts, proving the consistency between the two types of simulation methods. Furthermore, the energy profile proves the existence of an adsorption zone within 6 Å from the membrane. The table below summarizes the penetration energy barrier calculated based on the minimum and the maximum energy values of the energy profile.

Table 7.6: Summary of energy barriers

Strain	Gas type	Energy barrier (eV)
5%	H_2	0.153
	CO_2	0.0303
7%	H_2	0.104
	CO_2	0.007
	N_2	0.209
	CH_4	0.545

As mentioned in section 7.3.1 to justify the use of constrained atomic coordinates, a TS search calculation was performed for H_2 travel through a C_2N membrane under 7% biaxial strain. TS search calculations were carried out for physisorbed configurations of the H_2 molecule at ~2.0 Å away from the membrane in either directions. Figure 7.17 compares the TS search results with our previous calculations under fully constrained conditions. In TS search calculations, only the lattice constants are constrained and the atomic positions of the membrane and gas molecule are fully relaxed. The results of the two methods are complimentary to each other, where the energy barrier in TS search calculation is 0.107 eV while the energy barrier from previous PES calculations is 0.104 eV. The excellent agreement of the results proves that our assumption of a constrained system does not affect the accuracy of the results significantly.

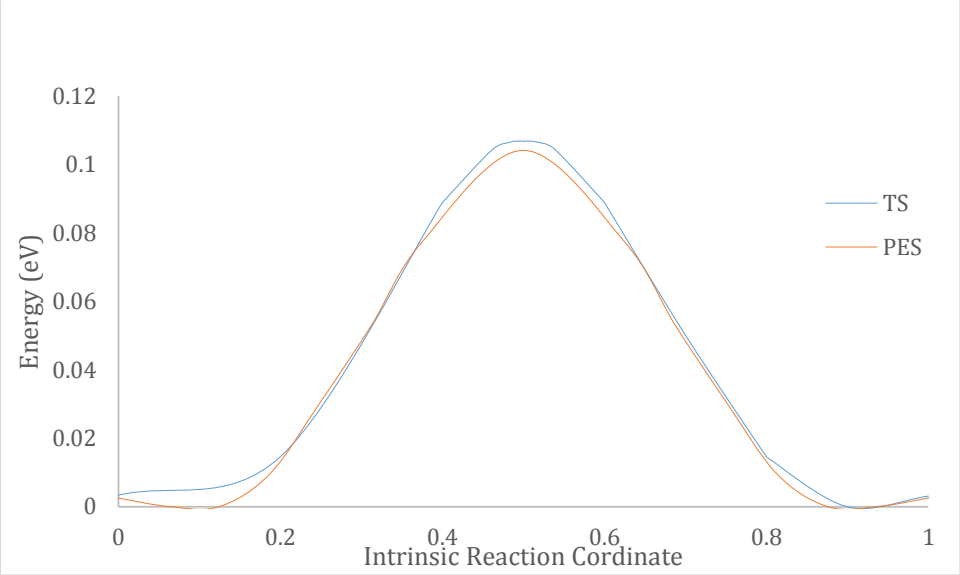

Figure 7.17: The comparison of potential energy scan along various points of the Z-axis and TS search calculations

7.3 DISCUSSION

The gas permeability of a 2D-C_2N membrane for small gas molecules, essentially focusing on key gases related to clean energy production, namely; H_2, CO_2, N_2 and CH_4 were evaluated. Our study shows that a fully relaxed pristine C_2N monolayer is hardly permeable to any of the gases in focus. However, using strain tuning, gas permeability characteristics of the membrane can be effectively altered to be permeable to H_2 and CO_2 molecules, while its N_2 and CH_4 impermeability remains intact.

A 5% biaxial strain improves the hydrogen gas flux to 403.7 mol/m²s while further increasing the biaxial strain to 7% boosts the gas flux to 689.2 mol/m²s. Due to its impermeability to CH_4 and N_2 despite the strain tuning, this characteristic can be exploited for H_2 purification from gas mixtures containing the latter two, especially in applications in hydrogen production as an energy source.

Similarly, when the membrane is under 5% biaxial strain it becomes permeable to CO_2 gas molecules with a gas flux of 689.2 mol/m²s. This value increases in approximately ten folds to 6301.3 mol/m²s, when the strain value is increased to 7%. Due to the high permeability to CO_2 under strain without compromising its selectivity over N_2 and CH_4, this membrane can be suggested for a number of industrial applications requiring CO_2 removal from gas streams. Its CO_2 selectivity over N_2 makes it an ideal candidate in post-combustion carbon capture, where CO_2 is

separated from streams of flue gases, where the other principle constituent is N_2. Similarly, the excellent CO_2/CH_4 selectivity, makes a strain tuned C_2N an ideal candidate for natural gas sweetening.

An interesting observation of this study is that the CO_2 molecule has a higher gas flux through the membrane compared to H_2, despite having the larger kinetic diameter out of the two. This shows that size sieving is not the only factor governing gas diffusion through the monolayer. The analysis of the gas distribution in the direction perpendicular to the membrane shows that CO_2 strongly adsorbs on the membrane while the H_2 adsorption is the poorest among the gases studied, confirming chemical affinity sieving is the principle mechanism for CO_2 diffusion.

This rationale was further strengthened by the potential energy scan calculations for CO_2 and H_2 crossing through the pore. The results showed that while the H_2 molecule has a slight energy barrier for diffusion, the CO_2 molecule in fact strongly binds with the pore with a binding energy of ~0.5 eV. The adsorptive diffusion of CO_2 through the C_2N monolayer can be attributed to the electrophilic nature of the CO_2 molecule. The negatively charged nitrogen atoms at the pore rim, readily attracts the CO_2 gas molecules causing the preferential diffusion of the gas molecule. In fact the reverse effect was observed by Wang et.al studying the CO_2 and N_2 diffusion characteristics through a hydrogen-passivated graphene pore [116]. They noticed that the positively charged hydrogen atoms at the pore ring repulsed the CO_2 molecules from the membrane pore and as a result, the N_2 had a higher flux despite having a larger kinetic diameter than the former. This confirms that the diffusion characteristics of a polar gas molecule like CO_2 can be influenced by not only size effects, but also by its chemical affinity with the pore.

7.4 CONCLUSION

Overall, the graphitic C_2N membrane, which is impermeable to all the gases studied under natural conditions, can be tuned into a H_2 purifying membrane and an excellent CO_2 capture membrane. Our MD simulations show that the near zero fluxes of these two gases through a membrane under no strain increases to 403.75 and 689.16 mol/m^{2}s, when the strain on the membrane is increased to 5%. Likewise, the increase in strain value to 7% sees the gas fluxes increase by approximately

10 times for both gas types. While the gas fluxes of H_2 and CO_2 increases to 4323.73 mol/m^{2}s and 6301.25 mol/m^{2}s, respectively, the membrane remains impermeable to both N_2 and CH_4 making this membrane suitable for H_2 purification applications, CO_2 separation in post-combustion carbon dioxide capture and natural gas sweetening.

Comparison of the H_2 and CO_2 permeabilities shows that the larger gas molecule, CO_2, in fact has a higher gas flux through the membrane. This contradictory behaviour is attributed to the higher CO_2 concentration closer to the membrane region, compared to the H_2 gas concentration, confirming the passage of the CO_2 molecule is governed principally by chemical affinity and under sufficient strain to open the pore, and the size sieving effects are only secondary. Furthermore, DFT simulations of PES calculations to identify the minimum energy pathway confirms that the CO_2 molecule in its minimum energy pathway actually adsorbs on the pore strongly while the H_2 molecule has a small energy barrier to overcome to penetrate through the pore opening. The N_2 and CH_4 molecules even under a strain value of 7% have a higher energy barrier to overcome. The stronger CO_2 adsorption is attributed to its electrophilic nature.

CHAPTER 8 CONCLUSIONS AND SUGGESTIONS

8.1 RESEARCH SUMMARY

With the advance in the field of nanomaterials and nanotechnology, the precise separation of gas molecules within a similar size range is now a possibility. This study, has investigated how low-dimensional carbon-based and graphene-like nanomaterials can be used in industrial gas separation applications, related to energy generation applications. Specifically, with the use of first-principles quantum mechanical simulations and non-equilibrium MD simulations, we have studied four different structures, their gas separation capabilities, their interactions with gas molecules and how these interactions affect the overall separation efficiency. Conclusions from this research can be summarized as below:

1. Charge controlled boron-doped fullerene for CO_2 separation

    - *Ab initio* DFT simulations performed in this study have shown that, boron doped C_{60} fullerene, under neutral conditions only forms a weak bond with the studied three gases: CO_2, N_2 and CH_4. While the adsorption energy of CO_2 is the highest among the three gases, the resulting adsorption energy of -2.04 kcal/mol and the adsorbed molecular structure indicates only a weak physisorption of the CO_2 molecule which is not sufficient for any meaningful separation

    - When the adsorbent is subjected to an electric field of $1e^-$ the added electron is mostly taken up by the doped boron atom, which has only three electrons in the outer orbital.

    - The CO_2 adsorption on the charged BC_{59}^{-1} becomes much stronger compared to the neutral state due to the charge transfer between the adsorbent and the adsorbate. The noticeable structural distortions and the adsorption energy of -15.41 kcal/mol strongly suggest a chemisorption of the gas molecule.

- Conversely, the N_2 and CH_4 molecules hardly see a noticeable change in the adsorbed configurations and the adsorption energies remain closer to the values observed in neutral conditions, suggesting the adsorption remains only physical.
- Due to the preferential adsorption of CO_2 gas molecule on BC_{59}^{-1}, over N_2 and CH_4, confirmed by the marked difference between the interaction energies between the gas adsorbent and the adsorbates, CO_2 can be effectively separated from the latter gases using BC_{59}^{-1}.

2. Porous hexagonal boron nitride membranes for gas separation

- The non-equilibrium MD simulations show, the h-BN membrane with a pore-10 type opening is impermeable to all the gases studied (H_2, CO_2, N_2 and CH_4). However, under 2.5 and 5% biaxial strains, the opening becomes permeable to H_2 gas molecules with molecular fluxes of 261.7 and 498.8 mol/m^{2}s despite its impermeability for all the other three gases studied in this thesis. Therefore, an h-BN membrane with a pore-10 type opening under biaxial strains between 2.5 and 5% can be effectively used for H_2 purification from gaseous mixtures containing CO_2, N_2 and CH_4.
- The membrane with a pore-13-B type opening is permeable to only H_2 gas molecules under normal conditions with a flux of 276.3 mol/m^{2}s. Under a 2.5% biaxial strain, the membrane becomes permeable to CO_2 with a flux of 1697.3 mol/m^{2}s and is weakly permeable to N_2 with a 454.2 while the H_2 permeability increases to 7410.8 mol/m^{2}s. When the strain is increased to 5% the membrane becomes permeable to all the gases studied. Therefore, a membrane at neutral conditions can be used to effectively separate H_2 from the rest of the gas types. Similarly, under a 2.5 strain it can be used for H_2/ CH_4, CO_2/CH_4 separation, and due to the significant differences in CO_2 and N_2 fluxes in CO_2/N_2 separation applications as well. Under 5% strain, no separation can be achieved among these types of gases.

- The pore-13-N type has the biggest opening due to the short bond distance between the nitrogen atoms at the pore edge and the terminating hydrogen atoms. However, under normal conditions it is only permeable to H_2 with a molecular flux of 1199.3 mol/m^{2}s and hence can be used to purify H_2 from gaseous mixtures of CO_2, N_2 and/or CH_4. However, even under a strain as little as 2.5%, the membrane becomes permeable to all the gases studied and no further separation can be achieved.
- The results show that when the pore openings become sufficient enough such that the size effects are not the dominant factor governing the gas transport through the opening, the intermolecular interactions between the gas molecules and the membrane have a significant impact on gas permeabilities.
- Furthermore, a sample study was carried out to compare the gas transport behaviour in binary gas mixtures, using an equimolar mixture of H_2 and CO_2. The increase in gas fluxes relative to the partial gas pressure of the gas type which forms a stronger interaction with the membrane, is higher than the pure gas permeability, while the reverse is applicable to the gases with smaller interactions.

3. Strained graphitic carbon nitride for hydrogen purification

- The non-equilibrium MD simulations have shown that g-C_3N_4 under normal conditions is only permeable to H_2, and when the feed pressure is increased, the gas flux increases in a near linear manner. Under 10, 20 and 30 bar initial feed side pressure values, the flux values vary as 6.47, 13.53 and 19.41 mol/m^{2}s, respectively.
- When the membrane is subjected to biaxial strains of 2.5 and 5% and the initial feed side pressure is maintained the same at 10 bar, the gas flux increases almost exponentially to 57.54 mol/m^{2}s and 501.80 mol/m^{2}s, respectively, from the initial weak flux of 6.47 mol/m^{2}s.

- However, even under a 5% biaxial strain, the membrane remains impermeable to the CO_2 and CH_4 gas molecules, confirming the g-C_3N_4 membrane can be effectively strain tuned to improve its gas separation efficiency without sacrificing its H_2 selectivity.
- The DFT simulations of transition state search confirm the observations of molecular dynamics simulations showing the gradual decrease in energy barrier for H_2 penetration through the pore opening with increasing strain, and hence, pore area.

4. Strain controlled C_2N for hydrogen purification and carbon dioxide separation
    - The non-equilibrium MD simulations show that the 2D-C_2N structure under no strain, is not permeable to the four gases studied in this thesis
    - The C_2N membrane under 3% strains is still impermeable to all the gases, while further increasing the biaxial strain of the membrane to 5%, sees it becoming permeable to both H_2 and CO_2 gas molecules, with fluxes of 403.75 mol/m^{2}s and 689 mol/m^{2}s respectively.
    - Further increasing the strain value to 7%, improves the H_2 and CO_2 fluxes to 4323.73 mol/m^{2}s and 6301.25 mol/m^{2}s, without losing its ability to block N_2 and CH_4. Therefore, this kind of membrane can be mechanically tuned by strain to alter its gas permeability and to improve its performance. Under appropriate strain, it can be used in H_2/CH_4, CO_2/N_2 and CO_2/CH_4 separation applications.
    - Interestingly, CO_2 with a larger kinetic diameter has a higher permeability compared to H_2 with a smaller molecular size, due to chemical affinity overcoming size exclusion effects.
    - The DFT simulations of the potential energy scan confirms the observations of the MD simulations, showing that the CO_2 molecule in its minimum energy pathway in fact adsorbs at the centre of the pore with a negative adsorption energy.

Conclusively, this work has shown that adsorption and membrane gas separation can be taken beyond traditionally studied low dimensional materials for effective separation, especially concerning H_2 and CO_2 separation from gaseous mixtures containing N_2 and CH_4. The theoretical simulation confirms the ability to alter the separation efficiency by manipulating chemical structure, charge state of the adsorbent and mechanical strain.

8.2 LIMITATIONS

Though this study provides a comprehensive understanding of the gas separation characteristics of the low dimensional nanomaterials especially combining DFT and MD simulations whenever permissible, few limitations have been identified.

- **Assumption of pristine systems**: In this theoretical study, all the materials used are pristine barring the BC_{59} structure and h-BN structure with introduced pores terminated with hydrogen atoms. Even in the latter two material systems, the defects are pre-determined and do not take into account the random defects that can appear in large-scale synthesis of materials. Such defects can affect the selectivity of the materials and affect the gas permeability or adsorption energies to a certain degree.

- **Assumption of ideal conditions:** The simulation studies, carried out in this thesis mostly assume ideal behaviour. For membrane gas separation studies, the conclusion of gas permeability is based on pure gas systems. However, in actual industrial gas separation, there will be more than two constituents within a system, and the gas permeability behaviour will be affected by the presence of other gas types in the system. To get an understanding of the behaviour of gas mixtures, we have carried out a sample simulation to identify the departure of behaviour from pure systems in the presence of other types of gas molecules. While, this does not reflect the actual industrial conditions (variation in mole ratio as opposed to the equimolar ratio used in the simulations and presence of other impurities in the system) this will provide a benchmark to identify the variation trends of the gas separation behaviour.

- **Scale of simulation systems**: In this study, the time and size scale of the simulations are in nano scale whereas in industrial scale, the operations occur in macro scale. Therefore, it is uncertain whether the exact values obtained from simulations translate from nano-scale to large scale. However, in this regard, specifically in membrane separation studies we have tried to identify the different behaviour in gas molecules closer to the membrane and in the bulk region. While even the bulk region is within nano-metre scale, the gas molecules within this region can be assumed to behave closest to large-scale systems.
- **Limitations of theoretical methods**: In this study, for different molecular systems, we have employed different methods and settings based on availability of theoretical resources such as force field data, different settings such as timescale and boundary conditions, and different operational conditions such as feed side initial pressure to balance the accuracy of the simulations, and the demand for computational resources. The variation in these parameters makes it ambiguous to quantitatively compare the results across the multiple studies but will provide for qualitative analysis of the behaviour.
- **Lack of experimental studies**: All the studies, in this thesis are purely theoretical and seldom will theoretical studies match experimental studies unerringly. However, the study employs well-established simulation methods with established parameters, to minimize such differences. To reduce the errors that can arise from the limitations of the theoretical model itself, a combination of MD simulations and DFT simulations are used whenever permissible by the scale of the simulations.

8.3 FUTURE DIRECTIONS

In this study, it has been attempted to study and do a comprehensive analysis of the gas separation characteristics of low dimensional nanomaterials. However, to overcome the above-mentioned limitations and to generally optimize these materials' gas separation efficiency, several suggestions and recommendations are proposed.

With the advancement of computational science, simulation systems with larger scales for a longer simulation periods is becoming a reality. Therefore, developing a more realistic technique to do multi scale modelling capable of handling larger systems, for a longer period of simulations, while maintaining details of the nano-scale will match simulation results to experimental systems is important.

Furthermore, in the study with porous BN membranes, our simulations are focussed on pores with edges terminated with hydrogen atoms. However, as our other simulation studies have confirmed, the atoms on the edge of the pore influences the gas selectivity and permeability. Therefore, further studies focussing on different terminal groups and various functionalization, and how they affect the gas separation behaviour will give more options to tune the membrane to obtain precisely controlled characteristics.

While both C_3N_4 and C_2N are experimentally synthesisable, further research on economical large-scale synthesis is vital for the development of atomically thin carbon nitrides as an industrial gas separation membrane. In the boron nitride membranes, the pores are not inherent, but created on a pristine boron nitride monolayer. While experimental techniques exist to create openings in that size scale, more research on techniques that offer precise control over pore opening size, shape and uniform distribution will further the nano membranes with introduced pore openings.

In the gas adsorption study on BC_{59}, the research is limited to the individual interaction between the gas molecules and the adsorbent. This will establish the gas separation characteristics of the adsorbent and will give more of a qualitative analysis of the adsorption process. However, to achieve a quantitative analysis large-scale simulations are required to analyse the gas adsorption capacity and other similar parameters. Furthermore, research to develop methods to dope the C_{60} fullerene with more boron atoms far apart from each other, will improve the gas sorption capacity of a single doped fullerene.

CHAPTER 9 BIBLIOGRAPHY

[1] R. K. Pachauri and A. Reisinger, "Climate Change 2007: Synthesis Report. Contribution of Working Groups I, II and III to the Fourth Assessment Report of the Intergovernmental Panel on Climate Change," *Intergovernmental Panel on Climate Change,* 2007.

[2] IEA, *World Energy Outlook 2011*: OECD Publishing, 2011.

[3] J. G. J. Olivier, G. Janssens-Maenhout, and J. A. H. W. Peters, "Trends in Global Carbon Dioxide Emissions: 2012 Report," PBL Netherlands Environmental Assessment Agency, The Hague2012.

[4] M. Winter and R. J. Brodd, "What Are Batteries, Fuel Cells, and Supercapacitors?," *Chemical Reviews,* vol. 104, pp. 4245-4270, 2004/10/01 2004.

[5] L. Carrette, K. A. Friedrich, and U. Stimming, "Fuel Cells: Principles, Types, Fuels, and Applications," *ChemPhysChem,* vol. 1, pp. 162-193, 2000.

[6] M. Balat, "Potential importance of hydrogen as a future solution to environmental and transportation problems," *International Journal of Hydrogen Energy,* vol. 33, pp. 4013-4029, 8// 2008.

[7] K. B. Lee and S. Sircar, "Removal and recovery of compressed CO2 from flue gas by a novel thermal swing chemisorption process," *AIChE Journal,* vol. 54, pp. 2293-2302, Sep 2008.

[8] J. Wilcox, *Carbon Capture*. New York: Springer, 2012.

[9] A. Brunetti, F. Scura, G. Barbieri, and E. Drioli, "Membrane technologies for CO2 separation," *Journal of Membrane Science,* vol. 359, pp. 115-125, Sep 1 2010.

[10] D. Singh, E. Croiset, P. L. Douglas, and M. A. Douglas, "Techno-economic study of CO2 capture from an existing coal-fired power plant: MEA scrubbing vs. O2/CO2 recycle combustion," *Energy Conversion and Management,* vol. 44, pp. 3073-3091, 2003.

[11] P. Bernardo, E. Drioli, and G. Golemme, "Membrane Gas Separation: A Review/State of the Art," *Industrial & Engineering Chemistry Research,* vol. 48, pp. 4638-4663, 2009/05/20 2009.

[12] E. K. Sandra, A. S. Colin, and W. S. Geoff, "Carbon Dioxide Separation through Polymeric Membrane Systems for Flue Gas Applications," *Recent Patents on Chemical Engineering,* vol. 1, pp. 52-66, 2008.

[13] W. An, P. Swenson, L. Wu, T. Waller, A. Ku, and S. M. Kuznicki, "Selective separation of hydrogen from C1/C2 hydrocarbons and CO2 through dense natural zeolite membranes," *Journal of Membrane Science,* vol. 369, pp. 414-419, 3/1/ 2011.

[14] S. Gopalakrishnan and J. C. Diniz da Costa, "Hydrogen gas mixture separation by CVD silica membrane," *Journal of Membrane Science,* vol. 323, pp. 144-147, 10/1/ 2008.

[15] S. Yun and S. Ted Oyama, "Correlations in palladium membranes for hydrogen separation: A review," *Journal of Membrane Science,* vol. 375, pp. 28-45, 6/15/ 2011.

[16] Y. Zhang, I. H. Musselman, J. P. Ferraris, and K. J. Balkus Jr, "Gas permeability properties of Matrimid® membranes containing the metal-organic framework Cu–BPY–HFS," *Journal of Membrane Science,* vol. 313, pp. 170-181, 4/10/ 2008.

[17] H. Marlies, J. Yan, D. Aijun, K. G. Stephen, and C. S. Sean, "Asymmetrically Decorated, Doped Porous Graphene As an Effective Membrane for Hydrogen Isotope Separation," *The Journal of Physical Chemistry C,* vol. 116, 2012.

[18] H. Liu, S. Dai, and D.-e. Jiang, "Insights into CO2/N2 separation through nanoporous graphene from molecular dynamics," *Nanoscale,* vol. 5, pp. 9984-9987, 2013.

[19] C. Sun, M. S. H. Boutilier, H. Au, P. Poesio, B. Bai, R. Karnik*, et al.*, "Mechanisms of Molecular Permeation through Nanoporous Graphene Membranes," *Langmuir,* vol. 30, pp. 675-682, 2014/01/21 2013.

[20] H. Au, "Moleucular Dynamics Simulation of Nanoporous Graphene for Selcective Gas Separation," Master of Science, Dept. of Mechanical Engineering, Massachusetts Institute of Technology, MIT, 2012.

[21] D.-e. Jiang, V. Cooper, and S. Dai, "Porous graphene as the ultimate membrane for gas separation," *Nano letters,* vol. 9, pp. 4019-4024, Dec 2009.

[22] S. Koenig, L. Wang, J. Pellegrino, and J. Bunch, "Selective molecular sieving through porous graphene," *Nature nanotechnology,* vol. 7, pp. 728-732, Nov 2012.

[23] H. Liu, Z. Chen, S. Dai, and D.-e. Jiang, "Selectivity trend of gas separation through nanoporous graphene," *Journal of Solid State Chemistry*.

[24] D. Huailiang, L. Jingyuan, Z. Jing, S. Gang, L. Xiaoyi, and Z. Yuliang, "Separation of Hydrogen and Nitrogen Gases with Porous Graphene Membrane," *The Journal of Physical Chemistry C,* vol. 115, 2011.

[25] Y. Jiao, A. Du, M. Hankel, and S. C. Smith, "Modelling carbon membranes for gas and isotope separation," *Physical Chemistry Chemical Physics,* vol. 15, pp. 4832-4843, 2013.

[26] S. W. Cranford and M. J. Buehler, "Selective hydrogen purification through graphdiyne under ambient temperature and pressure," *Nanoscale,* vol. 4, pp. 4587-4593, 2012.

[27] Y. Jiao, A. Du, M. Hankel, Z. Zhu, V. Rudolph, and S. C. Smith, "Graphdiyne: a versatile nanomaterial for electronics and hydrogen purification," *Chemical Communications,* vol. 47, pp. 11843-11845, 2011.

[28] F. Li, Y. Qu, and M. Zhao, "Efficient helium separation of graphitic carbon nitride membrane," *Carbon,* vol. 95, pp. 51-57, 12// 2015.

[29] Z. Ma, X. Zhao, Q. Tang, and Z. Zhou, "Computational prediction of experimentally possible g-C3N3 monolayer as hydrogen purification membrane," *International Journal of Hydrogen Energy,* vol. 39, pp. 5037-5042, 3/26/ 2014.

[30] L. Hoonkyung, L. Jia, Z. Gang, D. Wenhui, K. Gunn, and I. Jisoon, "Room-temperature dissociative hydrogen chemisorption on boron-doped fullerenes," *Physical Review B,* vol. 77, 2008.

[31] Q. Sun, M. Wang, Z. Li, Y. Ma, and A. Du, "CO2 capture and gas separation on boron carbon nanotubes," *Chemical Physics Letters,* vol. 575, pp. 59-66, Jun 21 2013.

[32] IEA, *Prospects for CO2 Capture and Storage*: OECD Publishing.

[33] A. S. Damle and T. P. Dorchak, "Recovery of carbon dioxide in advanced fossil energy conversion processes using a membrane reactor," in *First National Conference on Carbon Sequestration, Washington, DC*, 2001.

[34] N. W. Ockwig and T. M. Nenoff, "Membranes for Hydrogen Separation," *Chemical Reviews,* vol. 107, pp. 4078-4110, 2007/10/01 2007.

[35] R. Babarao and J. Jiang, "Diffusion and Separation of CO2 and CH4 in Silicalite, C168 Schwarzite, and IRMOF-1: A Comparative Study from Molecular Dynamics Simulation," *Langmuir,* vol. 24, pp. 5474-5484, 2008/05/01 2008.

[36] X. Yue and X. Yang, "Molecular Simulation Study of Adsorption and Diffusion on Silicalite for a Benzene/CO2 Mixture," *Langmuir,* vol. 22, pp. 3138-3147, 2006/03/01 2006.

[37] R. Krishna and J. M. v. Baten, "Using molecular simulations for screening of zeolites for separation of CO2/CH4 mixtures," *Chemical Engineering Journal,* vol. 133, 2007.

[38] S. T. Oyama, D. Lee, P. Hacarlioglu, and R. F. Saraf, "Theory of hydrogen permeability in nonporous silica membranes," *Journal of Membrane Science,* vol. 244, pp. 45-53, 11/15/ 2004.

[39] N. Du, H. Park, G. Robertson, M. Dal-Cin, T. Visser, L. Scoles*, et al.*, "Polymer nanosieve membranes for CO2-capture applications," *Nature materials,* vol. 10, pp. 372-375, May 2011.

[40] D. F. Sanders, Z. P. Smith, R. Guo, L. M. Robeson, J. E. McGrath, D. R. Paul*, et al.*, "Energy-efficient polymeric gas separation membranes for a sustainable future: A review," *Polymer,* vol. 54, pp. 4729-4761, 8/16/ 2013.

[41] M. Yu, H. H. Funke, R. D. Noble, and J. L. Falconer, "H2 Separation Using Defect-Free, Inorganic Composite Membranes," *Journal of the American Chemical Society,* vol. 133, pp. 1748-1750, 2011/02/16 2011.

[42] K. Yoshida, Y. Hirano, H. Fujii, T. Tsuru, and M. Asaeda, "Hydrothermal Stability and Performance of Silica-Zirconia Membranes for Hydrogen Separation in Hydrothermal Conditions," *JOURNAL OF CHEMICAL ENGINEERING OF JAPAN,* vol. 34, pp. 523-530, 2001.

[43] H. Bux, A. Feldhoff, J. Cravillon, M. Wiebcke, Y.-S. Li, and J. Caro, "Oriented Zeolitic Imidazolate Framework-8 Membrane with Sharp H2/C3H8 Molecular Sieve Separation," *Chemistry of Materials,* vol. 23, pp. 2262-2269, 2011/04/26 2011.

[44] S. Li, J. L. Falconer, and R. D. Noble, "SAPO-34 membranes for CO2/CH4 separation," *Journal of Membrane Science,* vol. 241, pp. 121-135, 9/15/ 2004.

[45] M. P. Bernal, J. Coronas, M. Menéndez, and J. Santamaría, "Separation of CO2/N2 mixtures using MFI-type zeolite membranes," *AIChE Journal,* vol. 50, pp. 127-135, 2004.

[46] Y. Li, F. Liang, H. Bux, W. Yang, and J. Caro, "Zeolitic imidazolate framework ZIF-7 based molecular sieve membrane for hydrogen separation," *Journal of Membrane Science,* vol. 354, pp. 48-54, 5/15/ 2010.

[47] P. M. Follmann, C. Bayer, M. Wessling, and T. Melin, "Chapter 7 Membrane Gas Separation Processes for Post-combustion CO2 Capture," in *Membrane Engineering for the Treatment of Gases: Volume 1: Gas-separation Problems with Membranes*. vol. 1, ed: The Royal Society of Chemistry, 2011, pp. 196-214.

[48] E. Tocci and P. Pullumbi, "Chapter 1 Multi-scale Molecular Modeling Approaches for Designing/Selecting Polymers used for Developing Novel Membranes," in *Membrane Engineering for the Treatment of Gases: Volume 1: Gas-separation Problems with Membranes*. vol. 1, ed: The Royal Society of Chemistry, 2011, pp. 1-28.

[49] L. M. Robeson, "Correlation of separation factor versus permeability for polymeric membranes," *Journal of Membrane Science,* vol. 62, pp. 165-185, 10/1/ 1991.

[50] C. B. Powell, "Occult ovarian cancer at the time of risk-reducing salpingo-oophorectomy," *Gynecologic Oncology,* vol. 100, pp. 1-2, // 2006.

[51] Y. Jiao, A. Du, M. Hankel, and S. Smith, "Modelling carbon membranes for gas and isotope separation," *Physical chemistry chemical physics : PCCP,* vol. 15, pp. 4832-4843, Apr 14 2013.

[52] D. W. Breck, *Zeolite molecular sieves: structure, chemistry, and use*: R.E. Krieger, 1984.

[53] L. M. Robeson, B. D. Freeman, D. R. Paul, and B. W. Rowe, "An empirical correlation of gas permeability and permselectivity in polymers and its theoretical basis," *Journal of Membrane Science,* vol. 341, pp. 178-185, 9/30/ 2009.

[54] K. S. Novoselov, A. K. Geim, S. V. Morozov, D. Jiang, Y. Zhang, S. V. Dubonos*, et al.*, "Electric Field Effect in Atomically Thin Carbon Films," *Science,* vol. 306, pp. 666-669, October 22, 2004 2004.

[55] M. J. Allen, V. C. Tung, and R. B. Kaner, "Honeycomb carbon: a review of graphene," *Chemical reviews,* vol. 110, pp. 132-145, 2009.

[56] A. Reina, X. Jia, J. Ho, D. Nezich, H. Son, V. Bulovic*, et al.*, "Large area, few-layer graphene films on arbitrary substrates by chemical vapor deposition," *Nano letters,* vol. 9, pp. 30-35, 2008.

[57] S. Bae, H. Kim, Y. Lee, X. Xu, J.-S. Park, Y. Zheng*, et al.*, "Roll-to-roll production of 30-inch graphene films for transparent electrodes," *Nature nanotechnology,* vol. 5, pp. 574-578, Aug 2010.

[58] J. Meyer, A. Geim, M. Katsnelson, K. Novoselov, T. Booth, and S. Roth, "The structure of suspended graphene sheets," *Nature,* vol. 446, pp. 60-63, 2007.

[59] C. Lee, X. Wei, J. Kysar, and J. Hone, "Measurement of the elastic properties and intrinsic strength of monolayer graphene," *Science (New York, N.Y.),* vol. 321, pp. 385-388, Jul 18 2008.

[60] C. Lee, X. Wei, J. W. Kysar, and J. Hone, "Measurement of the elastic properties and intrinsic strength of monolayer graphene," *science,* vol. 321, pp. 385-388, Jul 18 2008.

[61] Z.-S. Wu, W. Ren, L. Gao, J. Zhao, Z. Chen, B. Liu*, et al.*, "Synthesis of graphene sheets with high electrical conductivity and good thermal stability by hydrogen arc discharge exfoliation," *Acs Nano,* vol. 3, pp. 411-417, Feb 24 2009.

[62] R. Nair, H. Wu, P. Jayaram, I. Grigorieva, and A. Geim, "Unimpeded permeation of water through helium-leak-tight graphene-based membranes," *Science (New York, N.Y.),* vol. 335, pp. 442-444, Jan 27 2012.

[63] J. Bunch, S. Verbridge, J. Alden, A. van der Zande, J. Parpia, H. Craighead*, et al.*, "Impermeable atomic membranes from graphene sheets," *Nano letters,* vol. 8, pp. 2458-2462, Aug 2008.

[64] D. F. Michael and D. Marija, "Electron beam nanosculpting of suspended graphene sheets," *Applied Physics Letters,* vol. 93, p. 113107, 2008.

[65] P. Kuhn, A. Forget, D. Su, A. Thomas, and M. Antonietti, "From microporous regular frameworks to mesoporous materials with ultrahigh surface area: dynamic reorganization of porous polymer networks," *Journal of the American Chemical Society,* vol. 130, pp. 13333-13337, 2008.

[66] M. Bieri, M. Treier, J. Cai, K. Aït-Mansour, P. Ruffieux, O. Gröning*, et al.*, "Porous graphenes: two-dimensional polymer synthesis with atomic precision," *Chemical communications (Cambridge, England),* pp. 6919-6921, Dec 7 2009.

[67] J. Schrier, "Carbon Dioxide Separation with a Two-Dimensional Polymer Membrane," *ACS Applied Materials & Interfaces,* vol. 4, pp. 3745-3752, 2012/07/25 2012.

[68] M. Shan, Q. Xue, N. Jing, C. Ling, T. Zhang, Z. Yan*, et al.*, "Influence of chemical functionalization on the CO2/N2 separation performance of porous graphene membranes," *Nanoscale,* vol. 4, pp. 5477-5482, 2012.

[69] Y. Li, Z. Zhou, P. Shen, and Z. Chen, "Two-dimensional polyphenylene: experimentally available porous graphene as a hydrogen purification membrane," *Chemical communications (Cambridge, England),* vol. 46, pp. 3672-3674, 2010.

[70] H. Kim, H. Yoon, S.-M. Yoon, B. Yoo, B. Ahn, Y. Cho*, et al.*, "Selective gas transport through few-layered graphene and graphene oxide membranes," *Science (New York, N.Y.),* vol. 342, pp. 91-95, Oct 4 2013.

[71] G. Li, Y. Li, H. Liu, Y. Guo, Y. Li, and D. Zhu, "Architecture of graphdiyne nanoscale films," *Chemical Communications,* vol. 46, pp. 3256-3258, May 21 2010.

[72] M. Bartolomei, E. Carmona-Novillo, M. I. Hernández, J. Campos-Martínez, F. Pirani, G. Giorgi*, et al.*, "Penetration Barrier of Water through Graphynes' Pores: First-Principles Predictions and Force Field Optimization," *The Journal of Physical Chemistry Letters,* vol. 5, pp. 751-755, 2014/02/20 2014.

[73] X. Minmin, Q. Hu, and G. Wanlin, "Exceptionally fast water desalination at complete salt rejection by pristine graphyne monolayers," *Nanotechnology,* vol. 24, p. 505720, 2013.

[74] J. Kou, X. Zhou, H. Lu, F. Wu, and J. Fan, "Graphyne as the membrane for water desalination," *Nanoscale,* vol. 6, pp. 1865-1870, 2014.

[75] H. Zhang, X. He, M. Zhao, M. Zhang, L. Zhao, X. Feng*, et al.*, "Tunable Hydrogen Separation in sp–sp2 Hybridized Carbon Membranes: A First-Principles Prediction," *The Journal of Physical Chemistry C,* vol. 116, pp. 16634-16638, 2012/08/09 2012.

[76] X. Zhuang, Y. Mai, D. Wu, F. Zhang, and X. Feng, "Two-Dimensional Soft Nanomaterials: A Fascinating World of Materials," *Advanced Materials,* vol. 27, pp. 403-427, 2015.

[77] S. Zhang, J. Li, M. Zeng, J. Xu, X. Wang, and W. Hu, "Polymer nanodots of graphitic carbon nitride as effective fluorescent probes for the detection of Fe3+ and Cu2+ ions," *Nanoscale,* vol. 6, pp. 4157-4162, 2014.

[78] Y. Wang, X. Wang, and M. Antonietti, "Polymeric Graphitic Carbon Nitride as a Heterogeneous Organocatalyst: From Photochemistry to Multipurpose Catalysis to Sustainable Chemistry," *Angewandte Chemie International Edition,* vol. 51, pp. 68-89, 2012.

[79] K. Cao, Z. Jiang, X. Zhang, Y. Zhang, J. Zhao, R. Xing*, et al.*, "Highly water-selective hybrid membrane by incorporating g-C3N4 nanosheets into polymer matrix," *Journal of Membrane Science,* vol. 490, pp. 72-83, 9/15/ 2015.

[80] G. Dong, Y. Zhang, Q. Pan, and J. Qiu, "A fantastic graphitic carbon nitride (g-C3N4) material: Electronic structure, photocatalytic and photoelectronic properties," *Journal of Photochemistry and Photobiology C: Photochemistry Reviews,* vol. 20, pp. 33-50, 9// 2014.

[81] S. Ye, R. Wang, M.-Z. Wu, and Y.-P. Yuan, "A review on g-C3N4 for photocatalytic water splitting and CO2 reduction," *Applied Surface Science,* vol. 358, Part A, pp. 15-27, 12/15/ 2015.

[82] S. Yin, J. Han, T. Zhou, and R. Xu, "Recent progress in g-C3N4 based low cost photocatalytic system: activity enhancement and emerging applications," *Catalysis Science & Technology,* vol. 5, pp. 5048-5061, 2015.

[83] J. Mahmood, E. K. Lee, M. Jung, D. Shin, I.-Y. Jeon, S.-M. Jung*, et al.*, "Nitrogenated holey two-dimensional structures," *Nature Communications,* vol. 6, p. 6486, 03/06/online 2015.

[84] B. Xu, H. Xiang, Q. Wei, J. Q. Liu, Y. D. Xia, J. Yin*, et al.*, "Two-dimensional graphene-like C2N: an experimentally available porous membrane for hydrogen purification," *Physical Chemistry Chemical Physics,* vol. 17, pp. 15115-15118, 2015.

[85] Y. Qu, F. Li, H. Zhou, and M. Zhao, "Highly Efficient Quantum Sieving in Porous Graphene-like Carbon Nitride for Light Isotopes Separation," *Scientific Reports,* vol. 6, p. 19952, 01/27/online 2016.

[86] Y. Wang, J. Li, Q. Yang, and C. Zhong, "Two-Dimensional Covalent Triazine Framework Membrane for Helium Separation and Hydrogen Purification," *ACS Applied Materials & Interfaces,* vol. 8, pp. 8694-8701, 2016/04/06 2016.

[87] M. Corso, W. Auwärter, M. Muntwiler, A. Tamai, T. Greber, and J. Osterwalder, "Boron Nitride Nanomesh," *Science,* vol. 303, pp. 217-220, 2004.

[88] D. Golberg, Y. Bando, Y. Huang, T. Terao, M. Mitome, C. Tang*, et al.*, "Boron Nitride Nanotubes and Nanosheets," *ACS Nano,* vol. 4, pp. 2979-2993, 2010/06/22 2010.

[89] A. Pakdel, C. Zhi, Y. Bando, and D. Golberg, "Low-dimensional boron nitride nanomaterials," *Materials Today,* vol. 15, pp. 256-265, 6// 2012.

[90] X.-F. Jiang, Q. Weng, X.-B. Wang, X. Li, J. Zhang, D. Golberg*, et al.*, "Recent Progress on Fabrications and Applications of Boron Nitride Nanomaterials: A Review," *Journal of Materials Science & Technology,* vol. 31, pp. 589-598, 6// 2015.

[91] S. Liu, B. Lu, Q. Zhao, J. Li, T. Gao, Y. Chen*, et al.*, "Boron Nitride Nanopores: Highly Sensitive DNA Single-Molecule Detectors," *Advanced Materials,* vol. 25, pp. 4549-4554, 2013.

[92] Z. Zhou, Y. Hu, H. Wang, Z. Xu, W. Wang, X. Bai*, et al.*, "DNA Translocation through Hydrophilic Nanopore in Hexagonal Boron Nitride," *Scientific Reports,* vol. 3, p. 3287, 11/21/online 2013.

[93] Z. Zhou, Y. Hu, X. Shan, and X. Lu, "Single DNA Molecule Sensing with Boron Nitride Nanopores."

[94] L. Zhang and X. Wang, "DNA Sequencing by Hexagonal Boron Nitride Nanopore: A Computational Study," *Nanomaterials,* vol. 6, p. 111, 2016.

[95] Y. Zhang, Q. Shi, Y. Liu, Y. Wang, Z. Meng, C. Xiao*, et al.*, "Hexagonal Boron Nitride with Designed Nanopores as a High-Efficiency Membrane for Separating Gaseous Hydrogen from Methane," *The Journal of Physical Chemistry C,* vol. 119, pp. 19826-19831, 2015/08/27 2015.

[96] F. Ma, M. Zhou, Y. Jiao, G. Gao, Y. Gu, A. Bilic*, et al.*, "Single Layer Bismuth Iodide: Computational Exploration of Structural, Electrical, Mechanical and Optical Properties," *Scientific Reports,* vol. 5, p. 17558, 12/02/online 2015.

[97] P. Li, L. Li, and X. C. Zeng, "Tuning the electronic properties of monolayer and bilayer PtSe2via strain engineering," *Journal of Materials Chemistry C,* vol. 4, pp. 3106-3112, 2016.

[98] Y. Li and Z. Chen, "Tuning Electronic Properties of Germanane Layers by External Electric Field and Biaxial Tensile Strain: A Computational Study," *The Journal of Physical Chemistry C,* vol. 118, pp. 1148-1154, 2014/01/16 2014.

[99] P. Johari and V. B. Shenoy, "Tuning the Electronic Properties of Semiconducting Transition Metal Dichalcogenides by Applying Mechanical Strains," *ACS Nano,* vol. 6, pp. 5449-5456, 2012/06/26 2012.

[100] K. He, C. Poole, K. F. Mak, and J. Shan, "Experimental Demonstration of Continuous Electronic Structure Tuning via Strain in Atomically Thin MoS2," *Nano Letters,* vol. 13, pp. 2931-2936, 2013/06/12 2013.

[101] P. Gerd, C.-G. Andres, B. Michele, S. J. v. d. Z. Herre, A. S. Gary, K. Agnieszka*, et al.*, "Control of biaxial strain in single-layer molybdenite using local thermal expansion of the substrate," *2D Materials,* vol. 2, p. 015006, 2015.

[102] D. M. D'Alessandro, B. Smit, and J. R. Long, "Carbon Dioxide Capture: Prospects for New Materials," *Angewandte Chemie International Edition,* vol. 49, pp. 6058-6082, Aug 16 2010.

[103] A. O. z. r. Yazaydın, R. Q. Snurr, T.-H. Park, K. Koh, J. Liu, M. D. LeVan*, et al.*, "Screening of Metal−Organic Frameworks for Carbon Dioxide Capture from Flue Gas Using a Combined Experimental and Modeling Approach," *Journal of the American Chemical Society,* vol. 131, pp. 18198-18199, 2009/12/30 2009.

[104] P. J. E. Harlick and A. Sayari, "Applications of Pore-Expanded Mesoporous Silicas. 3. Triamine Silane Grafting for Enhanced CO2 Adsorption," *Industrial & Engineering Chemistry Research,* vol. 45, pp. 3248-3255, 2006/04/01 2006.

[105] Q. Sun, Z. Li, D. J. Searles, Y. Chen, G. Lu, and A. Du, "Charge-Controlled Switchable CO2 Capture on Boron Nitride Nanomaterials," *Journal of the American Chemical Society,* vol. 135, pp. 8246-8253, 2013/06/05 2013.

[106] Z. Chen and R. King, "Spherical aromaticity: recent work on fullerenes, polyhedral boranes, and related structures," *Chemical reviews,* vol. 105, pp. 3613-3642, Oct 2005.

[107] T. Reshef, "Doped and heteroatom-containing fullerene-like structures and nanotubes," *Advanced Materials,* vol. 7, 1995.

[108] B. Gao, J. X. Zhao, Q. H. Cai, X. G. Wang, and X. Z. Wang, "Doping of calcium in C(60) fullerene for enhancing CO(2) capture and N(2)O transformation: a theoretical study," *J Phys Chem A,* vol. 115, pp. 9969-76, Sep 8 2011.

[109] F. Gao, G.-L. Zhao, S. Yang, and J. J. Spivey, "Nitrogen-Doped Fullerene as a Potential Catalyst for Hydrogen Fuel Cells," *Journal of the American Chemical Society,* vol. 135, pp. 3315-3318, 2013/03/06 2012.

[110] T. Guo, C. Jin, and R. E. Smalley, "Doping bucky: formation and properties of boron-doped buckminsterfullerene," *J Phys Chem-Us,* vol. 95, pp. 4948-4950, 1991/06/01 1991.

[111] Y. J. Zou, X. W. Zhang, Y. L. Li, B. Wang, H. Yan, J. Z. Cui*, et al.*, "Bonding character of the boron-doped C60 films prepared by radio frequency plasma assisted vapor deposition," *Journal of Materials Science,* vol. 37, pp. 1043-1047, 2002/03/01 2002.

[112] W. D. Paul, R.-F. Antonio, K. K. Nathan, S. Hisanori, M. P. Josep, and W. K. Harold, "Formation of Heterofullerenes by Direct Exposure of C 60 to Boron Vapor," *Angewandte Chemie,* vol. 125, pp. 333-337, 2013.

[113] S.-H. Wang, F. Chen, Y. C. Fann, M. Kashani, M. Malaty, and S. A. Jansen, "Assessment of the Stability of Heterohedral Fullerenes: A Theoretical Analysis of C60-xNx and C60-xBx Where x = 1 and 2," *J. Phys. Chem.A,* vol. 99, pp. 6801-6807, 1995/05/01 1995.

[114] N. Kurita, K. Kobayashi, H. Kumahora, K. Tago, and K. Ozawa, "Molecular structures, binding energies and electronic properties of dopyballs C59X (X=B, N and S)," *Chemical Physics Letters,* vol. 198, pp. 95-99, 10/2/ 1992.

[115] L. Zhu, Q. Xue, X. Li, T. Wu, Y. Jin, and W. Xing, "C2N: an excellent two-dimensional monolayer membrane for He separation," *Journal of Materials Chemistry A,* vol. 3, pp. 21351-21356, 2015.

[116] Y. Wang, Q. Yang, J. Li, J. Yang, and C. Zhong, "Exploration of nanoporous graphene membranes for the separation of N2 from CO2: a multi-scale computational study," *Physical Chemistry Chemical Physics,* vol. 18, pp. 8352-8358, 2016.

[117] R. Babarao, S. Dai, and D.-e. Jiang, "Nitrogen-Doped Mesoporous Carbon for Carbon Capture – A Molecular Simulation Study," *The Journal of Physical Chemistry C,* vol. 116, pp. 7106-7110, 2012/03/29 2012.

[118] Y. Jiao, A. Du, Z. Zhu, V. Rudolph, and S. C. Smith, "Adsorption of Carbon Dioxide and Nitrogen on Single-Layer Aluminum Nitride Nanostructures Studied by Density Functional Theory," *The Journal of Physical Chemistry C,* vol. 114, pp. 7846-7849, 2010/05/06 2010.

[119] Y. Jiao, A. Du, Z. Zhu, V. Rudolph, and S. C. Smith, "A density functional theory study of CO2 and N2 adsorption on aluminium nitride single walled nanotubes," *Journal of Materials Chemistry,* vol. 20, pp. 10426-10430, 2010.

[120] A. Torrisi, C. Mellot-Draznieks, and R. G. Bell, "Impact of ligands on CO2 adsorption in metal-organic frameworks: First principles study of the interaction of CO2 with functionalized benzenes. II. Effect of polar and acidic substituents," *The Journal of Chemical Physics,* vol. 132, pp. -, Jan 28 2010.

[121] S. Choi, T. Watanabe, T.-H. Bae, D. S. Sholl, and C. W. Jones, "Modification of the Mg/DOBDC MOF with Amines to Enhance CO2 Adsorption from Ultradilute Gases," *The Journal of Physical Chemistry Letters,* vol. 3, pp. 1136-1141, 2012/05/03 2012.

[122] M. L. Terranova, S. Orlanducci, and M. Rossi, *Carbon nanomaterials for gas adsorption*: CRC Press, 2012.

[123] J. B. Foresman and Æ. Frisch, *Exploring chemistry with electronic structure methods: A Guide to Using Gaussian*, Second Edition ed. vol. 118. Pittsburgh, PA: Gaussian Inc. , 1996.

[124] K. I. Ramachandran, D. Gopakumar, and K. Namboori, *Computational Chemistry and Molecular Modeling: Principles and Applications*. Berlin, Heidelberg: Springer Berlin Heidelberg, 2008.

[125] M. J. Dewar, E. G. Zoebisch, E. F. Healy, and J. J. Stewart, "Development and use of quantum mechanical molecular models. 76. AM1: a new general purpose quantum mechanical molecular model," *Journal of the American Chemical Society,* vol. 107, pp. 3902-3909, 1985.

[126] J. J. P. Stewart, "Optimization of parameters for semiempirical methods I. Method," *Journal of Computational Chemistry,* vol. 10, pp. 209-220, 1989.

[127] J. J. P. Stewart, "Optimization of parameters for semiempirical methods II. Applications," *Journal of Computational Chemistry,* vol. 10, pp. 221-264, 1989.

[128] J. Pople, D. Beveridge, and P. Dobosh, "Approximate Self-Consistent Molecular-Orbital Theory. V. Intermediate Neglect of Differential Overlap," *The Journal of Chemical Physics,* vol. 47, pp. 2026-2033, 1967.

[129] J. A. Pople and G. A. Segal, "Approximate Self-Consistent Molecular Orbital Theory. III. CNDO Results for AB2 and AB3 Systems," *The Journal of Chemical Physics,* vol. 44, pp. 3289-3296, 1966.

[130] P. Hohenberg and W. Kohn, "Inhomogeneous Electron Gas," *Physical Review,* vol. 136, pp. B864-B871, 11/09/ 1964.

[131] M. Levy, "Universal variational functionals of electron densities, first-order density matrices, and natural spin-orbitals and solution of the v-representability problem," *Proceedings of the National Academy of Sciences,* vol. 76, pp. 6062-6065, December 1, 1979 1979.

[132] H. Jacobsen and L. Cavallo, "Directions for Use of Density Functional Theory: A Short Instruction Manual for Chemists," in *Handbook of Computational Chemistry*, J. Leszczynski, Ed., ed Dordrecht: Springer Netherlands, 2012, pp. 95-133.

[133] S. H. Vosko, L. Wilk, and M. Nusair, "Accurate spin-dependent electron liquid correlation energies for local spin density calculations: a critical analysis," *Canadian Journal of Physics,* vol. 58, pp. 1200-1211, 1980/08/01 1980.

[134] J. P. Perdew and Y. Wang, "Accurate and simple analytic representation of the electron-gas correlation energy," *Physical Review B,* vol. 45, pp. 13244-13249, 06/15/ 1992.

[135] J. P. Perdew, K. Burke, and M. Ernzerhof, "Generalized Gradient Approximation Made Simple," *Physical Review Letters,* vol. 77, pp. 3865-3868, 10/28/ 1996.

[136] A. D. Becke, "A multicenter numerical integration scheme for polyatomic molecules," *The Journal of Chemical Physics,* vol. 88, pp. 2547-2553, 1988.

[137] C. Lee, W. Yang, and R. G. Parr, "Development of the Colle-Salvetti correlation-energy formula into a functional of the electron density," *Physical Review B,* vol. 37, p. 785, Jan 15 1988.

[138] P. J. Stephens, F. J. Devlin, C. F. Chabalowski, and M. J. Frisch, "Ab Initio Calculation of Vibrational Absorption and Circular Dichroism Spectra Using Density Functional Force Fields," *The Journal of Physical Chemistry,* vol. 98, pp. 11623-11627, 1994/11/01 1994.

[139] A. D. Becke, "Density-functional thermochemistry. III. The role of exact exchange," *The Journal of Chemical Physics,* vol. 98, pp. 5648-5652, 1993.

[140] C. Cazorla and S. A. Shevlin, "Accuracy of density functional theory in the prediction of carbon dioxide adsorbent materials," *Dalton Transactions,* vol. 42, pp. 4670-4676, Apr 7 2013.

[141] F. Negri and N. Saendig, "Tuning the physisorption of molecular hydrogen: binding to aromatic, hetero-aromatic and metal-organic framework materials," *Theoretical Chemistry Accounts,* vol. 118, pp. 149-163, 2007/07/01 2007.

[142] S. F. Boys and F. Bernardi, "The calculation of small molecular interactions by the differences of separate total energies. Some procedures with reduced errors," *Molecular Physics,* vol. 19, pp. 553-566, 1970/10/01 1970.

[143] A. Torrisi, C. Mellot-Draznieks, and R. G. Bell, "Impact of ligands on CO2 adsorption in metal-organic frameworks: First principles study of the interaction of CO2 with functionalized benzenes. I. Inductive effects on the aromatic ring," *The Journal of Chemical Physics,* vol. 130, pp. -, May 21 2009.

[144] B. Delley, "An all-electron numerical method for solving the local density functional for polyatomic molecules," *The Journal of Chemical Physics,* vol. 92, pp. 508-517, 1990.

[145] B. Delley, "From molecules to solids with the DMol3 approach," *The Journal of Chemical Physics,* vol. 113, pp. 7756-7764, 2000.

[146] M. J. Frisch, G. W. Trucks, H. B. Schlegel, G. E. Scuseria, M. A. Robb, J. R. Cheeseman*, et al.*, "Gaussian 09," vol. Revision B.01, ed. Wallingford CT: Gausian, Inc., 2009.

[147] R. Dennington, T. Keith, and J. Millam, "GaussView," vol. Version 5, ed. Shawnee Mission, KS: Semichem Inc., 2009.

[148] C. Lorenz and N. L. Doltsinis, "Molecular Dynamics Simulation: From "Ab Initio" to "Coarse Grained"," in *Handbook of Computational Chemistry*, J. Leszczynski, Ed., ed Dordrecht: Springer Netherlands, 2012, pp. 195-238.

[149] J. E. Jones, "On the Determination of Molecular Fields. II. From the Equation of State of a Gas," *Proceedings of the Royal Society of London. Series A,* vol. 106, pp. 463-477, 1924.

[150] R. W. Hockney, "POTENTIAL CALCULATION AND SOME APPLICATIONS," Langley Research Center, Hampton, Va.1970.

[151] C. W. Gear, "Algorithm 407: DIFSUB for solution of ordinary differential equations [D2]," *Communications of the ACM,* vol. 14, pp. 185-190, 1971.

[152] L. Verlet, "Computer" experiments" on classical fluids. I. Thermodynamical properties of Lennard-Jones molecules," *Physical review,* vol. 159, p. 98, 1967.

[153] A. Leach, *Molecular Modelling: Principles and Applications (2nd Edition)*: Prentice Hall, 2001.

[154] D. C. Young, "Molecular Dynamics and Monte Carlo Simulations," in *Computational Chemistry*, ed: John Wiley & Sons, Inc., 2002, pp. 60-66.

[155] R. W. Hockney, "The Potential Calculation and Some Applications," *Methods Comput. Phys.,* vol. 9, pp. 136-210, // 1970.

[156] W. C. Swope, H. C. Andersen, P. H. Berens, and K. R. Wilson, "A computer simulation method for the calculation of equilibrium constants for the formation of physical clusters of molecules: Application to small water clusters," *The Journal of Chemical Physics,* vol. 76, pp. 637-649, 1982.

[157] D. Beeman, "Some multistep methods for use in molecular dynamics calculations," *Journal of Computational Physics,* vol. 20, pp. 130-139, 1976.

[158] F. Plus, "Accelrys Inc," *San Diego, CA [2008] http://accelrys. com/products/datasheets/forcite-plus. pdf.*

[159] S. Plimpton, "Fast Parallel Algorithms for Short-Range Molecular Dynamics," *Journal of Computational Physics,* vol. 117, pp. 1-19, 3/1/ 1995.

[160] C. Lee, W. Yang, and R. G. Parr, "Development of the Colle-Salvetti correlation-energy formula into a functional of the electron density," *Physical Review B,* vol. 37, pp. 785-789, 01/15/ 1988.

[161] R. S. Mulliken, "Electronic Population Analysis on LCAO–MO Molecular Wave Functions. I," *The Journal of Chemical Physics,* vol. 23, pp. 1833-1840, 1955.

[162] C. Peng and H. Bernhard Schlegel, "Combining Synchronous Transit and Quasi-Newton Methods to Find Transition States," *Israel Journal of Chemistry,* vol. 33, pp. 449-454, 1993.

[163] H. P. Hratchian and H. B. Schlegel, *Finding minima, transition states, and following reaction pathways on ab initio potential energy surfaces*: Elsevier: Amsterdam, 2005.

[164] C. Peng, P. Y. Ayala, H. B. Schlegel, and M. J. Frisch, "Using redundant internal coordinates to optimize equilibrium geometries and transition states," *Journal of Computational Chemistry,* vol. 17, pp. 49-56, Jan 15 1996.

[165] C. Gonzalez and H. B. Schlegel, "An improved algorithm for reaction path following," *The Journal of Chemical Physics,* vol. 90, pp. 2154-2161, Feb 15 1989.

[166] K.-C. Kim, F. Hauke, A. Hirsch, P. D. W. Boyd, E. Carter, R. S. Armstrong*, et al.*, "Synthesis of the C59N+ Carbocation. A Monomeric Azafullerene Isoelectronic to C60," *Journal of the American Chemical Society,* vol. 125, pp. 4024-4025, 2003/04/01 2003.

[167] R.-H. Xie, G. W. Bryant, J. Zhao, V. H. Smith Jr, A. Di Carlo, and A. Pecchia, "Tailorable Acceptor C 60− n B n and Donor C 60− m N m Pairs for Molecular Electronics," *Physical review letters,* vol. 90, p. 206602, 2003.

[168] S. Chu and A. Majumdar, "Opportunities and challenges for a sustainable energy future," *Nature,* vol. 488, pp. 294-303, Aug 16 2012.

[169] S. Grimme, "Semiempirical GGA-type density functional constructed with a long-range dispersion correction," *Journal of Computational Chemistry,* vol. 27, pp. 1787-1799, 2006.

[170] H. J. Monkhorst and J. D. Pack, "Special points for Brillouin-zone integrations," *Physical Review B,* vol. 13, p. 5188, 1976.

[171] E. Kroke and M. Schwarz, "Novel group 14 nitrides," *Coordination Chemistry Reviews,* vol. 248, pp. 493-532, 3// 2004.

[172] T. A. Halgren and W. N. Lipscomb, "The synchronous-transit method for determining reaction pathways and locating molecular transition states," *Chemical Physics Letters,* vol. 49, pp. 225-232, 1977/07/15 1977.

[173] N. Govind, M. Petersen, G. Fitzgerald, D. King-Smith, and J. Andzelm, "A generalized synchronous transit method for transition state location," *Computational Materials Science,* vol. 28, pp. 250-258, 10// 2003.

[174] T. R. Mattsson, J. M. D. Lane, K. R. Cochrane, M. P. Desjarlais, A. P. Thompson, F. Pierce*, et al.*, "First-principles and classical molecular dynamics simulation of shocked polymers," *Physical Review B,* vol. 81, p. 054103, 2010.

[175] A. van Duin, "Reaxff user manual," *California Institute of Technology, Materials and Process Simulation Center,* 2002.

[176] Y. Ji, H. Dong, H. Lin, L. Zhang, T. Hou, and Y. Li, "Heptazine-based graphitic carbon nitride as an effective hydrogen purification membrane," *RSC Advances,* vol. 6, pp. 52377-52383, 2016.

[177] A. D. Buckingham, R. L. Disch, and D. A. Dunmur, "Quadrupole moments of some simple molecules," *Journal of the American Chemical Society,* vol. 90, pp. 3104-3107, 1968/06/01 1968.

[178] S. Alavi, J. A. Ripmeester, and D. D. Klug, "Molecular-dynamics study of structure II hydrogen clathrates," *The Journal of Chemical Physics,* vol. 123, p. 024507, 2005.

[179] I. F. Silvera and V. V. Goldman, "The isotropic intermolecular potential for H2 and D2 in the solid and gas phases," *The Journal of Chemical Physics,* vol. 69, pp. 4209-4213, 1978.

[180] G. H. Jonathan and H. Y. Kwong, "Carbon Dioxide's Liquid-Vapor Coexistence Curve And Critical Properties as Predicted by a Simple Molecular Model," *The Journal of Physical Chemistry,* 1995.

[181] R. D. Etters and B. Kuchta, "Static and dynamic properties of solid CO2 at various temperatures and pressures," *The Journal of Chemical Physics,* vol. 90, pp. 4537-4541, 1989.

[182] C. S. Murthy, K. Singer, M. L. Klein, and I. R. McDonald, "Pairwise additive effective potentials for nitrogen," *Molecular Physics,* vol. 41, pp. 1387-1399, 1980/12/20 1980.

[183] H. Stassen, "On the pair potential in dense fluid methane," *Journal of Molecular Structure: THEOCHEM,* vol. 464, pp. 107-119, 5/18/ 1999.

APPENDIX A

Results for repeated simulations for Pore-13-B under 5% strain

To avoid any statistical uncertainty, the simulations were carried out twice for pore-13-B. Below are the results from the repeated simulations. The results are within the same range of the first simulations and observed a near identical trend.

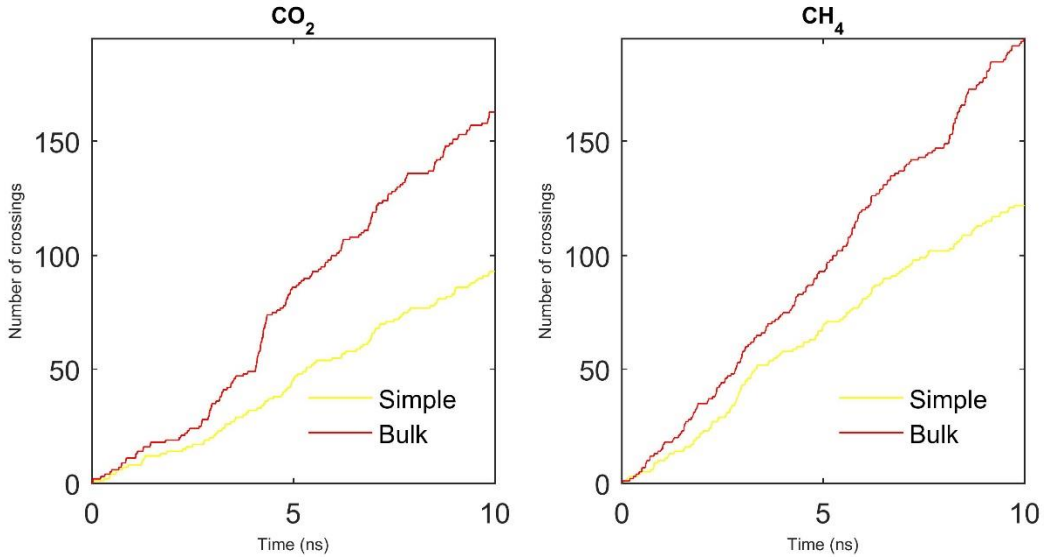

APPENDIX B

Feed side pressure variation during simulation for C_2N gas permeation study

Below, we compare the feed side pressure variation for the four different gases. It should be noted that the pressure represented here is in the bulk zone and the gas molecules adsorbed on the solid adsorbent is assumed to not contribute towards the bulk feed side pressure. Due to a combination of high permeability and adsorption on the solid membrane, the feed pressures in CO_2 simulation systems are comparatively low. The feed side pressure of H_2 too, gradually decreases due to the molecular crossing to the permeate side. The disparity of the permeate rate and pressure variation between CO_2 and H_2 gas molecules is an indication of the high CO_2 adsorption on the C_2N monolayer.

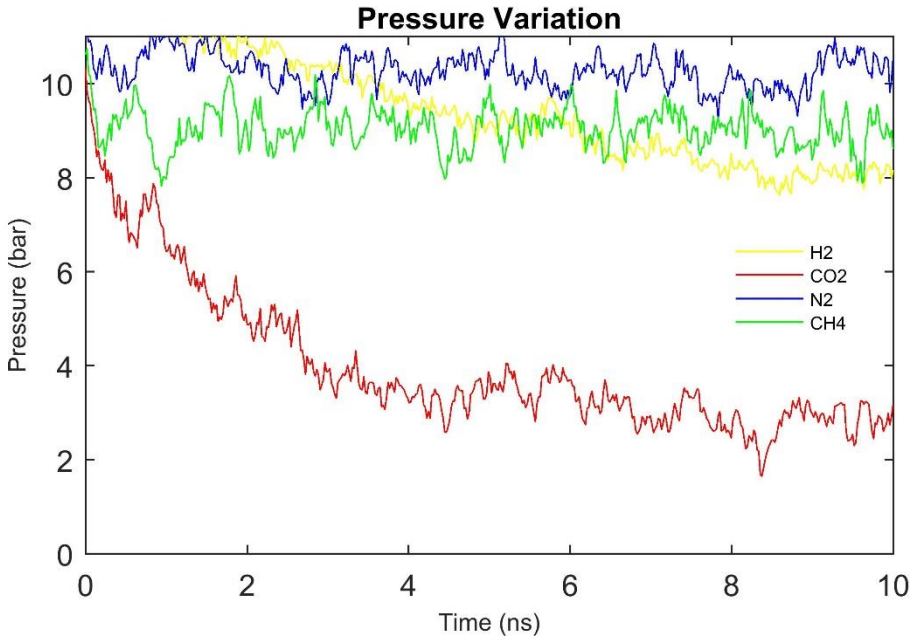

A: Strain 5%

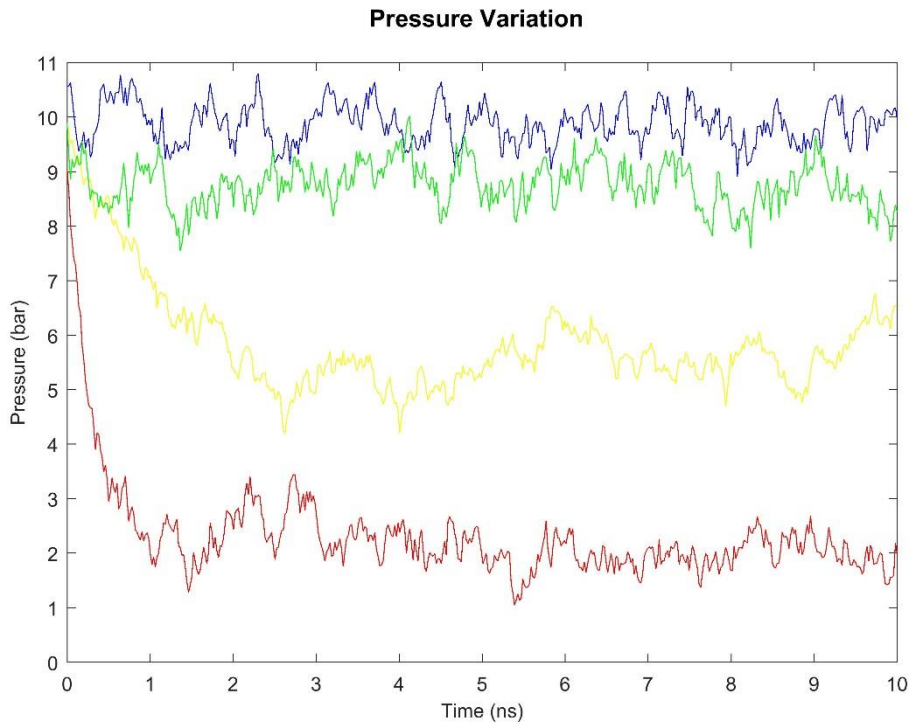

B: Strain 7%